Experiments of Search for Neutron Electric Dipole Moment and Spin-Dependent Short-Range Force

by

Wangzhi Zheng

Department of Physics
Duke University

Date: __________________________
Approved:

____
Haiyan Gao, Supervisor

____
Robert Behringer

____
Calvin Howell

____
Ashutosh Kotwal

____
Thomas Mehen

Dissertation submitted in partial fulfillment of the requirements for the degree of
Doctor of Philosophy in the Department of Physics
in the Graduate School of Duke University
2012

Abstract

Experiments of Search for Neutron Electric Dipole Moment and Spin-Dependent Short-Range Force

by

Wangzhi Zheng

Department of Physics
Duke University

Date: ____________________
Approved:

____
Haiyan Gao, Supervisor

____
Robert Behringer

____
Calvin Howell

____
Ashutosh Kotwal

____
Thomas Mehen

An abstract of a dissertation submitted in partial fulfillment of the requirements for
the degree of Doctor of Philosophy in the Department of Physics
in the Graduate School of Duke University
2012

Copyright © 2012 by Wangzhi Zheng
All rights reserved

Abstract

It is of great importance to identify new sources of discrete symmetry violations because it can explain the baryon number asymmetry of our universe and also test the validity of various models beyond the standard model. Neutron Electric Dipole Moment (nEDM) and short-range force are such candidates for the new sources of P&T violations. A new generation nEDM experiment was proposed in USA in 2002, aiming at improving the current nEDM upperlimit by two orders of magnitude. Polarized ^{3}He is crucial in this experiment and Duke is responsible for the ^{3}He injection, measurements of ^{3}He nuclear magnetic resonance (NMR) signal and some physics properties related to polarized ^{3}He.

A Monte-Carlo simulation is used to simulate the entire ^{3}He injection process in order to study whether polarized ^{3}He can be successfully delivered to the measurement cell. Our simulation result shows that it is achievable to maintain more than 95% polarization after ^{3}He atoms travel through very complicated paths in the presence of non-uniform magnetic fiels.

We also built an apparatus to demonstrate that the ^{3}He precession signal can be measured under the nEDM experimental conditions using the Superconducting Quantum Interference Device (SQUID). Based on the measurement result in our lab, we project that the signal-to-noise ratio in the nEDM experiment will be at least 10.

During this SQUID test, two interesting phenomena were discovered. One is the pressure dependence of the T_1 of the polarized ^{3}He which has never been reported

before. The other is the discrepancy between the theoretically predicted T_2 and the experimentally measured T_2 of the ^{3}He precession signal. To investigate these two interesting phenomena, two dedicated experiments were built, and two papers have been published in Physical Review A.

In addition to the nEDM experiment, polarized ^{3}He is also used in the search for the exotic short-range force. The high pressure ^{3}He cell used in this experiment has a very thin window ($\sim$ 250 μm) to maximize the effect from the force. We demonstrate that our new method could improve the current best experimental limit by two orders of magnitude. A rapid communication demonstrating the technique and the result was published in Physical Review D.

To my parents and the memory of my grandfather

Contents

List of Figures

List of Abbreviations and Symbols

Symbols

C	Charge conjugation
P	Parity transformation
T	Time reversal transformation
CP	C and P combined transformation
T_1	Longitudinal relaxation time
T_2	Transverse relaxation time

Abbreviations

SM	Standard model
UCN	Ultra-cold neutron
UV	Ultra-violet
FID	Free induction decay
NMR	Nuclear magnetic resonance
pNMR	Pulsed nuclear magnetic resonance
nEDM	Neutron electric dipole moment
SQUID	Superconducting quantum interference device
ABS	Atomic beam source
LANL	Los Alamos national lab
ORNL	Oak Ridge national lab

Acknowledgements

It has been more than five years since I came to Duke to pursue my PhD degree in physics. At the beginning of the journey, I felt excited but also unsecured. You never knew what would happen and how fierce it was going to be. To me, it was like driving a yacht through a stormy sea to an unknown island, which is so far away that only imagination can help. Fortunately, that island is so close to me right now and I can see it even without my glasses. I am amazed that how peaceful and delightful this journey turns out to be, and I deeply feel that I am indebted to many people who, during this journey, always stand by my side, support me and encourage me to do more than I can achieve.

First of all, I want to thank my advisor Prof. Haiyan Gao, who is the captain of this journey. Without her navigation and support, I could not imagine how difficult the journey would be. Not only a captain to me, she is also a parent and friend who cares about my growth and teaches me many things beyond the physics that are invaluable to me and my future life.

I also want to thank all the members in the MEP group, especially to Qiang Ye and Xiaofeng Zhu. Qiang is always kind enough to teach me all the experimental skills and help me with my experiment. I can never forget that we work together on the SQUID experiment until the midnight of the thanksgiving eve, which is the best thanksgiving eve I have ever had. Xiaofeng is always generous to share all his knowledge and skills with me. He helped me to start my own research at the very

beginning of my PhD study and it is also his diligence and enthusiasm in physics that impress me and urge me to work harder. Many thanks also go to Wei, Xing Zong, Xin Qian, Pinghan, Sucheta, Qiujian, Ming, George, Yang and Chao both as group members and friends. They always support me and lend me a hand whenever I ask for help. It is the time we spent together throughout the past five years that makes my PhD journey adorable and full of pleasure. Particularly, I want to say thank you to Sucheta for her careful proof-reading of every chapter of my thesis. It is her effort that greatly improves the writing and quality of this thesis.

More thanks go to the people in TUNL and the physics department, especially the help and timely support from Christopher Westerfelt, Jeffrey Addison and Matthew Busch. Without them, my projects can never be successful. I also appreciate the help and support from Prof. Calvin Howell, Prof. Thomas Mehen, Prof. Robert Behringer and Prof. Ashutosh Kotwal, who supervise my PhD study and serve as my committee members.

Lastly, I want to take this opportunity to thank my parents and my old friends. It is my parents who give me the opportunity to explore this exciting world. It is my parents who raise me up and teach me how to be a good man. It is my parents who are always around me and have faith in me no matter what has happened. It is with my deepest love that I dedicate this thesis to them. I am also the luckiest guy to have so many friends who care about me and share the happiness and sadness with me. Though I will not list all the names, you are in my heart all the time. Among all them, I want to say special thanks to Lin Li. I cherish the every single moment we spent together and those days are the most joyful memories I have ever had.

1

Introduction

1.1 Discrete Symmetries in Physics and Their Violation

There are three important discrete symmetry transformations in physics, charge conjugation (C), parity (P), and time reversal (T). Charge conjugation changes a particle into its anti-particle; P reverses the space coordinates; T reverses the direction of time. It was believed for some time that interactions between particles are preserved under these transformations so that the form of the equation describing the physical process is unchanged. In 1956, Lee and Yang proposed the possibility that P may not be conserved in weak interactions and suggested some experiments to test their hypothesis [89].

In 1957, Wu and her collaborators carried out an experiment to measure the emitting electron angular distribution from the polarized ^{60}Co β decay [140]. In this experiment, the ^{60}Co was polarized by a strong external magnetic field at low temperature. The polarized ^{60}Co β emits electron via β decay. If P is preserved, the angular distribution of the emitting electron with respect to the spin direction of the ^{60}Co should be symmetric. However, their observation proves that this distribution is not symmetric and one always has more electrons on one side than the other, which is a direct evidence of P violation. Later in the same year, Garwin *et al.* [52] and Friedman *et al.* [48] also discovered C violation in the meson decay. Though, P and C symmetries were violated in weak interactions, the combined transformation CP has been found to be a good symmetry until 1964.

In 1964, Christenson *et al.* found that CP is violated in the neutral Kaon decays [36]. The neutral Kaon has two CP eigenstates, K_1 and K_2 with CP=1 and CP=-1, respectively. Kaon can decay through the weak interaction, by which K_1 only decays to two pions ($\pi^0\pi^0$ and $\pi^+\pi^-$), and K_2 only decays to three pions ($\pi^0\pi^0\pi^0$ and $\pi^+\pi^-\pi^0$). The lifetime of the neutral Kaon has two distinct values, $\tau_L = 5.17 \times 10^{-8}$ s and $\tau_S = 8.93 \times 10^{-11}$ s [142]. Before the discovery of the Christenson *et al*, people believe that $K_L = K_2$ and $K_S = K_1$. In their experiment, they found that occasionally, K_L can decay to two pions with a branching ratio of 2×10^{-3}, which violates CP because of different CP values prior and after the decay. In other words, K_L and K_S are not equivalent to K_2 and K_1 and they are actually a mixture of the two CP eigenstates, K_2 and K_1.

$$K_S = \frac{1}{\sqrt{1+\epsilon^2}}(K_1 - \epsilon K_2) \tag{1.1}$$

$$K_L = \frac{1}{\sqrt{1+\epsilon^2}}(K_2 + \epsilon K_1), \tag{1.2}$$

where $\epsilon = 2 \times 10^{-3}$, the mixing parameter. The CP violation due to the mixture of CP eigenstates is also known as indirect CP violation. Later, CP violation was also discovered in neutral B Meson decays. Direct CP violation has also been seen in the neutral Kaon decay and more details can be found in [107]. These observed CP violations can be fully explained by the complex phase in the Cabibbo-Kobayashi-Maskawa (CKM) matrix in the standard model (SM) (more details can be found in the next section). Two dedicated precision experiments on neutral B Meson decay

(Belle at KEK Japan [2] and BaBar at SLAC USA) [7] were carried out to provide precise determination of some of the matrix elements in the CKM matrix.

Although P and CP symmetries are violated, the combined CPT transformation is still believed to be a good symmetry because of the CPT theorem [127, 128]. The theorem states that the CPT is always conserved if assuming the validity of the more fundamental physics principle, such as Lorentz invariance, hermiticity of the Hamiltonian and Bose/Fermi statistics. Hence, CPT violation would imply a breakdown of one or several of these fundamental principles, which is very unlikely. As a result, the conservation of CPT [20, 88, 127] also implies that the violation of CP definitely leads to the violation of T symmetry and vice versa.

1.2 Possible Sources of CP and T Violations in the Standard Model

The Standard Model (SM) is the most successful framework to describe the strong, electromagnetic and weak interactions [24]. Many predictions from SM agree with the experimental observations. There are two possible CP violation sources in SM. One is the CKM matrix in the weak interaction and the other is the θ term from the strong interaction. The weak interaction allows the quark to change its flavor and the interaction only happens among the quarks that have different electron charges. Therefore, the charge-raising weak current describing the interaction can be written as [63]

$$J^\mu = (\bar{u}\ \bar{c}\ \bar{t})\frac{\gamma_\mu(1-\gamma^5)}{2}U(d\ s\ b)^T,\ U = \begin{pmatrix} U_{ud} & U_{us} & U_{ub} \\ U_{cd} & U_{cs} & U_{cb} \\ U_{td} & U_{ts} & U_{tb} \end{pmatrix} \tag{1.3}$$

where γ_μ is the gamma matrices, $\gamma^5 = i\gamma^0\gamma^1\gamma^2\gamma^3$, and U is a 3×3 matrix that couples the u,c,t quarks with d,s,b quarks, also known as the CKM matrix. Because of the unitarity of the matrix and the physical insignificance of the phase associated with each quark field, there are only 4 independent variables charactering the matrix.

One way to parametrize the CKM matrix is to specify three mixing angles ($\theta_1, \theta_2, \theta_3$) and one complex phase (δ) [84]. If we use c_i and s_i to denote $\cos(\theta_i)$ and $\sin(\theta_i)$, respectively, the CKM matrix can be written as

$$\begin{pmatrix} c_1c_2 & s_1c_2 & s_2e^{-i\delta} \\ -s_1c_3 - c_1s_2s_3e^{i\delta} & c_1c_3 - s_1s_2s_3e^{i\delta} & c_2s_3 \\ s_1s_3 - c_1c_3s_2e^{i\delta} & -c_1s_3 - s_1s_2c_3e^{i\delta} & c_2c_3 \end{pmatrix}, \tag{1.4}$$

where $\theta_1 = 13.05 \pm 0.05$, $\theta_2 = 0.0201 \pm 0.011$, $\theta_3 = 2.38 \pm 0.06$, and $\delta = 1.20 \pm 0.08$ [4]. It can be shown that a nonzero complex phase δ will violate the CP symmetry by applying the CP transformation to the weak interaction Hamiltonian [63]. The CP asymmetry due to this complex phase can fully describe the CP violation in the neutral Kaon and B meson decay.

The strong interaction in the SM is described by Quantum Chromo-Dynamics (QCD). The generalized QCD Lagrangian has two terms, $L = L_{QCD} + L_\theta$ [138]. L_{QCD} describes the interaction among quarks and gluons which preserves the CP symmetry. The L_θ term violates CP symmetry, and it is written as [28, 19, 134, 72]

$$L_\theta = \theta \frac{g^2}{32\pi^2} G^{\alpha\mu\nu} \tilde{G}^{\alpha}_{\mu\nu}, \tag{1.5}$$

where $G^{\alpha\mu\nu}$ is the gluon field strength tensor, $\tilde{G}^{\alpha}_{\mu\nu} = \frac{1}{2}\epsilon_{\mu\nu\rho\sigma}G^{\alpha\mu\nu}$, g is the strong coupling constant and θ is a constant. The magnitude of the θ is unknown and it is an input to the SM, and can be only determined from the experiment. Naturally, one expects that θ should be close to the order of one.

Theoretical calculations have shown that the neutron electric dipole moment (nEDM) is proportional to θ and a rough estimation is nEDM $\approx \theta 10^{-16}$ e $\cdot$ cm [13, 42, 110]. The current experimentally upperlimit of the nEDM is 3×10^{-26} e $\cdot$ cm [11], indicating $\theta < 10^{-10}$ instead of close to 1. This is also known as the strong CP problem [34].

Some attempts have been made to explain why θ is so small, and among them, the most attractive approach is proposed by Peccei and Quinn in 1977 [104, 105]. They assume that the QCD Lagrangian has a global U(1) chiral symmetry and θ is actually a field instead of a constant. Once this global symmetry is broken by the instanton effect, it results a new particle, called an axion. Meanwhile, the θ parameter is fixed to zero. Once the axion was proposed, extensive searches have been conducted but without success till date. Though the axion can elegantly solve the strong CP problem and make the CP violation term L_θ vanish, its existence may also generate some other CP violation sources. One of these possible examples is the short-range spin-dependent macroscopic interaction, proposed by Moody and Wilczek [97]. This spin-dependent interaction happens between polarized spins and unpolarized masses. If this exotic force exists, it is mediated by an axion-like particle which is also a pseudoscalar boson. The new force will also violate both P and T symmetries and therefore CP symmetry. Hence, this could be a new source of CP violation in addition to the CKM matrix. It will be explained in the next paragraph that additional CP violation mechanism is crucial to explain the so-called baryon number asymmetry of our universe (BAU) [54].

Baryon number asymmetry is also known as matter/anti-matter asymmetry. We know that our universe is predominated by matters or baryons. By observation of the cosmic ray, we also know that the cosmic ray from far away of the universe is consistent with the interactions between ordinary matters, which indicates that the asymmetry holds throughout the entire universe [85]. Moreover, the observation of gamma ray backgrounds can be well explained by cosmic ray and normal matters [131]. Therefore, we do not need to resort to antimatter to explain them. All these evidences indicate that our universe is consisted of matter. However, since all the mass generating processes we know to date produce equal amount of matter and anti-matter, it is a mystery that why only matter is left in our universe. There must be some unknown mechanisms that generates this asymmetry at the very early stage of the evolution of the universe. It is shown by Sakharov that one of the necessary conditions for the BAU to happen is the C symmetry and CP symmetry violation [124]. If one use η to represent the baryon number asymmetry, it can be calculated as

$$\eta = \frac{n_B - n_{\bar{B}}}{n_B + n_{\bar{B}}}, \tag{1.6}$$

where n_B and $n_{\bar{B}}$ are the baryon and anti-baryon number density in the universe, respectively. Since baryon and anti-baryon will annihilate and generate photons γ, one can replace the total number of n_B and $n_{\bar{B}}$ with $n_B + n_{\bar{B}} = \sigma$, where σ is the number density of γ and can be estimated from the cosmic microwave background radiation. In the above equation, $n_B - n_{\bar{B}}$ can be approximated by n_B as $n_{\bar{B}} \approx 0$ today. Therefore, one can estimate $\eta \approx 10^{-10}$ [137, 85], which is 10 to 12 orders of magnitude bigger than the prediction from the SM assuming CKM matrix is the only source of CP violation [47]. This strongly suggests that there must be more CP violation sources we do not know, in order to be consistent with the BAU.

1.3 The Organization of this Thesis

My thesis research focuses on the search for the new sources of CP violations. We explore two possible sources: the experimental search of the neutron electric dipole moment (nEDM) and the axion-like particle mediating the spin-dependent exotic short-range force. The nEDM is a model-independent quantity, which provides an excellent way to examine existing models, including the SM and those that explore physics beyond it. It could also provide insights into the new sources of CP violation, which may help people understand the BAU. Several experiments have attempted to measure the nEDM for the past 6 years [11, 46, 65, 114, 118]. In 2002, a new nEDM experiment was proposed in the USA [100]. The goal of the new nEDM experiment is to improve the sensitivity of the measurement by two orders of magnitude. A country-wide collaboration is formed to carry out the project and Duke University is part of the collaboration. I will discuss the nEDM in general in Chapter 2. It includes a brief discussion of the previous nEDM experiments and their techniques, and the introduction of the novel techniques used in the newly proposed nEDM experiment. In Chapter 3, I will discuss about the ^{3}He injection simulation and the SQUID implementation for the nEDM experiment. In Chapter 4, two independent studies of the longitudinal (T_1) and transverse relaxation time (T_2) of the polarized ^{3}He are presented. T_1 and T_2 are the two most important parameters associated with polarized ^{3}He. They characterize how fast the polarized ^{3}He depolarized longitudinally and transversely. Therefore, these studies are closely related to the nEDM experiment, as they have a great influence on the sensitivity and the measurement time.

The other approach to probe possible new CP violation sources is the search of short-range and spin-dependent force. This will be presented in Chapter 5. As discussed previously, the existence of the axion can solve the strong CP problem naturally. If the short-range and spin-dependent force exists, this force will violate both P and T symmetries and the interaction will be mediated by an axion-like particle. It is of great importance to look for this axion-like particle, as the interaction is different from the four fundamental forces in physics. It also provides additional CP violation sources in addition to the strong and weak interactions. During this study, we use a high pressure spin-polarized ^{3}He target cell. Because of the extremely thin glass window of the cell and the technique we have developed, the sensitivity of our experiment can be potentially two orders of magnitude better than that of existing experiments. Chapter 6 concludes my thesis and a future outlook on the short-range force experiment is also presented.

2

The nEDM Experiment

2.1 Neutron Electric Dipole Moment and the Previous nEDM Experiments

In this section, I will first show how is nEDM related to the CP violation. Then, I will discuss previous nEDM experiments which utilized various experimental techniques. The limits of those experiment will also be discussed. The next section will be dedicated to the new nEDM experiment proposed in the USA. This covers the novelty and working principles of the new experiment as well as a comparison of the new experiment with previous ones.

2.1.1 What is nEDM and What Is It Predicted from the Theory?

The electric dipole moment characterizes a charge distribution, and it is mathematically defined as

$$\vec{d} \equiv \int \vec{x} q(\vec{x}) d^3x, \tag{2.1}$$

where $\vec{x}$ is the position vector and $q(\vec{x})$ is the charge distribution. Though neutron is a charge neutral particle, it can acquire a dipole moment if the positive charge and negative charge distribution do not overlap with each other perfectly. Theoretically, it can be shown that a nonzero θ term in Eq. (1.5) will lead to a nonzero nEDM [87, 146, 115].

Here I present a simple physics interpretation to illustrate how a nonzero nEDM can violate CP and T symmetry. Given a non-degenerate system in its ground state, such as a neutron, the only vector that denotes the energy levels of the system is the spin $\vec{S}$. If the neutron is placed in a magnetic field $\vec{B}$, the ground state will split into two states, $E^+ = E_0 + \mu B$ and $E^- = E_0 - \mu B$, where E_0 is the energy of the ground state. The two states become non-degenerate. If the neutron also has a EDM $\vec{d}$, it will possess a second vector to denote its state. Consequently, for either energy state E^+ or E^-, we have another degree of freedom $\vec{d}$ other than the spin $\vec{S}$ to characterize the system. With different angles between $\vec{d}$ and $\vec{S}$, the system always has the same energy. This means the ground state is degenerate, contradictory to the assumption that the ground state of the neutron is non-degenerate. To eliminate the contradiction, $\vec{d}$ must be in the same direction as the $\vec{S}$, i.e. $\vec{d} = d\frac{\vec{S}}{S}$ [82].

Under P transformation, $\vec{d}$ will change sign, whereas $\vec{S}$ is unchanged. Similarly, under T transformation, $\vec{d}$ is unchanged, whereas $\vec{S}$ changes sign. Hence, under P and T transformation, the left hand side and right hand side of $\vec{d} = d\frac{\vec{S}}{S}$ change in different ways. In order for this equation to be valid, we are left with two possibilities. They are either d is zero or P and T symmetries are violated.

The SM prediction of the nEDM is extremely small (in the range from 10^{-32} to 10^{-30} e$\cdot$cm [83, 93, 53]). The small value of the nEDM arises from three loop Feynman diagrams given the CKM matrix is the only source of the CP violation. Beside the CP violating complex angle in the CKM matrix, other CP violation sources or mechanisms can also contribute to the nonzero nEDM. Various models, such as supersymmetry model(SUSY) [16, 14, 45, 81], left and right symmetry model [22, 96] and

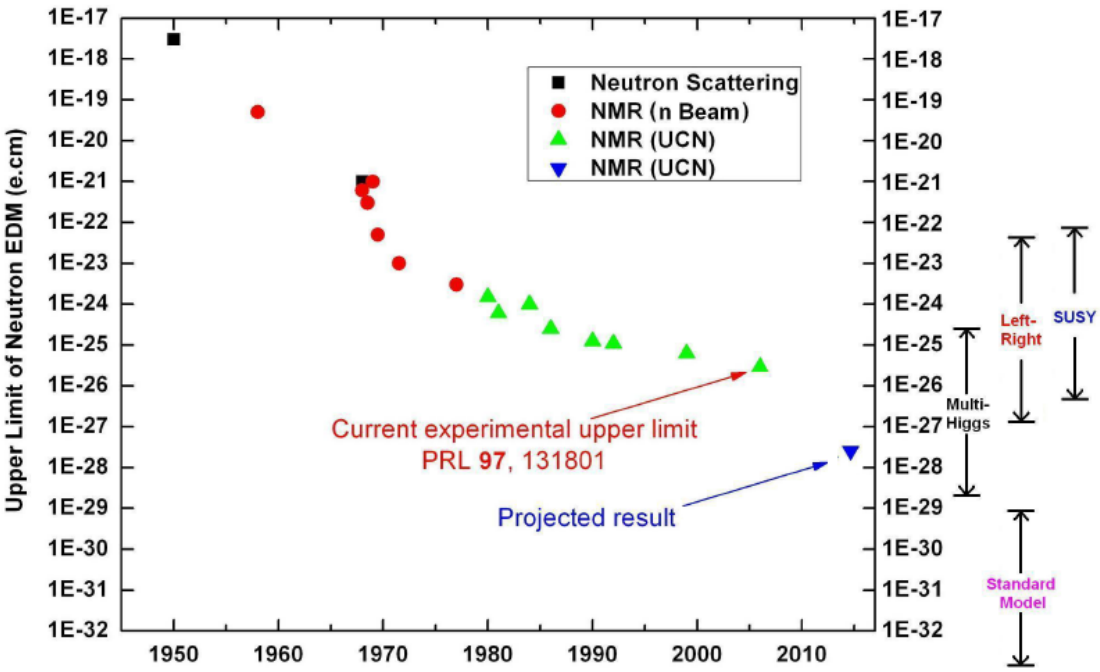

FIGURE 2.1: The world data on the upperlimit of the experimental value of the nEDM. The theoretical prediction from different models are plotted on the right of the figure. The proposed upperlimit of the new experiment is plotted as the blue downward triangle.

multi Higgs model [18, 80, 23, 15, 62] all have their own predictions of the nEDM which are much larger than the SM's prediction, Figure 2.1 [106]. Since the very first measurement on nEDM obtained in 1950 [113], the upperlimit of the nEDM has been reduced by eight orders of magnitude. The current best upperlimit is 2.9×10^{-26} e·cm [11], which is still several orders of magnitude larger than the SM's prediction. A new nEDM experiment was proposed in 2002 which is aimed at improving the sensitivity by two orders of magnitude [100]. With this improved sensitivity, the experiment will have a major impact on distinguishing different theoretical models, shown on the right panel in Figure 2.1.

2.1.2 Previous nEDM Experiments and Their Measurement Techniques

Three different techniques have been used in the past to measure the nEDM. They are neutron scattering [113, 65], nuclear magnetic resonance (NMR) using neutron beams [114, 46] and NMR on ultra-cold neutrons [11]. In neutron scattering, neutrons in a beam are scattered by the electrons in a solid lead target. The dipole moment is extracted assuming that the neutron-electron interaction is due to the nEDM. A better approach, in terms of sensitivity, involves a magnetic resonance technique. In this approach, a magnetic field together with a very strong electric field is applied to the neutron. Since the nEDM and the spin are in the same direction, the magnetic field and the electric field are applied either parallel or anti-parallel to each other. In this way, the Hamiltonian for the interaction can be written as

$$H = \mu_n \hat{S} \cdot \vec{B} \pm d_n \hat{S} \cdot \vec{E}, \tag{2.2}$$

where μ_n is the magnetic dipole and d_n is the electric dipole of the neutron. The "+" sign means the $\vec{E}$ field is parallel to the $\vec{B}$ field and the "-" sign means the $\vec{E}$ field is anti-parallel to the $\vec{B}$ field. As the neutron spin can only be aligned parallel or anti-parallel to the magnetic field, the system has two energy levels and consequently, the resonance frequency is determined by the spacing between the two levels

$$f_n = (2\mu_n B \pm 2d_n E)/h, \tag{2.3}$$

where h is the plank constant. As the resonance frequency shifts when the $\vec{E}$ field is flipped, the nEDM d_n can be extracted from the frequency difference $d_n = \frac{\Delta f_n h}{4E}$. When using a neutron beam, neutrons will pass two parallel plates. Between the two plates, the magnetic field and electric field are applied, so that the velocity of the neutron and the direction of the fields are perpendicular to each other. The best upperlimit obtained from this method is $d_n < 3 \times 10^{-24}$ e·cm [46]. One of the biggest systematic uncertainties that limits the sensitivity is the mis-alignment between the beam and the field. In the neutron rest frame, neutron will see an additional magnetic field $\vec{B} = \frac{1}{c}\vec{v} \times \vec{E}$ if the electric field $\vec{E}$ and the magnetic field $\vec{B}$ are not perfectly parallel to each other. This additional field shifts the resonance frequency as well and therefore gives a false nEDM. As a thermal or cold neutron beam usually has a velocity around 10^3 m/s, this $\vec{v} \times \vec{E}$ effect can be greatly reduced if the neutron velocity can be decreased. This observation leads to the next technique, NMR on ultra-cold neutrons (UCN).

The UCNs have much smaller velocities, less than 10 m/s, which greatly suppress the $\vec{v} \times \vec{E}$ effect. More interestingly, the energy of the neutron is so low that they can no longer penetrate many materials. They can be therefore safely stored in a bottle similar to the storage of a regular gas. This provides two additional advantages for the NMR measurement. The first advantage is that the velocity of the bottled UCNs is random in direction. The randomness of the velocity can further suppress the $\vec{v} \times \vec{E}$ effect. Another advantage is that bottled UNCs can have a much longer interaction time (> 500 seconds) with the $\vec{B}$ and $\vec{E}$ field than the neutrons in a beam (< 1 second). Therefore, it greatly increases the sensitivity by accumulating more phase changes from flipping the $\vec{E}$ field. The nEDM measured from UCNs provides the most stringent limit to date. The latest result using UCNs was done at Institute Laue-Langevin (ILL) with an upperlimit 4×10^{-26} $\mathrm{e} \cdot \mathrm{cm}$ [11].

2.2 The New nEDM Experiment at SNS

The newly proposed nEDM experiment in USA also utilizes the UCNs. However, the UCNs are produced in the superfluid ^{4}He, which is different from the previous UCN generating method. The precession frequency measurement of the neutron is also different from the previous techniques. These will be discussed in detail in the following sub-sections.

2.2.1 Experimental Techniques

The new nEDM experiment will be carried out using the Spallation Neutron Source (SNS) at the Oak Ridge National Lab (ORNL). The new experiment also relies on the NMR technique and UCNs. The biggest difference from the previous experiments is that polarized UCNs, polarized ^{3}He atoms and superfluid ^{4}He form a three-component fluid stored in the measurement cell where the NMR measurements take place. The presence of ^{3}He and ^{4}He are crucial and indispensable to the experiment.

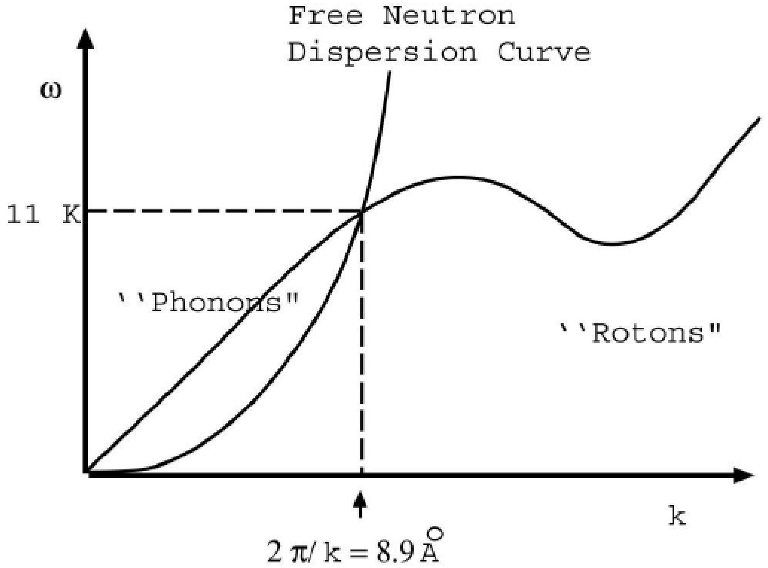

FIGURE 2.2: Dispersion curves of superfluid ^{4}He and the free neutron. The x axis is the momentum and y axis is the energy. The neutron curve is a parabola and the ^{4}He dispersion curve is linear at low energy.

The superfluid ^{4}He serves three purposes. Firstly, the superfluid ^{4}He will down-scatter the cold neutrons to the UCNs in the measurement cell [59, 58]. Polarized cold neutrons are produced from the SNS at ORNL. Cold neutrons can easily enter the measurement cell made of acrylic because of their relatively large kinetic energy. Once they enter the cell, they will collide with superfluid ^{4}He atom through the so called down-scattering process. This down-scattering is best explained by the dispersion curves of the neutron and superfluid ^{4}He, see Figure 2.2 [139]. When a collision takes place between neutron and ^{4}He, the conservation of energy and momentum must be satisfied. This requires that the collisions can only happen when the energies of the two particles are at the two points, where the two dispersion curves intersect with each other. One point of the intersections is at the origin and the other is at $2\pi/k^* = 8.9$ Å, which is equivalent to the neutron energy $E^* = 11$ K and velocity $v = 440$ m/s. Hence, only cold neutrons with this energy can be slowed down by ^{4}He atoms with energy close to zero. As a result, the energies of neutron and ^{4}He are switched, and the neutron energy becomes close to zero ($E < 0.13$ μeV and $v < 10$ m/s). This UCN production process is also called superthermal process. Note that the reverse process can also happen, i.e. the UCN can be up-scattered to cold neutrons by absorbing energy from ^{4}He. However, the rate of this process is much smaller because the number of ^{4}He at high energy is much smaller than the number of ^{4}He at low energy due to the Boltzmann distribution, $e^{-E_{^4He}/kT}$ when the temperature of ^{4}He is below 1 K [82]. As the up-scattering can be ignored, the production rate of the UCNs inside the superfluid ^{4}He is approximately 0.3 UCN/cm$^3\cdot$sec. After 500 seconds of UCN production, the UCN density will be 150 UCNs/cm^3.

The second purpose of the superfluid ^{4}He is to produce scintillation light when ^{3}He and neutron react in the ^{4}He bath. I will defer the explanation of this process to the next two paragraphs where I discuss the application of ^{3}He. The third purpose of the superfluid ^{4}He is to work as dielectric material so that a very high electric field ($\sim$ 50 kV/cm) can be applied to the neutrons [56]. In the proposed experiment, there are actually two measurement cells, see Figure 2.3. A high voltage electrode is sandwiched by the two measurement cells and the two cells sit between two ground electrodes [100]. If a fixed $\vec{B}$ field is applied, the $\vec{E}$ field in one cell is parallel to the $\vec{B}$ field; and in the other cell, the $\vec{E}$ field is anti-parallel to the $\vec{B}$ field.

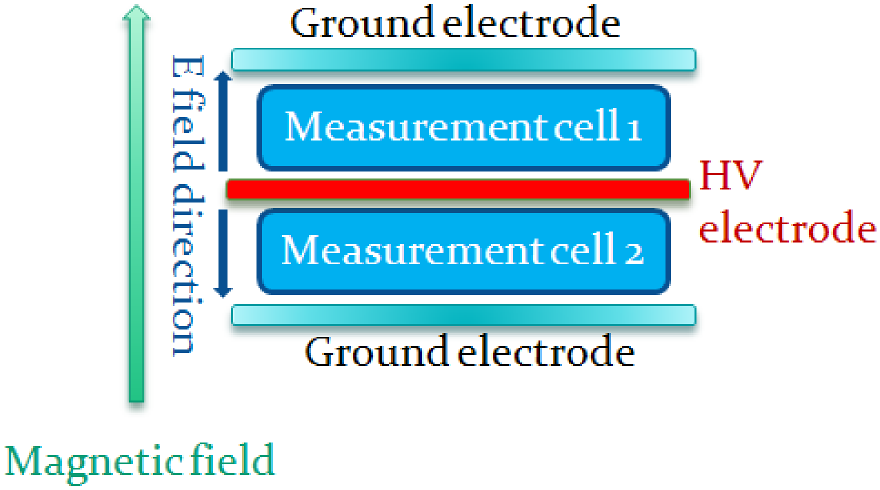

FIGURE 2.3: Two measurement cells containing the polarized UCNs, ^{3}He and superfluid ^{4}He. The magnetic field direction is fixed and the electric fields in the two cells have opposite directions.

In this configuration, the frequency differences in the two cells can be measured simultaneously. If we use f_p and f_a to denote the frequency difference in the parallel and anti-parallel cases, respectively, the nEDM can be calculated as $d_n = h(f_p - f_a)/4E$. In this way, the systematic uncertainty from the flipping of the $\vec{E}$ field is reduced and the overall measurement time is shortened as well.

More than 95% polarized ^{3}He is used as a co-magnetometer to monitor the magnetic field fluctuation in situ [116]. Any frequency shift of the neutron due to the magnetic field fluctuation can be removed from the frequency measurement of ^{3}He, given the knowledge of their respective gyromagnetic ratios. One may think that the $\vec{E}$ field will also shift the ^{3}He frequency because ^{3}He also has an EDM. This is not the case here because of the Schiff effect [51, 125] that the electron cloud around the ^{3}He nucleus can shield the nuclues from the influence of the external electric field. The shielding factor is about 2×10^7 [125], therefore the effect of the external electric field on ^{3}He can be ignored.

Polarized ^{3}He also has another important task in this experiment. Neutrons and polarized ^{3}He atoms have a spin-dependent reaction,

$$\vec{n} + {}^3\vec{He} \rightarrow p + t + 764 \text{ keV} \tag{2.4}$$

The cross-sections of this reaction with spins in parallel or anti-parallel are $\sigma_p = 59$ b and $\sigma_a = 11$ kb, respectively [79, 117, 150]. If we let the polarized neutron and ^{3}He precess in a magnetic field, they will precess at different speeds due to their different gyromagnetic ratios. The angle between the two spins varies as a function of time. As a result, the cross-section or equivalently the reaction rate also varies as a function of time. As this reaction happens in the measurement cell filled with superfluid ^{4}He at $\sim$ 400 mK, the recoiled proton and triton can generate scintillation light in the superfluid ^{4}He [94]. As the cross-section of the reaction changes sinusoidally, the amplitude of the scintillation light is modulated by a sinusoidal function with the frequency equal to the frequency difference between the two species $\Delta f = f_n - f_{^3\mathrm{He}}$. More specifically, the amplitude of the scintillation light can be expressed as [100, 82]

$$A(t) = A_{bg} + N \exp^{-\frac{t}{\tau_n}} \left\{ \frac{1}{\tau_\beta} + \frac{1}{\tau_{^3He}} \left[1 - P_{^3He}(t) P_n(t) \cos(2\pi \Delta f t + \phi) \right] \right\}, \tag{2.5}$$

where A_{bg} is the background, N is proportional to the number of UCNs in the cell, $1/\tau_n$ is the total loss rate of UCNs, including β decay with a decay constant $1/\tau_\beta$, wall loss and the average absorption by the ^{3}He with a decay constant $1/\tau_{^3\mathrm{He}}$, and $P_{^3\mathrm{He}}(t)$ and $P_n(t)$ represent the depolarization of the ^{3}He atoms and neutrons, respectively. In the equation, ϕ is an arbitrary angle between ^{3}He and neutron, which depends on the initial position of the ^{3}He spin and neutron spin. By detecting the frequency of the light amplitude Δf and the precession frequency of ^{3}He $f_{^3\mathrm{He}}$, the precession frequency of the neutron can be extracted $f_n = \Delta f + f_{^3\mathrm{He}}$.

However, the generated scintillation light has a very short wavelength ($\sim$ 80 nm), it cannot be detected directly by the photo multiplier tube (PMT). To overcome this difficulty, the inside of the cell wall is coated with deuterated TetraPhenyl Butadiene-doped deuterated PolyStyrene (dTPB-dPS) which can shift the wavelength of the scintillation light to $\sim$ 430 nm [25]. At this ultraviolet (UV) region, the light can be easily detected by the PMT.

In practice, two different techniques are proposed to measure the neutron precession frequency. The first method involves the measurement of the ^{3}He precession frequency and the frequency of the scintillation light so that the neutron precession frequency is extracted from $f_n = \Delta f + f_{^3\mathrm{He}}$ as described. An alternative technique is called "dressed spin". The idea is that we can artificially change the magnetic moment of spins by applying a transverse ac field, also called dressing field. By carefully choosing the amplitude and frequency of this dressing field, ^{3}He and neutron can have the same magnetic moment so that they will precess at the same frequency. This is also known as "critical dressing", in which the amplitude of the dressing field B_{ac} and frequency of the dressing field ω_{ac} satisfy the relationship $\gamma_n \frac{B_{ac}}{\omega_{ac}} \approx 1.19$ [82], where γ_n is the neutron gyromagnetic ratio. In the "critical dressing", the fluctuation of the magnetic holding field is theoretically irrelevant, and one only needs to measure the frequency of the scintillation light to extract nEDM. More detailed discussion of the dressed spin technique can be found in [37]. The sensitivity of these two methods are still under study, and both of them will be implemented in the final nEDM experiment to extract nEDM.

The polarized ^{3}He atoms are produced from the atomic beam source (ABS) which has already been built at Los Alamos National Lab. The description of the ABS will be presented in Chapter 3. The entire nEDM apparatus consists of two parts, the upper cryostat and the lower cryostat, see Figure 2.4. The ABS is attached to the upper cryostat at a 45 degree angle. ^{3}He atoms are injected into the upper cryostat and collected in a collection volume sitting in the upper cryostat. Once enough polarized ^{3}He atoms are collected, they will be transfered as a whole into the lower cryostat where the two measurement cells are located. The polarized cold neutron beam is directly incident onto the two measurement cells filled with ^{4}He. Once the three component fluid is formed, the magnetic resonance measurement will start. The NMR measurement takes about five hundred seconds [100]. Once a measurement is done, the ^{3}He in the two measurement cells are flushed completely so that newly polarized ^{3}He can enter the cells. Then, another measurement cycle begins and these procedures are repeated for many times to obtain enough statistics. Because of the novel techniques adopted in this nEDM experiment, the UCN density is 50 times higher, the electric field is 5 times higher and the measurement time is 4 times longer. These differences lead to an improvement of the sensitivity on the upperlimit of the nEDM by two orders of magnitude, or 2.2×10^{-28} e $\cdot$ cm.

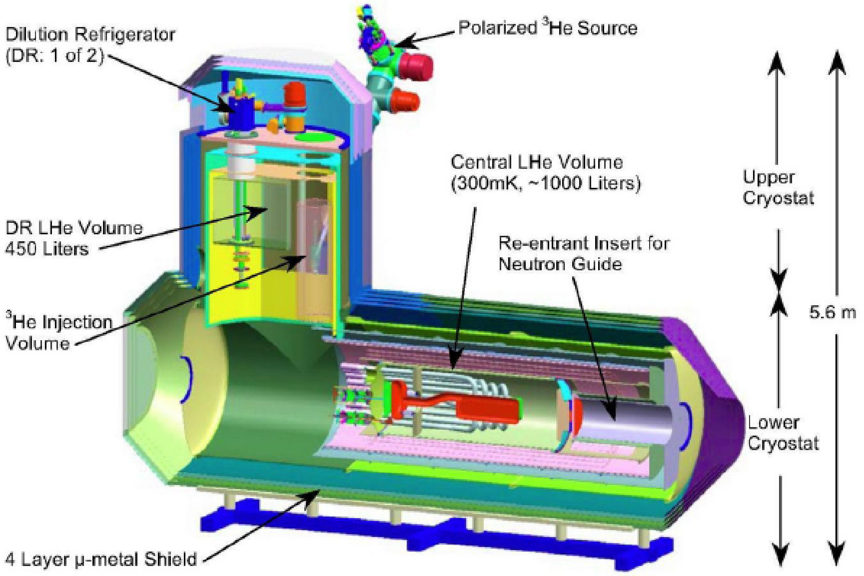

FIGURE 2.4: Schematic view of the nEDM experimental apparatus. Polarized ^{3}He atoms are injected into the upper cryostat from the ABS at a 45 degree angle. The two measurement cells are located in the lower cryostat. The lower cryostat also has a magnetic package, including electro-magnet and several layers of magnetic and superconducting shielding to improve the magnetic field uniformity in the measurement cells.

2.2.2 Our Role in the New nEDM Experiment

The Medium Energy Group at Duke, is in charge of the polarized ^{3}He injection for the nEDM experiment. As the polarized ^{3}He needs to travel along a rather complicated path in order to reach the measurement cell, the apparatus needs to be designed very carefully to ensure that the polarization of the ^{3}He is not lost during this process. We calculate the polarization of ^{3}He throughout the entire injection process using Monte-Carlo simulation. Given different apparatus designs, including geometries and magnets, the simulation yields different ^{3}He polarizations. The goal of the simulation is to assist the design so that when ^{3}He reaches the measurement cell, more than 95% of ^{3}He is still polarized. This study is presented in Chatper 3.

The other project taken on at Duke related to the ^{3}He injection is the SQUID implementation for the ^{3}He polarization measurement. SQUID stands for superconducting quantum interference device, which is a sensitive device to measure a magnetic flux. In the nEDM experiment, we need to measure the polarization of ^{3}He every time ^{3}He atoms are injected into the system. Since the ^{3}He density is extremely low ($\sim 10^{14}$ atoms/cc) [100], only SQUID is sensitive enough to measure the magnetic flux. At Duke, we built an apparatus to test the SQUID sensor and demonstrate that the SQUID indeed has the sensitivity to measure the ^{3}He signal at such a low density. This work is presented in the second part of Chapter 3.

2.3 Two Spin-off Results from the nEDM Projects

During the experiment of SQUID implementation, we found two interesting phenomena. One is that the longitudinal relaxation rate $1/T_1$ of the polarized ^{3}He has a pressure dependence, which has never been observed before. The other is that the transverse relaxation rate $1/T_2$ of the ^{3}He is much longer than the theoretical prediction. To clarify the first mysterious observation, we built a dedicated experiment to test the T_1 pressure dependence and also proposed a diffusion model to explain the observation. This work was published on *Physical Review A* as a rapid communication [Phys. Rev. A, Vol 83, 061401(R) (2011)].

Regarding to the second finding, I dug into the relaxation theories and discovered that the measured T_2 relaxation rate falls into the slow diffusion regime, which cannot be described by the usual ^{3}He relaxation result since it only applies to the fast diffusion regime. I developed a new approach to calculate both transverse and longitudinal relaxation rates of ^{3}He. This approach gives a general solution applicable to both diffusion limits. Moreover, it is also suitable for the intermediate regime, which greatly extends the scope of its application. This theoretical derivation together with experimental justification is published in *Physical Review A* [Phys. Rev. A, Vol 84, 053411 (2011)]. I will discuss these two works in detail in Chapter 4.

3

^{3}He Injection Simulation for the nEDM Experiment and the SQUID implementation for the Injection Test

Polarized ^{3}He atoms serve two purposes in the nEDM experiment. Firstly, polarized ^{3}He has a spin-dependent reaction with polarized neutrons, as shown in Eq. (2.4). This spin dependent reaction produces ultra-violet (UV) scintillation light in superfluid ^{4}He [94]. Since the light amplitude is modulated by the frequency difference between the neutron and ^{3}He, Eq. (2.5), one can determine the precession frequency of the neutron by measuring the oscillation frequency Δf of the scintillation light and the ^{3}He precession frequency $f_{^3\mathrm{He}}$.

Secondly, polarized ^{3}He works as a in situ co-magnetometer to monitor the overall magnetic field fluctuations. The precession frequency of ^{3}He is proportional to the magnetic holding field. Any field fluctuation will cause the ^{3}He precession frequency to fluctuate as well. By continuously monitoring the ^{3}He precession frequency, one of the biggest systematic uncertainties in the nEDM experiment can be compensated for.

Both of these two goals require a precise measurement of ^{3}He precession frequency. A traditional way to measure the precession frequency is nuclear magnetic resonance (NMR) technique. However, the number density of ^{3}He atoms in the nEDM experiment is extremely low (only 5×10^{14} atoms/cc or 1 million times smaller than the number density of 1 atm ^{3}He gas at 300 K), and the magnetic holding field in the nEDM experiment is also extremely small ($\sim$ 50 mG). These two factors make the traditional NMR technique impossible to detect the magnetic resonance signal. Therefore, superconducting quantum interference device (SQUID) will be used to measure the resonance signal because of its ultra-high sensitivity (10^{-15} T), especially at low fields.

In the proposed nEDM experiment [100], nearly 100% polarized ^{3}He atoms are generated from an Atomic Beam Source (ABS). The ABS is incorported with a series of quadruple magnets which work as a spin filter so that only ^{3}He atoms with one spin state can pass through them, and atoms with the other spin state will be deflected by the quadruple magnet. The deflected atoms will be pumped out of the system. After the magnets, polarized ^{3}He atoms are injected into the collection volume in the upper cryostat of the nEDM apparatus, see Figure 3.1.

The collection volume is used to collect enough ^{3}He atoms and check their polarization. Once enough polarized atoms are collected, they will be transfered to the measurement cell in the lower cryostat of the nEDM apparatus, where the actual measurements take place. As the polarized ^{3}He atoms have to travel through rather long paths in order to arrive at the measurement cell, the changing magnetic fields experienced by the ^{3}He along its path may depolarize the spin. Hence, one must make sure that polarization loss is negligible during the injection process.

The first section of this chapter is devoted to the study of the ^{3}He injection simulation. This simulation is used to guide the magnetic field design, so as to achieve negligible polarization loss during the injection process. The second section of this

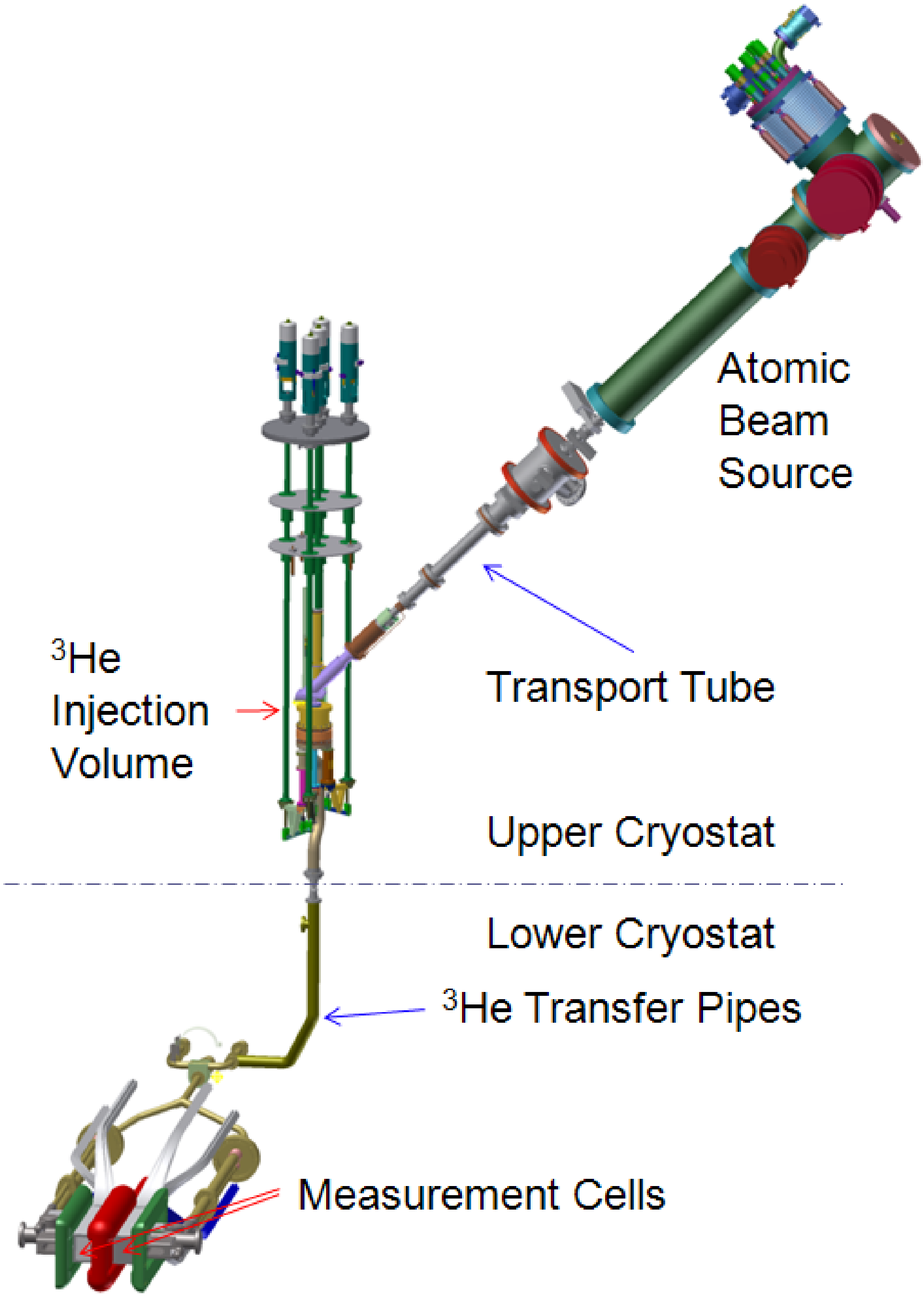

FIGURE 3.1: The schematic of the ^{3}He transport. All magnets and magnetic shieldings are not shown.

chapter will be devoted to the SQUID implementation in the collection volume. The SQUID sensor is planted in the collection volume to monitor the polarization of ^{3}He during the injection. The goal of this study is to demonstrate that the SQUID sensor is sensitive enough to measure the ^{3}He signal under the actual nEDM experimental conditions.

3.1 ^{3}He Injection Simulation for the neutron Electric Dipole Moment Experiment

The ABS exit is connected to a transport tube covered by three layers of μ metal shieldings (μ metal is an alloy which has very high magnetic permeability). The other end of the tube is connected to the injection volume in the upper cryostat. The inside of the transport tube is pumped to a high vacuum of approximately 10^{-8} torr. This high vacuum is to ensure that the scattering of the ^{3}He atoms from the ^{4}He molecules is negligible. Three sets of solenoid coils are installed around the transport tube to provide a magnetic holding field to maintain the polarization of the ^{3}He spins. The stray fields from these solenoids are confined in the transport tube by the μ metal shielding so that they have minimum effects on other parts of the apparatus.

The entire ABS and the transport tube is tilted by 45 degree with respect to the ground and the magnetic field at the exit of the ABS is along the axis of the transport tube. At the other end of the transport tube, the collection volume is connected, and it sits in a 24 turns cosθ coils [12] which provide a very uniform magnetic field along the horizontal direction ($\hat{x}$ direction). A schematic diagram showing all the coils are presented in Figure 3.2.

The field at the ABS exit is approximately 700 Gauss; whereas the field inside the 24 cosθ coils is approximately 50 mG. Hence, the transport field at the ABS end needs to match the 700 G field from the ABS quadruple magnet and when getting

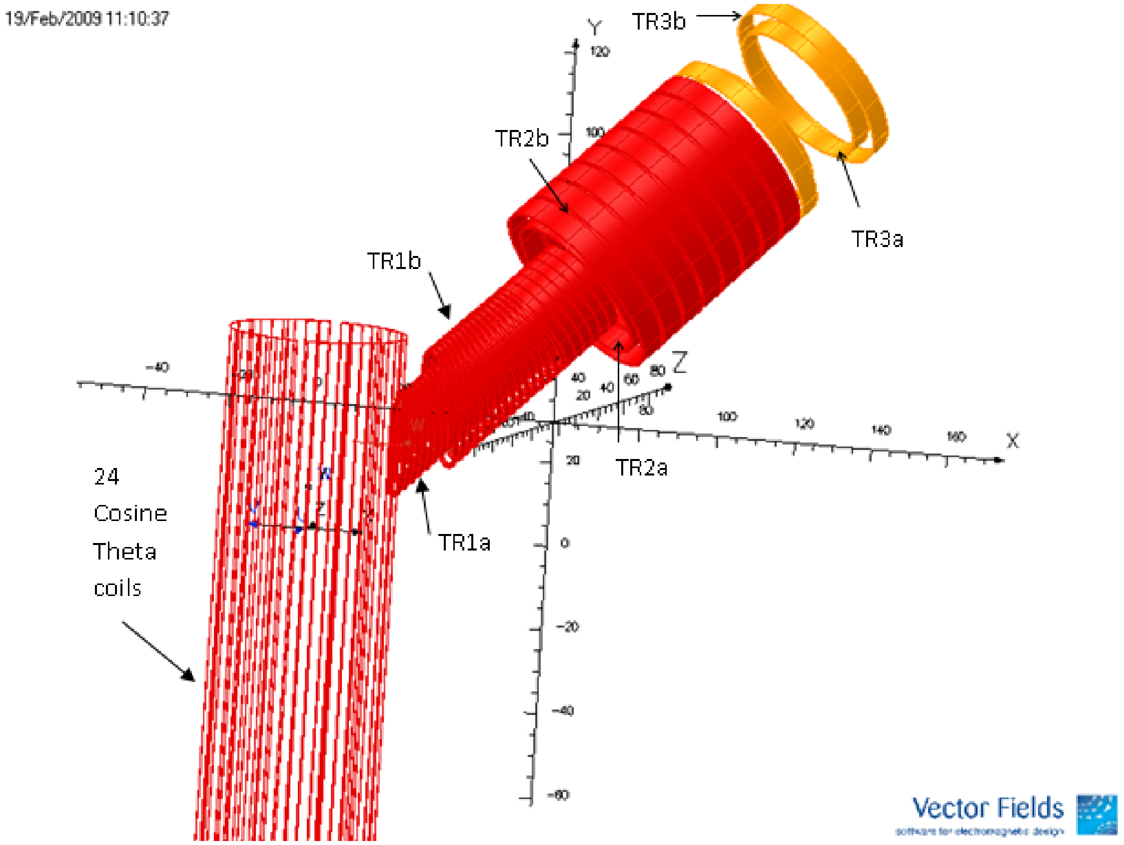

FIGURE 3.2: Three sets of spin transport coils, TR1a, TR2a and TR3a. Each set of these coils has its compensating coils, TR1b, TR2b and TR3b, to actively shield the field. The vertical lines are the 24 turns $\cos\theta$ coils at the collection volume. This is still an ongoing project and the coil design has not been finalized yet.

close to the collection volume, this field needs to be tapered down to 50 mG to match the field of the cosθ coil. Moreover, because of the 45 degree angle between the field at ABS exit and the field in the collection volume, the polarized ^{3}He spins have to rotate by 45 degree during their injections. This task must be accomplished by the transport field as well. There are totally three sets of transport coils, TR1, TR2 and TR3, and each set has two coils, denoted by “a” and “b”. For example, the TR1 set has TR1a and TR1b, see Figure 3.2. The current in each set of the coils can be adjusted independently so that the field can be tapered down to the desired level. The compensating coils, TR1b, TR2b and TR3b, are added to the outside of the primary coils, TR1a, TR2a and TR3a. The current in those compensating coils runs in the opposite direction to the current in the inner coils. This current configuration is called active shielding [78]. It ensures that the stray field outside the magnet rolls off quickly enough so that it will not saturate the magnetic shielding outside the transport tube. The rotation of the field is realized by changing the winding direction of the coil TR1a and TR1b, which can be easily seen in Figure 3.2. In principle, this is how the transport coils are designed. To check whether the designed field was able to maintain at least 95% polarization of ^{3}He during the injection, I carried out a Monte Carlo simulation to compute the average polarization of ^{3}He at the collection volume given any particular transport magnetic field.

The Monte Carlo simulation consisted of three parts. The first part simulated how the 100% polarized ^{3}He atoms were produced at the ABS. This part of the code generated a velocity and position distribution of ^{3}He atoms at the exit interface of the ABS. The second part of the code took the velocity and position distribution from the first part as an input and simulated how many of those generated atoms from ABS could finally pass through the transport tube and arrive at the collection volume. The atoms that can successfully arrive at the collection volume was recorded and this piece of information was used in the third part of the simulation. The third part simulated the precession of individual ^{3}He spin in the magnetic field along its path to the collection volume. Once the atom entered the collection volume, the angle between the spin and the magnetic field was recorded. After simulation of enough samples, the average polarization of ^{3}He was extracted. A detailed description of each part of the simulation is presented in the following subsections.

3.1.1 Generating Polarized ^{3}He Atoms from ABS

Nearly 100% polarized ^{3}He atoms are produced by letting ^{3}He atoms pass through magnetic field gradients. Due to the relatively small force which can be applied to the ^{3}He through its nuclear magnetic moment, the ^{3}He source is operated at 1 K to decrease its kinetic energy and an interaction region of approximately 1 m long is also chosen so that the total time for ^{3}He spins in the interaction region is increased. As a result, the atoms with the right spin state can be correctly selected by the field gradients [100]. The simulation assumes that the velocity of the emitting ^{3}He follows Boltzmann distribution

$$I(v) = I_0 \frac{2}{\alpha^4} v^3 e^{-v^2/\alpha^2}, \tag{3.1}$$

where $\alpha^2 = 2k_B T/m$, k_B is the Boltzmann constant, m is the mass of ^{3}He. The angular distribution of the emitting atoms I_0 has the form $dI_0/d\Omega = n\bar{v}A\cos(\theta)/4\pi$, where n and A are the source density and the aperture area, $\bar{v}$ is the average velocity of ^{3}He at temperature T, and θ is the azimuthal angle measured from the normal of the aperture. The emitted ^{3}He atoms will pass through a nozzle and enter the 1 m quadruple magnetic field region where the right spin state is selected. A schematic view of the ABS, including ^{3}He source, nozzle and quadruple magnets, is shown in Figure 3.3.

When ^{3}He spins are in the interaction region (quadruple magnetic field), the force on the spin can be expressed as [100]

$$\vec{F}_B(\vec{r}) = \pm\mu \frac{B_0}{R_a} \frac{1}{\sqrt{1 + (B_z/B_0)^2 (R_a/r)^2}} \hat{r}, \tag{3.2}$$

where r is the distance from the axis of the polarizer to the atom, R_a is the polarizer aperture, B_0 is the magnitude of the field near the surface of one of the magnets and ± refers to the two spin states anti-parallel and parallel to $\vec{B}$, respectively. When spins are anti-parallel to the field, the force is pointing outward in the radial direction. In this case, the atom will move away from the center of the polarizer and fail to pass. In the other case when spins are anti-parallel to the field, the force is always pointing towards the center. This restoring force tries to keep the atoms at the center

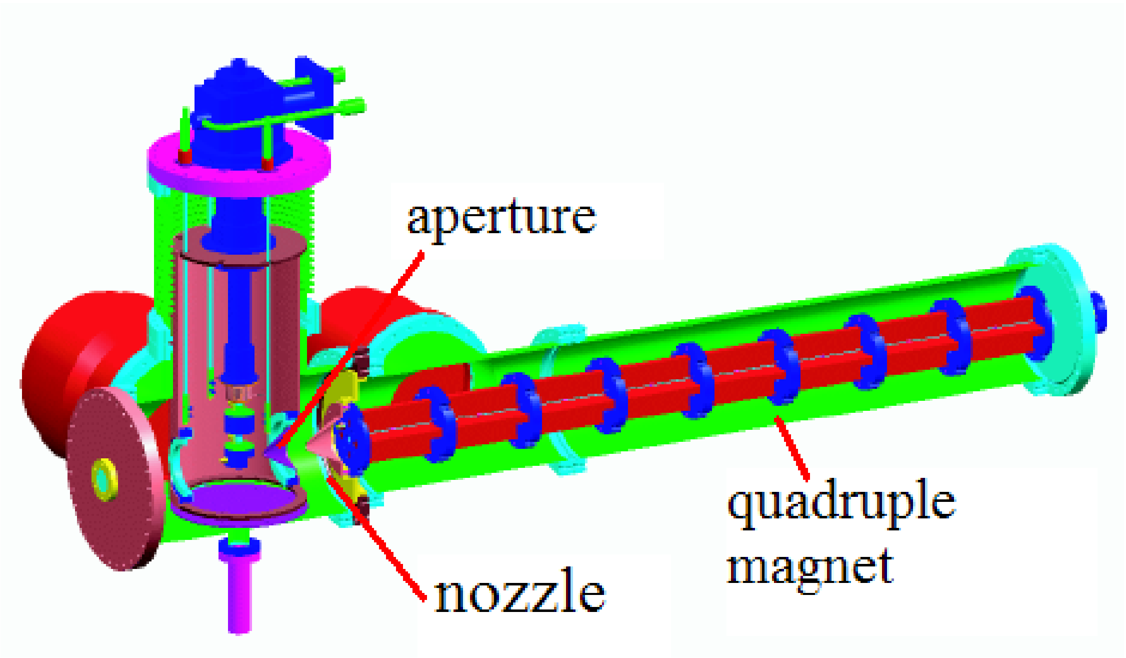

FIGURE 3.3: Cutaway view of the polarized ^{3}He source. The quadruple magnets are in the 1 m long green tube, and the exit of the ABS is at the end of the tube on the right.

of the polarizer and the pass rate will be much higher than the anti-parallel case. The effects of gravity and of bending of the polarizer bore can be expressed as

$$\vec{F}_g = -m(g + \frac{v_z^2}{R_p})(\sin(\phi)\hat{r} + \cos(\phi)\hat{\phi}), \tag{3.3}$$

where g is the acceleration due to gravity, v_z is the axial velocity of the atom, ϕ is the azimuthal angle, and R_p is the radius of curvature of the "bent" polarizer. Combining Eq. (3.2) and Eq. (3.3), one can obtain the equation of motion in cylindrical coordinates as

$$\begin{aligned}\vec{F}_t &= \vec{F}_B + \vec{F}_g = m\ddot{\vec{r}} \\ &= m((\ddot{r} - \dot{r}\dot{\phi}^2)\hat{r} + (r\ddot{\phi} + 2\dot{r}\dot{\phi})\hat{\phi} + \ddot{z}\hat{z}).\end{aligned} \tag{3.4}$$

The relevant dimensions and parameters used in the simulation are:

- source aperture radius $R_s = 6$ mm

- separation between source aperture and polarizer entrance aperture $s = 22$ cm
- polarizer aperture (or bore radius) $R_a = 7.5$ mm
- polarizer length $L = 1.25$ m
- the source temperature $T = 1$ K
- the magnetic fields $B_0 = 0.75$ T and $B_z = 0.03$ T

The simulation result is shown in Figure 3.4. This calculation suggests that the probability of a ^{3}He atom with the right spin state to pass the polarizer is $P_+ = 0.519$. The probability for an atom with wrong spin state to successfully pass the polarizer is $P_- = 0.00005$. The polarization can be therefore calculated as

$$P = \frac{P_+ - P_-}{P_+ + P_-}. \tag{3.5}$$

For $P_+ = 0.519$ and $P_- = 0.0005$, the above equation gives $P > 0.998$. In addition to the output polarization, the simulation also generates the velocity distribution of ^{3}He atoms at the exit of the ABS. This distribution is used to calculate how many atoms can travel through the transport tube and reach the collection volume, which is shown in the next section.

3.1.2 Spin Transport in the Transport Tube

The exit interface of the ABS is connected to the transport tube with a length ranging from 1.3 to 1.9 m, as shown in Figure 3.5. Since the transport magnetic field design is not finalized, the length of the transport tube is not a fixed parameter. As the ^{3}He beam from the ABS exit has a divergence, a longer transport tube tends to block more atoms from entering the collection volume. The transport tube cannot be too short because the ABS quadruple magnet will be too close to the collection volume such that the strong field can interfere with the polarization measurement at

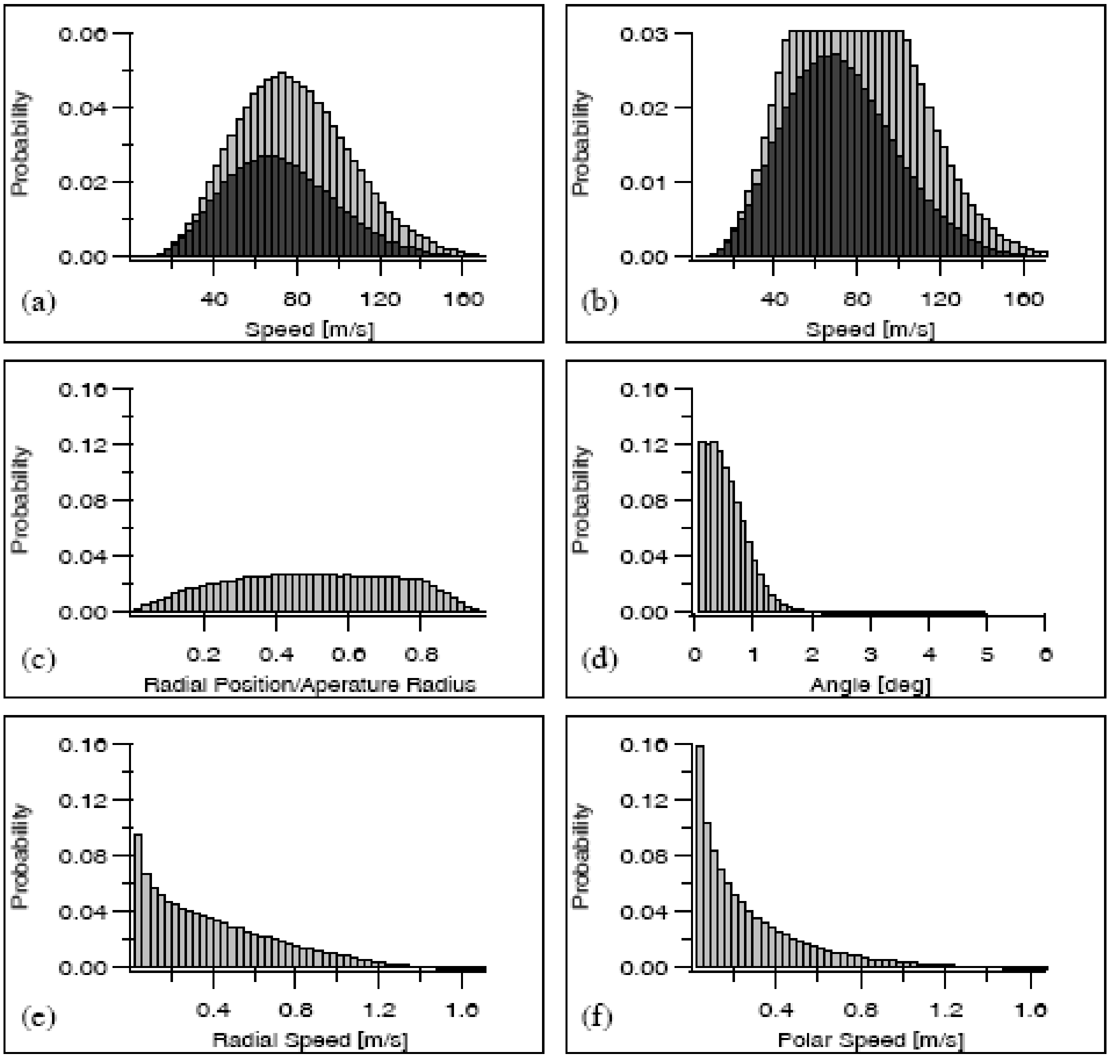

FIGURE 3.4: Results of a simulation with a straight polarizer and no obstructions for atoms with spin in the right state. The light gray bars in (a) represent the velocity distribution of atoms which enter the aperture of the polarizer and the dark gray represents the subset that successfully passes the polarizer. Panel (b) shows the same results as (a) with a different vertical scale. Panels (c), (d), (e) and (f) show the exit distributions with respect to radial position, angle, radial speed and polar speed, respectively, for atoms which successfully pass the polarizer. Totally 160000 atoms are simulated to generate this histogram.

the collection volume, and a short tube can also increase the heat radiation into the collection volume coming from the ABS exit which is at room temperature.

This part of the simulation keeps track of the atoms that can reach the collection volume. The transport tube is simplified to a cylindrical tube for the purpose of simulation. Position and velocity distribution of ^{3}He atoms calculated from the first part of the simulation is used to reproduce how ^{3}He atoms enter the transport tube. As the transport tube is pumped to a high vacuum, the collisions between ^{3}He and ^{4}He molecules are ignored. The collisions among ^{3}He atoms themselves are also ignored because the flux of the beam is low at 10^{14} atoms/s. By ignoring all the collisions, the atoms travel ballistically inside the tube. If an atom hits the wall of the tube, it will have a high probability to stick onto the wall and never enter the collection volume. With 10000 trials, the statistical uncertainly is 1% and the simulation result shows that 89.1% of the 99.8% polarized atoms can enter the collection volume if the length and diameter of the transport tube are 1.9 m and 54 mm, respectively.

The program also keeps a record of all the atoms that succeessfully enter the collection volume. Only these atoms are used to compute the polarization of ^{3}He in the collection volume, and the details of the polarization calculation are shown in the next section.

3.1.3 Spin Precession Simulation

The polarization of ^{3}He atoms in the collection volume is estimated by simulating the ^{3}He spin precession during the injection process. The dynamics of the spin precession under magnetic fields is described by the Bloch equation

$$\frac{d\vec{M}(t)}{dt} = \gamma\vec{M}(t) \times \vec{B}(\vec{r}), \tag{3.6}$$

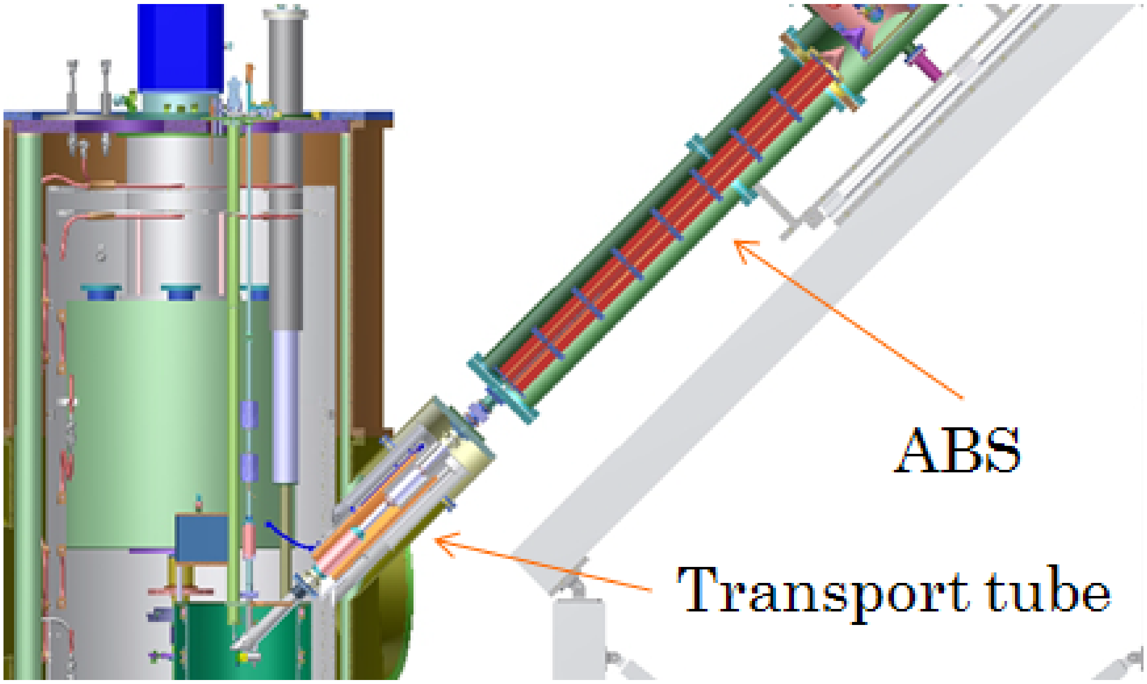

Figure 3.5: ABS (green) connected to the transport tube (silver) at a 45 degree angle. The transport tube and the collection volume are cooled by the dilution refrigerator which is the huge cylinder on the left. The transport magnets and μ metal shielding are not shown in this diagram.

where $\vec{M}$ is the magnetization of each ^{3}He spin, γ is the ^{3}He gyromagnetic ratio, and $\vec{r}$ is the position vector of the ^{3}He atom inside the transport tube. As the field from the ABS to the collection volume is not uniform, ^{3}He spin will see changing fields when it travels through the transport tube. The transport field was designed and calculated by Septimiu Balascuta from Arizona State University using finite element analysis (FEA). FEA discretize the space into 3 dimensional grids. It computes the magnetic field at each grid point given the current distribution. When ^{3}He atoms travel through the tube, it can be imagined as moving inside the 3D grid. The magnetic field must be known continuously at all positions so that Eq. (3.6) can be used to simulate the spin precession. In order to overcome the drawback of the discrete field generated by FEA, the actual field used in Eq. (3.6) is obtained from 3D linear interpolation of the field on the grid. This 3D linear interpolation method requires that the step size of the grid in each direction be fixed. Any position in space is therefore enclosed by a rectangular box. Each vertex of the box is uniquely

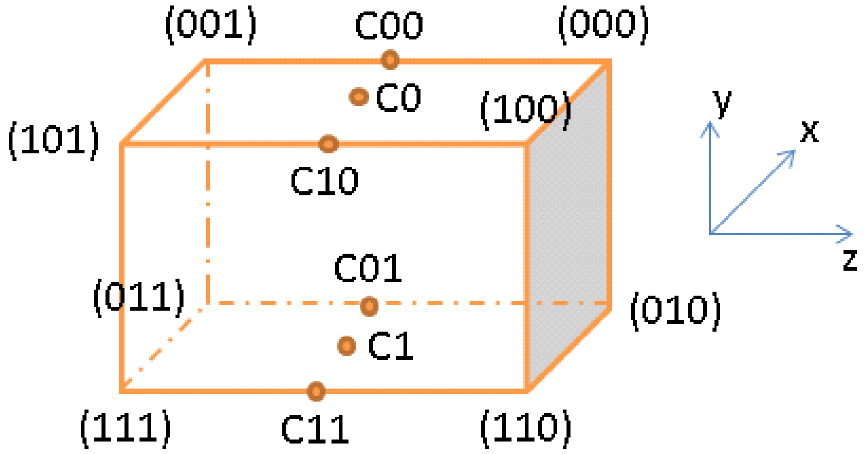

FIGURE 3.6: A diagram showing how the 3D interpolation is done. Field values are known at each of the eight vertices. Every vertex is labeled uniquely for the convenience of showing how the interpolation is done. C0, C1, C00, C01, ..., and C11 are intermediate points used in the 3D interpolation.

labeled, as shown in Figure 3.6. We only know the field at these vertices. For the field at position (x,y,z) other than those vertices, one can interpolate the field as following

$$C_{11} = \frac{z_1 - z}{z_1 - z_0} C_{111} + \frac{z - z_0}{z_1 - z_0} C_{110} \tag{3.7}$$

$$C_{01} = \frac{z_1 - z}{z_1 - z_0} C_{011} + \frac{z - z_0}{z_1 - z_0} C_{010} \tag{3.8}$$

$$C_{10} = \frac{z_1 - z}{z_1 - z_0} C_{101} + \frac{z - z_0}{z_1 - z_0} C_{100} \tag{3.9}$$

$$C_{00} = \frac{z_1 - z}{z_1 - z_0} C_{001} + \frac{z - z_0}{z_1 - z_0} C_{000} \tag{3.10}$$

where C_{ijk} is the magnetic field value at the vertex labeled in Figure 3.6, z_0 and z_1 are the corresponding z coordinates for these vertices. C_{11}, C_{01}, C_{10} and C_{00} are the values of the fields at these points shown in Figure 3.6. Once they are obtained, one can proceed to calculate C_1 and C_0 as following

$$C_1 = \frac{x_1 - x}{x_1 - x_0} C_{11} + \frac{x - x_0}{x_1 - x_0} C_{01} \tag{3.11}$$

$$C_0 = \frac{x_1 - x}{x_1 - x_0} C_{10} + \frac{x - x_0}{x_1 - x_0} C_{00} \tag{3.12}$$

where x_0 and x_1 are the corresponding x coordinates of these vertices. Finally, one obtains the field value at position (x, y, z) through

$$B(x, y, z) = \frac{y_1 - y}{y_1 - y_0} C_1 + \frac{y - y_0}{y_1 - y_0} C_0, \tag{3.13}$$

where y_0 and y_1 are the corresponding y coordinates of these 8 vertices. If the atom moves out of the box, the program will automatically locate the next nearest box containing the atom, and the field values and coordinates of the new vertices will be updated.

Given the field at any position, the next step is to numerically compute $\vec{M}$ for each ^{3}He atom along its path from the ABS to the collection volume. To ensure a high precision of the calculation, the 4th order Runge-Kutta method is used [111]. The general recipe of the Runge-Kutta method is expressed as

$$y' = f(t, y) \tag{3.14}$$

$$y_{n+1} = y_n + \frac{1}{6} h(k_1 + 2k_2 + 2k_3 + k_4) \tag{3.15}$$

$$t_{n+1} = t_n + \Delta t \tag{3.16}$$

where y change as a function of time t, and k_1, k_2, k_3 and k_4 are respectively equal to

$$k_1 = f(t_n, y_n) \tag{3.17}$$

$$k_2 = f(t_n + \frac{1}{2}\Delta t, y_n + \frac{1}{2}\Delta t k_1) \tag{3.18}$$

$$k_3 = f(t_n + \frac{1}{2}\Delta t, y_n + \frac{1}{2}\Delta t k_2) \tag{3.19}$$

$$k_4 = f(t_n + \frac{1}{2}\Delta t, y_n + \frac{1}{2}\Delta t k_3) \tag{3.20}$$

To use this recipe, we let $y = \vec{M}(t)$ and $f = \gamma \vec{M} \times \vec{B}$, and calculate $\vec{M}(t)$ in the vector form. As the length of $\vec{M}$ will not change during the precession, $\vec{M}$ is normalized to 1 at each integration step to reduce rounding error. In order to control the accumulated error under 1%, it is found that the time step size needs to be at least

$$\Delta t = \frac{10^{-8}}{B} \text{ [s/G]}, \tag{3.21}$$

where B is the magnitude of the magnetic field strength in Gauss. As the magnetic field is changing from one place to another, the step size Δt is also changing during the integration. In this way, the precision of the integration is guaranteed and unnecessarily small step sizes are avoided at locations with small field values.

The polarization of spins is defined as the average of $\vec{B} \cdot \vec{M}/(BM)$. With the latest transport magnetic field design, the simulation yields a polarization of 76% for the positive current and 79% for the negative current, as shown in Figure 3.7. The positive and negative current represent the field generated by the 24 turns cosθ coil is in the positive and negative $\hat{x}$ direction, respectively.

In order to identify the regions where ^{3}He loses the polarization during the injection, we plot the polarization as a function of position as shown in Figure 3.8. As seen in this plot, two regions with major polarization loss are identified. One is close to 180 cm where the ABS is located and the other is the big slope where the atoms

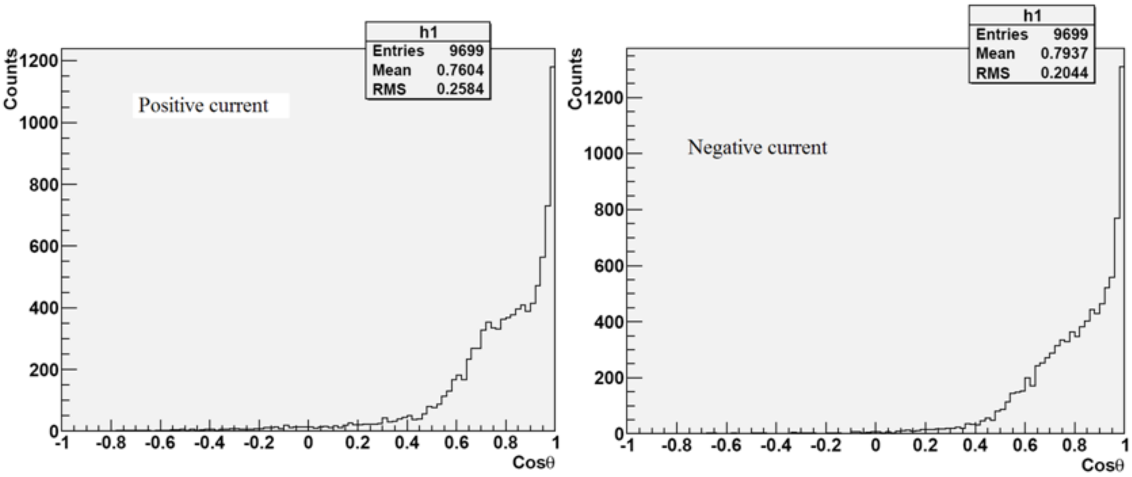

FIGURE 3.7: Angle distribution of ^{3}He spins in the collection volume. The left panel is for the positive current and the right panel is for the negative current. The mean at the top right corner gives the average of the $\cos\theta$ where θ is the angle between $\vec{B}$ and $\vec{M}$, which is essentially the polarization. Totally 9699 atoms are simulated to generate these two histograms.

start to enter the collection volume. The reason for the first polarization drop is due to the irregular stray fields from the quadruple magnets in the ABS. The second drop is due to the 45 degree rotation of the field from the axial direction to the horizontal direction. The first drop can be eliminated by increasing the transport magnetic field strength at the ABS exit. We artificially double the transport field strength at the ABS exit and the polarization loss is reduced from 10% to 3%. The second drop can be minimized if we let the spin rotation happen at the high field region, i.e. close to the ABS end, since it is easier for spin to follow a high field than a low field.

In order to achieve the 95% polarization at the collection volume required by the nEDM experiment, the transport magnetic field needs to be redesigned. Currently, the field design and calculation are transferred from Septimiu Balascuta to Christopher Crawford at University of Kentucky. Collaboration work with Chris Crawford in doing the spin transport simulation will help finalize the transport coil design.

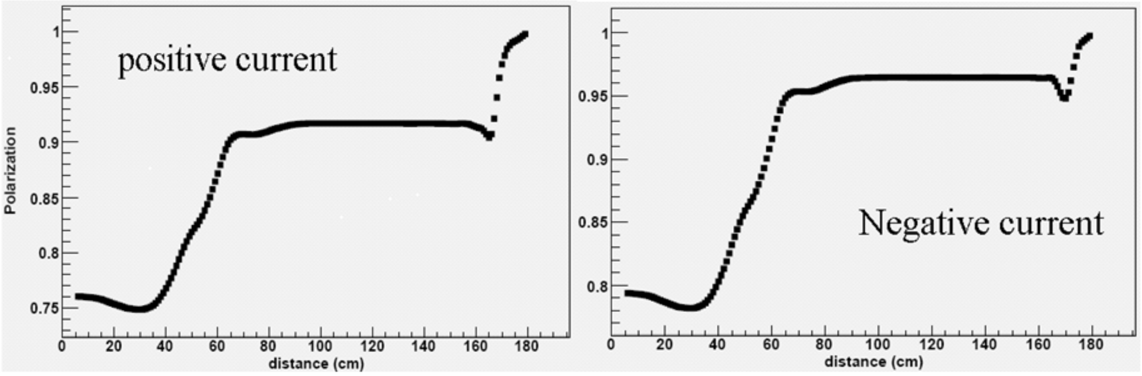

FIGURE 3.8: The polarization as a function of distance measured from the collection volume. ^{3}He atoms travel from right to the left with an initial polarization of $\sim 100\%$, so 180 cm is the exit of the ABS and 0 cm is the center of the collection volume.

3.2 SQUID Implementation for the Monitoring of ^{3}He Polarization in the Collection Volume

SQUID is one of the most sensitive devices available to measure a magnetic flux. The typical noise level of a SQUID magnetometer is 1 fT/$\sqrt{\text{Hz}}$. This extremely low noise figure makes SQUID suitable to many applications that are impossible using traditional NMR methods (usually a factor of 10^4 to 10^6 difference). One example is to measure a magnetic field generated from organs inside human bodies such as the heart (10^{-10} T) or the brain (10^{-13} T). In our experiment, the magnetic field from ^{3}He atoms is extremely small because of the small number density (10^{14} atoms/cc) of ^{3}He. In addition, the resonance frequency is only a few hundred Hz which makes the traditional magnetic resonance technique completely unpractical.

The key part of a SQUID sensor consists of a superconducting ring with one or two Josephson junctions [77]. The Josephson junction is made of two superconductors separated by one thin insulation layer (SIS). The insulation layer is thin enough so that the cooper pairs in the superconductor have enough probability to tunnel through the insulator and reach the superconductor on the other side. Hence, it combines two quantum mechanical phenomena. One is the quantization of magnetic flux in the superconducting ring; the other is the tunneling effect. In the next section, an introduction to the working principle of the SQUID sensor will be presented.

3.2.1 Basic Concepts of a SQUID Magnetometer

In a superconductor, the supercurrent is carried by cooper pairs. A cooper pair is made of two electrons. These two electrons always move together with double mass and double charge of a single electron, so they can be treated as a single particle. Since the cooper pair does not have lattice scattering in the superconductor, it has a very long coherence length, which can be represented by a wave function [120]

$$\phi_p = \phi_0 \exp(i\vec{p}\cdot\vec{r}/\hbar), \tag{3.22}$$

where $\vec{p}$ is the momentum of the cooper pair, $\vec{r}$ is the distance and $\hbar$ is the Planck's constant. Because the cooper pair is coherent over a long distance, there is a definite phase difference between any two positions X_a and X_b if they are on the path of the supercurrent flow. This difference can be expressed as

$$(\Delta\phi)_{XY} = \phi_Y - \phi_X = 2\pi \int_X^Y \frac{\hat{x}}{\lambda}\cdot d\vec{l}, \tag{3.23}$$

where $\hat{x}$ is the unit wave vector denoting the direction of the wave and λ is the wave length of the cooper pair. If an external magnetic field is applied to the system, the momentum $\vec{p}$ is modified to $\vec{p} = m\vec{v} + q\vec{A}$, where $\vec{A}$ is the vector potential of the applied magnetic field and q is 2e, the charge of cooper pairs. Due to this additional term in $\vec{p}$, the wavelength is changed by

$$\Delta\lambda = \frac{h}{q\left|\vec{A}\right|} = \frac{h}{2e\left|\vec{A}\right|}. \tag{3.24}$$

Therefore, an additional phase difference due to the $\vec{B}$ field is added to the two positions

$$[(\Delta\phi)_{XY}]_B = \frac{4\pi e}{h}\int_X^Y \vec{A}\cdot d\vec{l}. \tag{3.25}$$

The long coherence of the cooper pair allows one to choose a closed path in the superconductor and integrate Eq. (3.25) over this closed loop. Since the wave function is a single-valued function, every point along the loop must have a definite amplitude and phase. This requires that the integral Eq. (3.25) over a closed loop must be equal to a multiple of 2π. As a result, the wave function exactly repeats itself when the integration comes back to its starting point. This condition is also known as magnetic flux quantization in the superconductor, since the integral

$$\oint \vec{A} \cdot d\vec{l} = \int\int \vec{B} \cdot d\vec{S}, \tag{3.26}$$

which is the flux passing through the closed path. Substitute this into Eq. (3.25), one obtains

$$\Delta\phi_B = \frac{4\pi e}{h} \int\int \vec{B} \cdot d\vec{S} = 2n\pi, \tag{3.27}$$

where n is a positive integer. If we use φ to represent the magnetic flux, then Eq. (3.27) can be rewritten as $\varphi = n\varphi_0$, where $\varphi_0 = \frac{h}{2e} = 2.07 \times 10^{15}$ Wb is one flux quanta. Strictly speaking, it is not necessary to have a complete superconducting ring. As long as some non-superconducting area is enclosed by a superconducting material, the magnetic flux trapped in the superconducting material will be quantized. If the insulation barrier (I) sandwiched between two superconducting materials (S) is thin enough, the cooper pair can easily tunnel through the barrier. In this case, the two superconductors are weakly coupled and this junction (SIS) is called Josephson junction. Like the normal superconductor, the Josephson junction also has its critical current I_c [77], above which its superconductivity will be destroyed. However, the difference is that the critical current in the Josephson junction is usually much smaller than that of a pure superconductor. If there is a phase difference ϕ_I between the weakly coupled superconductors, the intensity of the current flowing across the insulator I_s is related to the critical current I_c by

$$I_s = I_c \sin(\phi_I). \tag{3.28}$$

A dc SQUID consists of a superconducting ring with two Josephson junctions. When a magnetic field is applied to the superconducting ring, an induced current I_s will be generated in the ring to partially compensate for the applied flux. If φ_a is the flux from the applied magnetic field, the phase change from the applied magnetic field is $\phi_B = 2\pi\frac{\varphi_a}{\varphi_0}$. The quantization condition can still be satisfied by developing a phase difference across the weak link. If we denote this phase difference as ϕ_I, and assume that the two Josephson junctions are identical to each other in the dc SQUID, the total phase change can be expressed as $\Delta\phi = \phi_B + 2\phi_I = 2n\pi$. Substituting ϕ_I into Eq. (3.28), the induced current is therefore obtained

$$I_s = I_c \sin(\pi\frac{\varphi_a}{\varphi_0}) \tag{3.29}$$

Theoretically, by detecting this induced current I_s, one can deduce how much flux is applied to the SQUID sensor. As current can be determined to a high precision, the dc SQUID sensor further improves the sensitivity by measuring the flux down to a fractional number of one flux quanta.

3.2.2 The Practical Way to Measure Magnetic Field Using dc SQUID

Eq. (3.29) is a periodic function with a period of $2\varphi_0$. This makes it difficult to measure a magnetic flux bigger than $2\varphi_0$, because different magnetic flux can have the same induced current. To overcome this drawback, a dc SQUID usually works in a flux-locked mode to linearize the SQUID response to a flux change [40]. In this configuration, a solenoid coil, connected to the feedback circuit, is coupled to the SQUID loop. When a flux change presents to the SQUID loop, the induced current will be amplified and lock-in detected. This signal is then fed back to the the SQUID loop via the solenoid coil. The flux generated from the solenoid coil is applied to the SQUID loop in such a way that it perfectly cancels out the flux presented to the SQUID loop from outside. Hence, the net flux inside the SQUID loop is always a constant and the magnitude of the external flux is proportional to the current or voltage in the feedback circuit, Figure 3.9.

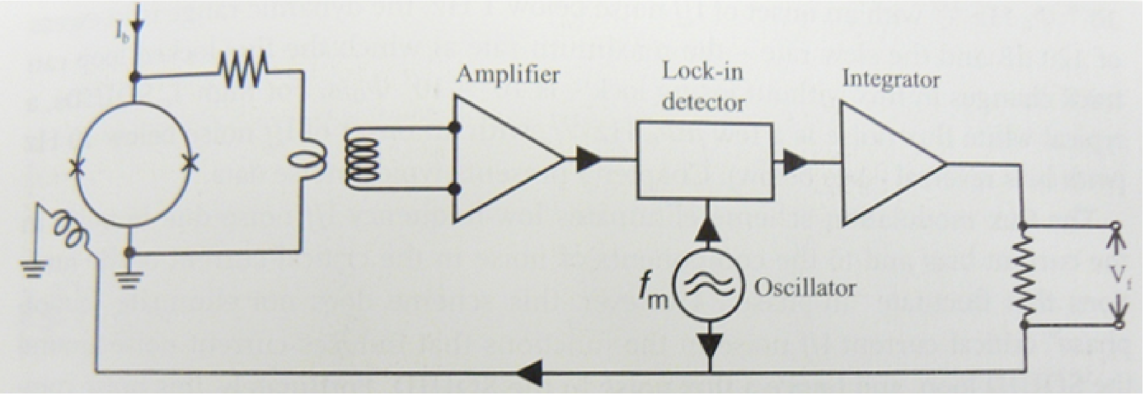

FIGURE 3.9: The SQUID loop (the two Josephson junctions are shown as two crosses) is coupled to the solenoid coil that connects to the feedback circuit. The induced current in the SQUID loop is amplified and lock-in detected. It is then fed back to the solenoid to cancel the flux from the applied magnetic field. The magnitude of the measured flux is therefore proportional to the voltage V_i on the resistor.

In practice, the SQUID loop is not used directly to measure the magnetic flux because of the inconvenience and delicacy of the SQUID loop. Instead, the most common way is to have a dedicated superconducting pickup coil to measure the magnetic flux. The pickup coil can vary in size and in configurations, such as a gradiometer. In this way, people have more freedom in terms of coil design so that it fits into their applications better. The pickup coil is coupled to the SQUID loop through a solenoid coil, similar to the feedback circuit. If one measures flux Φ at the pickup coil, the induced current I in the pickup coil can be expressed as

$$\Phi = B \times A = (L_i + L_p) \times I, \tag{3.30}$$

where B is the magnetic field at the pickup coil, A is the area of the pickup coil,

L_i is the inductance of the input solenoid coil coupled to the SQUID loop and L_p is the inductance of the pickup coil, including the inductance from the wire itself. The induced current will generate a flux at the SQUID loop through the coupling solenoid. The flux seen by the SQUID coil is

$$\Phi_{SQUID} = M \times I, \tag{3.31}$$

where M is the mutual inductance between the SQUID loop and the solenoid. From Eq. (3.30) and Eq. (3.31), one can obtain the efficiency of flux transfer between the pickup coil and SQUID loop,

$$\frac{\Phi_{SQUID}}{B} = \frac{M \times A}{L_p + L_i}. \tag{3.32}$$

It can be seen from Eq. (3.32) that a larger area A of the pickup coil and a better coupling (M) between SQUID loop and pickup coil will generate more flux at the SQUID loop given the same magnetic field. The inductance of the pickup coil can be calculated from an empirical function [40]

$$L_p(N) = F \cdot D[cm] \cdot N^2[nH], \tag{3.33}$$

where N is the number of turns, D is the diameter of the pickup coil, and $F = 5.87 - 14.25Log(l/D)$. In this formula, l is the width of the coil winding. It can be computed as $l = (N-1)p + d$, where p is the pitch of the winding and d is the thickness of the wire. For the estimation of the inductance of the wire, a typical value to use is 0.5 nH/mm [40].

The pickup coil used in our experiment is a one-turn gradiometer, Figure 3.10(c). The gradiometer has two identical loops connected in series but with opposite winding directions. The spatial separation between two loops in our gradiometer is 1.25 cm. The diameter of the coil is 1.25 cm and the thickness of the wire is 0.29 mm. Using Eq. (3.33) and 10 cm as the length of the wire, $L_p = 36 + 50 = 85$ nH. The

SQUID package we used is manufactured by StarCryo Electronics and the type of the SQUID is called SQ680. The inductance L_i of the input solenoid coil is 683 nH and the mutual inductance M is 10 nH. Using these numbers and Eq. (3.32), the efficiency of the SQUID is 1.3 nT/φ_0. Given the typical value of the SQUID intrinsic noise 5 $\mu\varphi_0/\sqrt{\text{Hz}}$, the sensitivity of our SQUID sensor is 6.5 fT/$\sqrt{\text{Hz}}$. In practice, besides the intrinsic noise, there are other types of noise, such as magnetic noise, RF noise, vibrational noise, etc. The sensitivity of the SQUID could be worse than the ideal value. However, with a complicated shielding and vibration reduction, it is possible to reduce the noise to the intrinsic level and reach the ideal sensitivity.

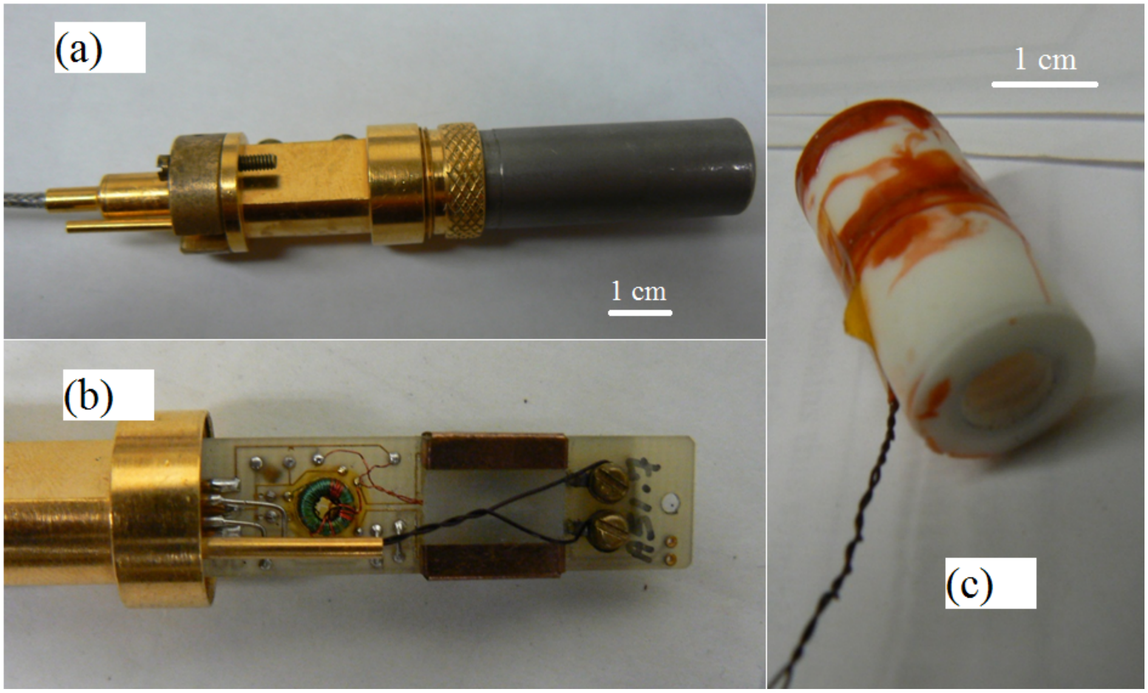

Figure 3.10: Panel (a) shows the entire SQUID assembly with the Niobium shielding (gray cylinder). Panel (b) shows the inside of the SQUID with the Niobium shielding removed. The SQUID loop is under the white square plastic. The braided wires under two brass screws connect the pickup coil and the input solenoid coil. They come out of the SQUID package through a needle-like feedthrough. Panel (c) shows the gradiometer used in the experiment. The Brown color is the glue used to fix the wires into the grove of the ceramic holder.

SQUID gives absolute flux measurement. A parameter, called transfer function, allows one to convert the measured voltage to the flux experienced by the SQUID loop. As the transfer function only depends on the feedback circuits and the coupling between the SQUID loop and the feedback loop, it is nearly a constant over the lifetime of a SQUID. In the SQUID operation manual, there is a standard procedure to measure the transfer function. A typical value is about $\approx 1\ \mathrm{V}/\varphi_0$. From the transfer function and Eq. (3.32), one can establish a relationship between the measured voltage and the magnetic field received by the pickup coil.

3.2.3 Experimental Apparatus and Procedures

The SQUID experiment is carried out at 4.2 K using a dewar filled with liquid ^{4}He. This temperature is different from the temperature of the actual nEDM experiment; however the comparison between the two is still valid for two reasons. Firstly, the signal size of the ^{3}He seen by SQUID is independent of the temperature. Secondly, in our experimental conditions, the major noise source in the SQUID is the environmental noise and this noise is independent of temperature. A key advantage is that the turn-around time at 4.2 K is much shorter than at a lower temperature using a dilution refrigerator. This expedites the experiment tremendously.

Polarized ^{3}He is prepared using spin exchange optical pumping (SEOP) technique. The ^{3}He gas is mixed with Rb vapor and stored in a pyrex glass cell, Figure 3.11b. The unpaired electron in the outermost shell of the Rb is polarized by absorbing the angular momentum from the circularly polarized laser. The polarized Rb atom then exchanges its spin with the nucleus of the ^{3}He atom through the hyperfine interaction. As a result, ^{3}He atoms are polarized by the optically polarized Rb vapor. Using this technique, we obtain approximately 30% polarization of ^{3}He in the pyrex cell.

Once the ^{3}He cell is polarized, it is mounted on a glass manifold that connects to the measurement cell inside the dewar at 4.2 K, Figure 3.11(a). The measurement cell is of cylindrical shape with an inner diameter of 8 mm and a length of 25 mm.

The inner surface of the measurement cell is coated with Cesium metal to increase the relaxation time (T_1) of polarized ^{3}He. The glass manifold is also connected to a turbo pump so that everything inside the manifold, including the measurement cell, is under vacuum. Everytime the ^{3}He cell is mounted on the glass manifold, a part of the glass manifold will be exposed to air. Hence, we pump the glass manifold for at least 15 minutes until the vacuum of the glass manifold and the measurement cell is below 3×10^{-8} Torr. Once the vacuum is ready, we open the valve on the manifold and let ^{3}He diffuse into the measurement cell. This process usually takes about 5 seconds. After the measurement cell and ^{3}He cell reach equilibrium, we start the polarization measurement on the measurement cell. After the measurement, we pump out the ^{3}He gas inside the measurement cell and restart the measurement procedure.

We use the pulsed nuclear magnetic resonance (pNMR) technique, also known as free induction decay (FID), to measure the polarization of polarized ^{3}He in the measurement cell. A radio frequency (RF) pulse was applied to the ^{3}He sample through a RF coil. If the frequency of the pulse equals the ^{3}He precession frequency $f = \gamma_{^3\mathrm{He}} B_0$, where $\gamma_{^3\mathrm{He}}$ is the gyromagnetic ratio of ^{3}He spin and B_0 is the magnetic holding field, it can tip the ^{3}He spin away from the holding field direction. Consequently, the ^{3}He spin starts to precess around the magnetic holding field. The magnetic flux generated from the precessing spin is received by the pickup coil of the SQUID mounted on the side of the measurement cell. With the same polarization and number density of the ^{3}He spins, the magnitude of the flux generated at the pickup coil is proportional to $\sin\alpha$, where α is the tipping angle between the spin and the holding field. The angle is controlled by the duration and amplitude of the RF pulse. It is usually chosen between 5 and 15 degrees since pNMR is a destructive measurement and the polarization loss is proportional to $1 - \cos\alpha$.

The timing of the pNMR measurement is crucial. In our experiment, this is

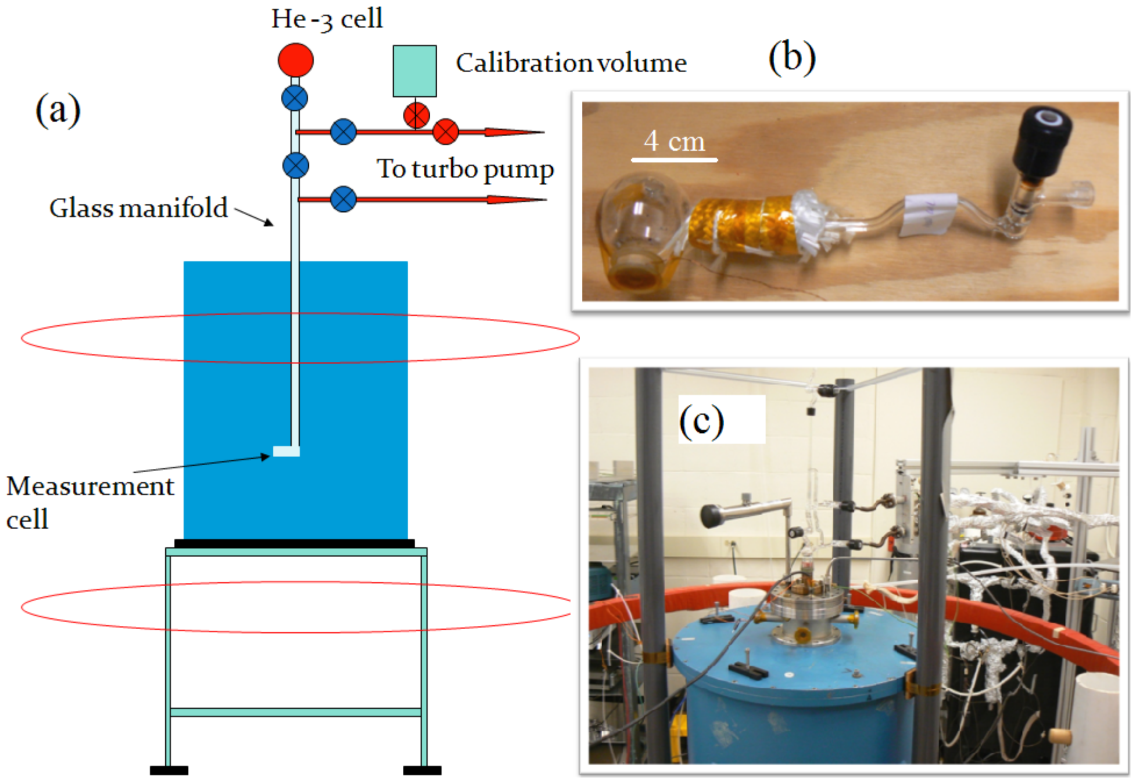

FIGURE 3.11: Schematic of the experiment (SQUID sensor is not shown) (a). The ^{3}He cell is on the top of the glass manifold and a photo of the cell is shown in panel (b). Panel (c) shows the blue dewar, pumping lines (on the back), glass manifold on top of the dewar and part of the red Helmholtz coils.

controlled by a pulse delay generator which has a time accuracy of 1 ns. The pulse generator will first send a TTL signal to trigger the function generator to send a RF pulse to the ^{3}He sample. During the meantime, it sends a blank signal to reset the SQUID so that the SQUID stops functioning during the RF pulse. After the RF pulse, the SQUID blank signal is off and a third signal is sent to computer to start data acquisition (DAQ). A diagram that demonstrates the connection and timing is shown in Figure 3.12.

As the SQUID is extremely sensitive, the noise reduction is crucial for the SQUID to work properly. Many techniques have been developed to reduce the noise. In a typical SQUID application, one layer of RF noise shielding and three layers of

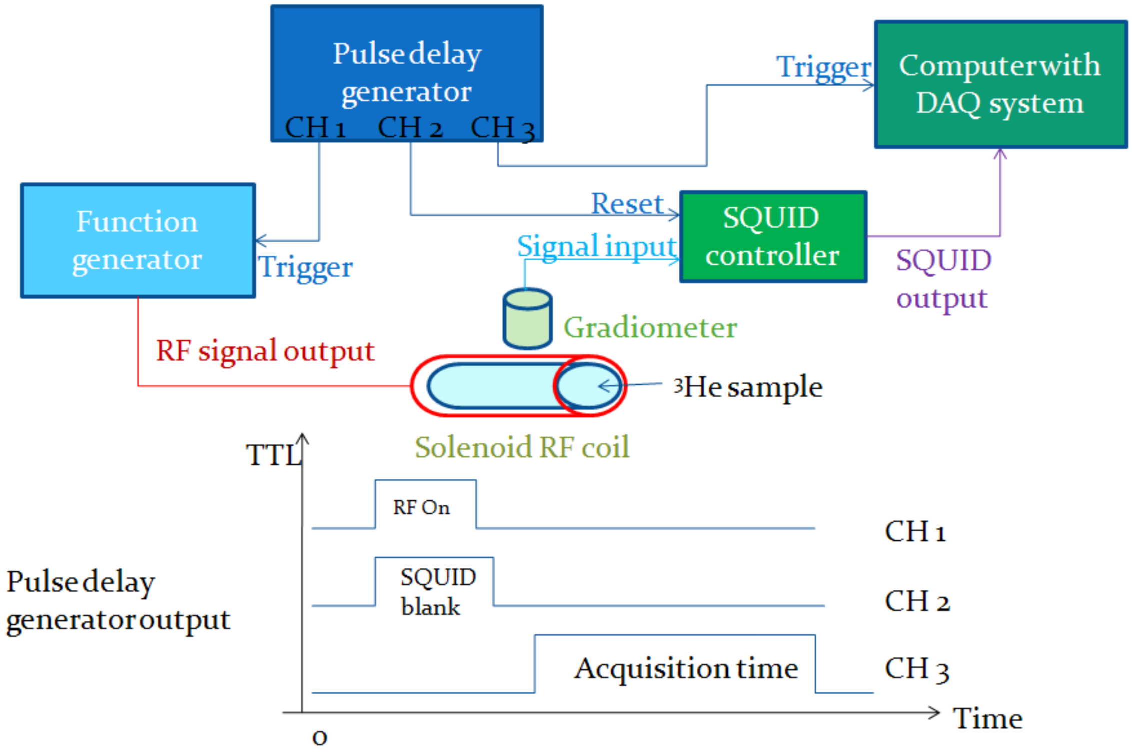

FIGURE 3.12: pNMR technique using the SQUID sensor (top). The signal output from the pulse delay generator used to control and synchronize the function generator, SQUID and the DAQ system (bottom).

magnetic shielding are required to reduce the environmental noise below the SQUID intrinsic noise level. People also use a superconducting can to shield the noise. As the field inside the superconducting can decays exponentially, one or two layers of the shielding are more than enough. However, the drawback of the superconducting shielding and magnetic shielding is that any external magnetic field applied to the system must be inside the shielding. In our experiment, the Helmholtz coil is outside the dewar, so any of these shielding cannot be used.

Alternatively, the shielding technique we use is the dewar itself because it has four heat insulation layers made of aluminum. When all the layers are grounded to the same reference point, it can effectively shield the noise above 10 kHz. As the skin depth of the low frequency noise becomes too large, the Al shielding does not shield low frequency noise effectively. In order to shield the low frequency noise, an open-ended superconducting tube is placed around the SQUID pickup coil and the measurement cell, Figure 3.13. In contrary to the superconducting can, the superconducting tube only shields the flux in the transverse direction, but not the flux in the axial direction. This allows the vertical magnetic holding field to penetrate into the shielding but reject noise from other directions. The long superconducting tube also increases the uniformity of the holding field, which improves T_2 and acquisition time of the ^{3}He signal.

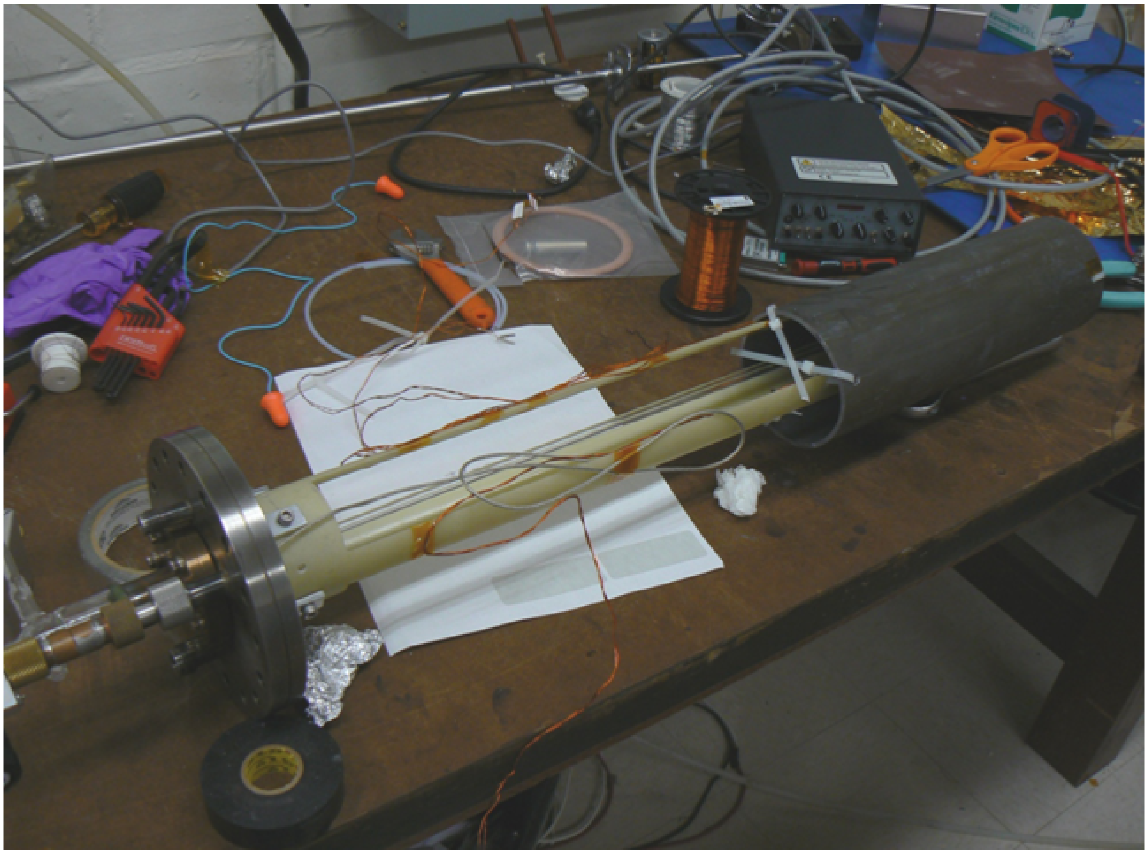

Figure 3.13: A lead superconducting tube (gray tube on the right) around the measurement cell. The measurement cell and the SQUID are hidden inside the tube and mounted on the yellow G-10 support.

Besides shielding, the pickup coil of the SQUID is also in a gradiometer configuration so that the uniform background noise is rejected. Moreover, we wrap two layers of gold foil around the pickup coil to further suppress the noise. The vibration induced noise, such as ^{4}He boiling off, is suppressed by mounting everything onto the sturdy G-10 support (yellow part in Figure 3.13). The lead tube shielding also adds stability to the system because of its weight.

3.2.4 Experimental Results

We measure the transfer function of the StarCryo Model 680 SQUID every time we cool down the SQUID sensor. The measurements consistently give a value of 0.73 $\mathrm{V_{pp}}/\varphi_0$. The background noise spectrum of the SQUID is measured by the SR760 FFT spectrum analyzer manufactured by Stanford Research System. Using the transfer function, we can convert the noise into the unit of flux quanta φ_0. The result is shown in Figure 3.14. The pNMR measurement is carried out at 1 kHz, corresponding to a field of 300 mG. The noise level at 1 kHz from the spectrum reads 10 $\mu\varphi_0/\sqrt{\mathrm{Hz}}$, which is twice as large as the intrinsic noise level. With limited shielding in our experiment, this noise level is considered to be very low.

A typical pNMR measurement is shown in Figure 3.15. In the fast diffusion limit, the signal $V(t)$ decays exponentially according to the equation $V(t) = V_0 \exp(-t/T_2)$, where $1/T_2$ is the transverse relaxation rate. At 4.2 K, ^{3}He atoms move very slowly, therefore the fast diffusion result is not applicable. In the slow diffusion limit, every atom can be treated as stationary in space, and the decay envelop of the signal is more complicated. One can refer to Chapter 4 for a complete treatment of this relaxation problem.

We also perform a $\mathrm{T_1}$ measurement on the measurement cell. $\mathrm{T_1}$ characterizes how fast the polarization of ^{3}He decays. Many factors contribute to the $\mathrm{T_1}$ relaxation. In our SQUID experiment, $\mathrm{T_1}$ is dominated by the wall relaxation. With the bare pyrex glass, the measured $\mathrm{T_1}$ is around 70 seconds. With Cs coated pyrex glass, $\mathrm{T_1}$ increases to more than 2000 seconds, Figure 3.17. This two orders of magnitude

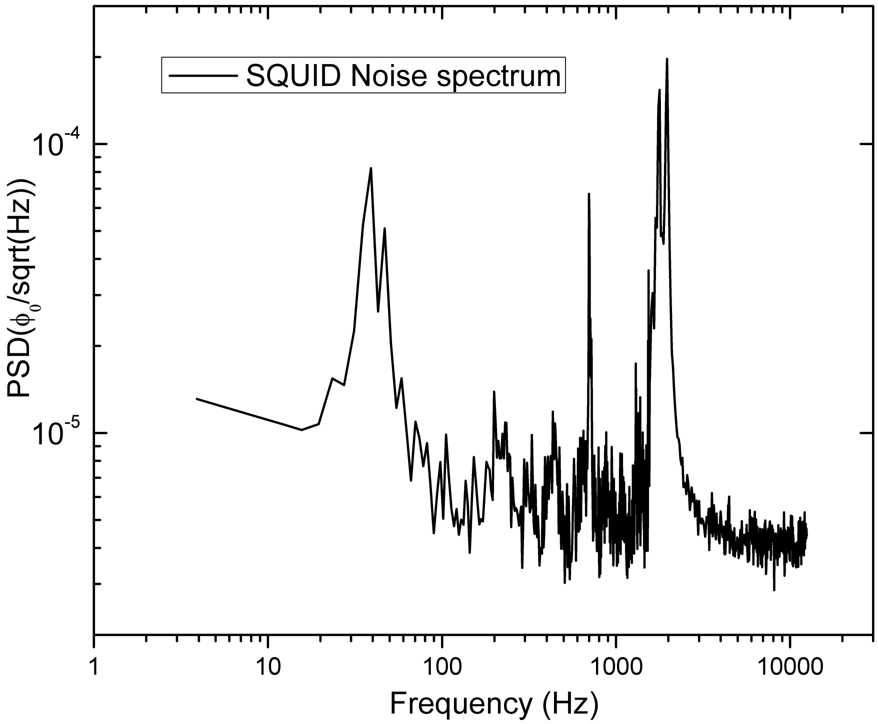

FIGURE 3.14: Noise spectrum of the SQUID from 1 to 10^4 Hz. The vertical axis is the power spectrum density. The pNMR measurement is carried out at 1 kHz.

improvement agrees with the observation in [67]. Since we want to demonstrate that ^{3}He signal with a number density of 5×10^{14} atoms/cc is measurable, we need to dilute the ^{3}He sample. Surprisingly, after the dilution, T_1 is also reduced proportional to the number density of the gas. The extremely short T_1 (less than a few seconds) at diluted number density makes it impossible to perform the pNMR measurement. As a result, instead of actually trying to reach the low number density, we have to deduce the signal size at the density of 5×10^{14} atoms/cc from the current measurement. In addition, we have also carried out a dedicated project to study the pressure/number density dependence on T_1. This is discussed in Chapter 4.

Each data point in Figure 3.17 is determined by the resonance peak height in

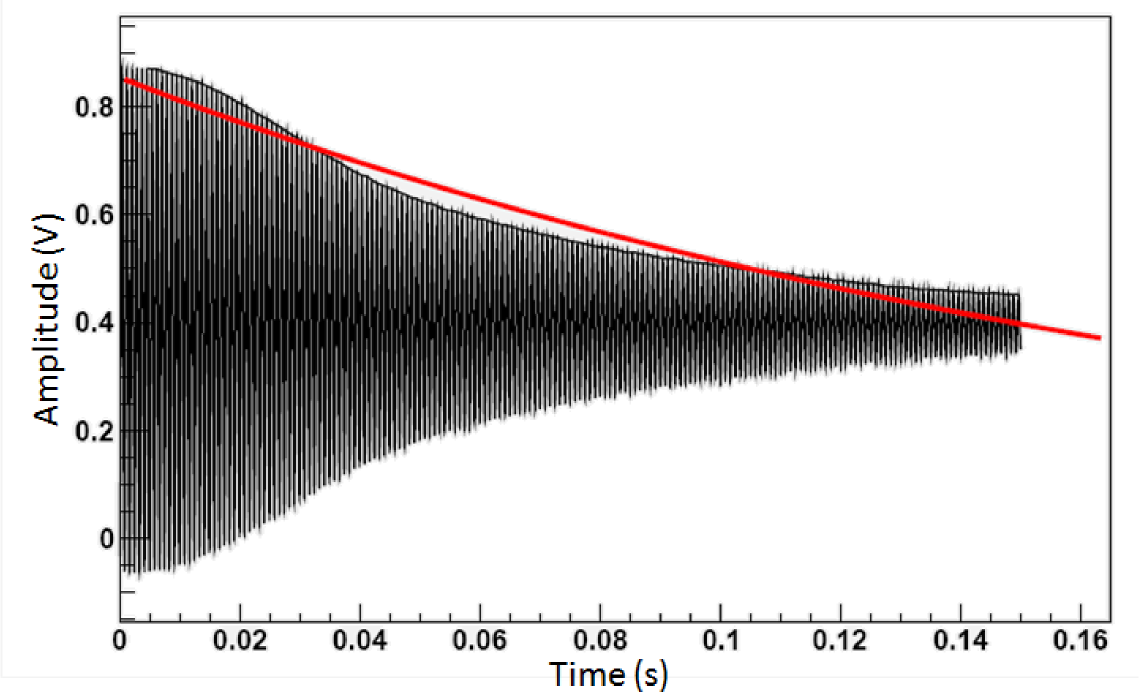

FIGURE 3.15: Typical time domain signal of the pNMR measurement. The acquisition time is 0.15 s. The red curve is the T_2 exponential fit, which does not match well because the signal does not decay exponentially.

the frequency domain, obtained from the Fourier transformation of the time domain signal, Figure 3.16. For the particular T_1 measurement shown in Figure 3.17, the ^{3}He pressure inside the measurement cell is 59 Torr. Using $T = 4.2$ K and assuming ^{3}He gas is an ideal gas, one can obtain the number density of ^{3}He inside the measurement cell to be 1.3×10^{20} atoms/cc. If we use the first data point in the figure as the biggest signal we can measure from 1.3×10^{20} atoms/cc ^{3}He with 30% polarization, and use 4×10^{-5} as the noise background, one obtains the signal to noise ratio SNR $= \frac{0.4}{4\times10^{-5}} = 10^4$. If the ^{3}He number density is reduced to 5×10^{14} atoms/cc with 95% polarization, the SNR will be 0.12.

There are several avenues to further improve the SNR. The acquisition time in the pNMR measurement is only 0.15 s, because the relatively large field gradient decreases the T_2 of the ^{3}He signal. However, the actual nEDM experiment has sev-

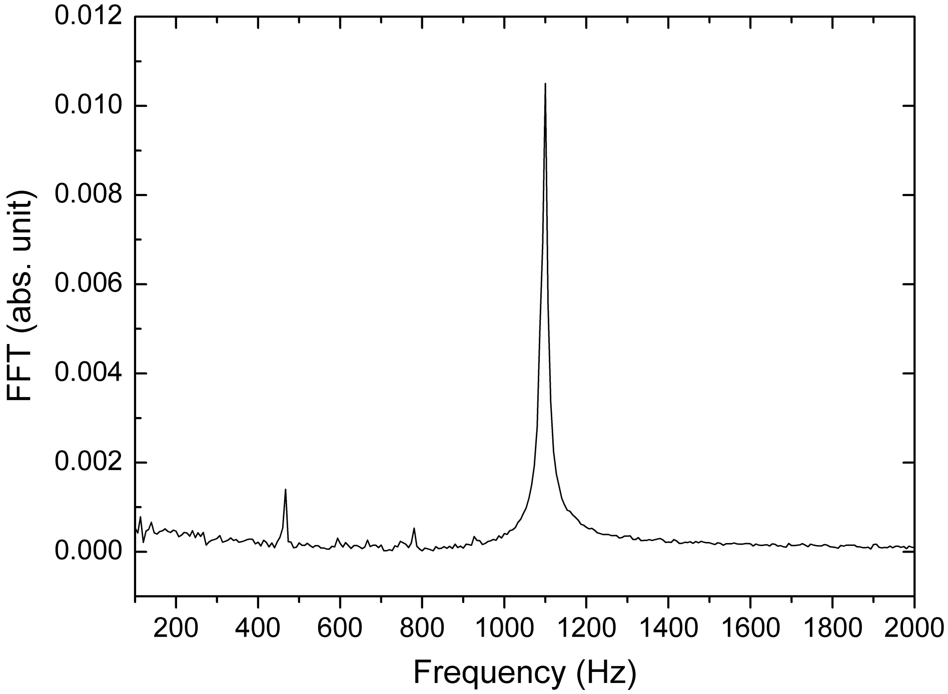

FIGURE 3.16: The fast Fourier transform (FFT) of the time domain signal. The resonance frequency is approximately 1.2 kHz.

eral layers of magnetic shielding and one layer of superconducting shielding. The $\cos\theta$ coil produces a very uniform field at the collection volume. This uniform field helps maintain ^{3}He precession signal for a much longer time. Based on a theoretical calculation, the measurement time in the nEDM experiment should be at least 200 seconds. The basics of the Fourier transform show that the SNR of a measurement is proportional to the square root of the measurement time given that all other parameters remain the same [6]. If taking into account the longer measurement time in the actual nEDM experiment, the projected SNR will be 4.4 rather than 0.12. The better shielding in the nEDM experiment will also reduce the noise background, it is reasonable to assume that the noise in the nEDM experiment will be at the intrinsic noise level $5\mu\varphi_0/\sqrt{\mathrm{Hz}}$ which is half the value of our current background noise. Addi-

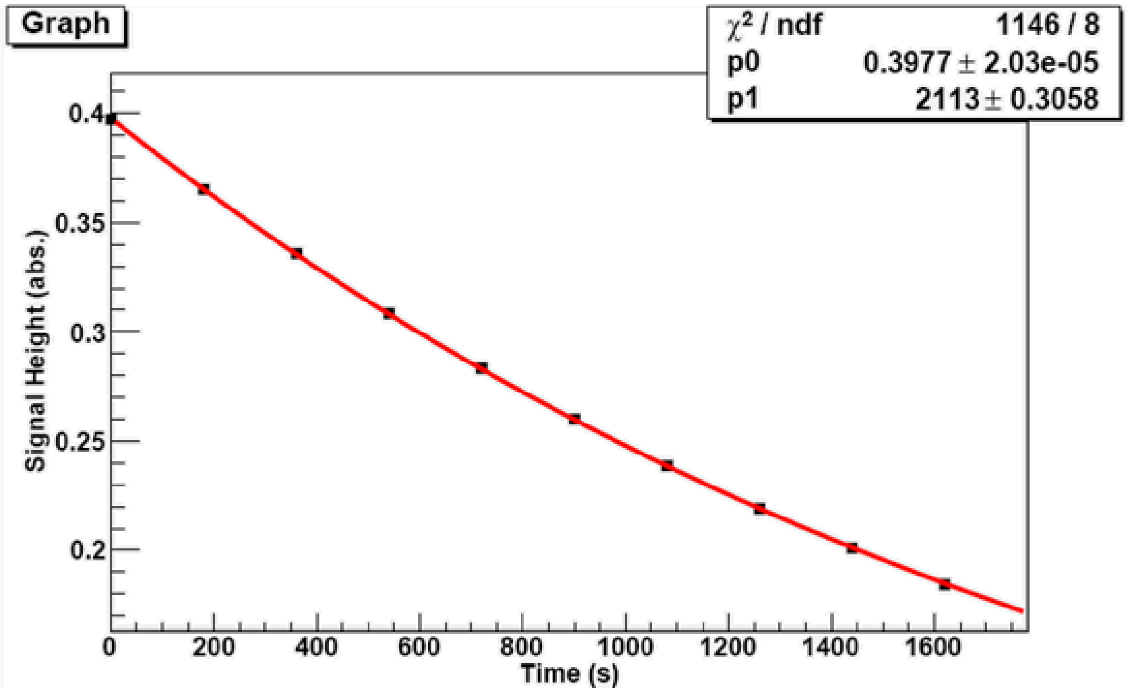

FIGURE 3.17: Longitudinal relaxation time T_1 measurement of ^{3}He in the Cs coated measurement cell. The pressure in the measurement cell is 59 torr, corresponding to 1.3×10^{20} atoms/cc. The exponential fit yields $T_1 = 2113 \pm 0.3$ s.

tionally, the pulse used in our experiment has a tipping angle of 8 degree, resulting in a loss about 1%. However, a 15 degree pulse can be used, which can double the signal size with only 5% polarization loss. In conclusion, taking all these improvements into account, the SNR of the SQUID measurement in the nEDM experiment will be at least 10, which is more than enough to measure the ^{3}He polarization in the collection volume.

4

Relaxation Study of Optically Polarized ^{3}He

In nEDM experiment, ^{3}He is polarized by the quadruple magnet, which achieves 99% polarization. In our laboratary, ^{3}He is polarized by the spin-exchange optical pumping (SEOP see Appendix A), which can achieve a polarization more than 30%. Both of these values far exceed the the polarization in the equilibrium state when placing the ^{3}He in a moderate magnetic field. The polarization of ^{3}He will inevitably drops to the equilibrium value once the the polarizing process is finished. This depolarizing process is characterized by the longitudinal relaxation rate $1/T_1$, which represents how fast the polarization will decress. There are many factors that can contribute to the T_1 depolarization. Among all of them, the most important ones for ^{3}He are the dipole-dipole interaction induced relaxation, wall relaxation, and field-gradient induced relaxation. Dipole-dipole interaction induced relaxation is 744 hours for 1 atm ^{3}He cell,

$$\frac{1}{T_{1\,dd}} = \frac{[^3He]}{744}\ \mathrm{hrs}^{-1}, \tag{4.1}$$

where $[^3He]$ is the number density of ^{3}He in amagats. Since this is extremely long, it can be safely ignored in most cases.

Wall relaxation is due to the collision of ^{3}He atoms with the inner surface of the ^{3}He cell. As the surface may contain some magnetic impurities. The spin of ^{3}He may get flipped when the atom has contact with the magnetic site. There are two kinds of magnetic impurities, paramagnetic impurities and ferromagnetic impurities. The relaxation behaviors are totally different for different impurities. It was believed for a long time that the paramagnetic wall relaxation is independent of gas pressure. It was discovered recently, that the ferromagnetic relaxation time has an inverse pressure dependence. However, in our SQUID measurement we surprisingly found that the T_1 is linearly dependent on the pressure of the ^{3}He gas. Therefore, we built a dedicated experiment to study this pressure dependence at room temperature. The study suggests that the relaxation we observed is due to the paramagnetic wall relaxation and the pressure dependence comes from the diffusion of ^{3}He inside the cell because the diffusion speed depends on the pressure. Our study of the T_1 pressure dependence is summarized and presented in the next section.

As the name suggests, the field-gradient induced T_1 relaxation is due to the ^{3}He moving in a non-uniform magnetic field. This problem is further divided into two regimes, the slow diffusion limit and the fast diffusion limit. This problem has been extensively studied in the context of the T_2 relaxation. T_2 is also called transverse relaxation characterizing how fast the spins dephase during the pulsed nuclear magnetic resonance (pNMR) measurement. In the pNRM measurement, a rf pulse is sent to the sample which tips the spins away from their initial position. When the spins are not aligned with the holding field, they will precess around the holding field. At the very beginning, all spins have the same phase. The dephasing happens because the field is not uniform so that different spin will precess at different speeds. In the slow diffusion limit, the time scale of the dephasing is much shorter than the time scale of the diffusion of spins in the cell. In this case, diffusion makes T_2 shorter. In the contrary, when the diffusion is much faster than the dephasing (fast diffusion limit), diffusion tends to average out the field non-uniformity. Therefore, diffusion actually helps increase the T_2. Most of the study of the slow diffusion is related to the water or liquid sample due to their relatively small diffusion constant. Fast diffusion is usually associated with gas samples such as polarized ^{3}He and different techniques are developed to solve this problem. In our SQUID experiment, we found that the diffusion of ^{3}He at 4.2 K falls into the slow diffusion limit and the measured T_2 is much longer than the prediction using the fast diffusion result. Hence, we developed a new approach to solve this gradient-induced relaxation, applicable to both slow and fast diffusion limits at the same time. It also can be used in the intermediate regime which is frequently encountered in the gas pNMR. More interestingly, our approach also solves T_1 in both limits and it turns out that T_1 has different forms in these two limits, which has never been discussed in the literatures. The detailed discussion of the gradient-induced T_1 and T_2 relaxations are presented in the second section of this chapter.

4.1 Pressure Dependence of Wall Relaxation in the Polarized ^{3}He Gaseous Cells

Spin polarized ^{3}He gas has been widely used in polarized nuclear targets for lepton scattering experiments [141] and as a signal source in Magnetic Resonance Imaging (MRI) of lung air space [95]. Recently, it has also been used in searches of exotic spin-dependent interactions [108]. These experiments take advantage of large non-equilibrium polarizations of ^{3}He obtained through spin-exchange with optically polarized Rb or Rb/K vapor mixture. The production and storage of polarized ^{3}He gas crucially depend upon longitudinal relaxation times (T_1). Among many factors contributing to the T_1 relaxation, the most important ones are the ^{3}He dipole-dipole interaction [102], magnetic field gradient induced relaxation [29] and wall relaxation. The least understood and hardest to control among these three effects is the relaxation due to the wall.

Although a thorough understanding of the nature of the wall relaxation is lacking, it is widely believed that relaxation rates due to paramagnetic sites in the wall do not depend upon the density of the gas. This is understood in the following way: the wall collision rate per unit area is known as $n\bar{v}/4$, where n is the number density of the gas and $\bar{v}$ is the mean velocity; assuming α is the depolarization probability per collision due to paramagnetic impurities, the relaxation rate $1/T_1$ can be expressed as [51]

$$\frac{1}{T_1} = \frac{\frac{1}{4}\int \alpha n\bar{v} dS}{\int n dV} = \frac{\alpha\bar{v}S}{4V}, \tag{4.2}$$

where S is the total surface area of the cell, V is the volume of the cell, and n is uniform across the cell. As long as α has no dependence on the gas density or pressure, T_1 is also independent of gas pressure.

In this paper, we present our recent T_1 measurements on polarized ^{3}He cells which show a linear pressure dependence of T_1, different from what has been discussed above. In our experiment, the measured T_1 is significantly reduced from tens of hours to tens of minutes by just decreasing the pressure of ^{3}He gas one hundred times. After excluding dipole-dipole and gradient induced T_1 relaxation, the observed pressure dependence can only be explained by the wall relaxation, which is, however, completely opposite to the pressure dependence observed in the ferromagnetic wall relaxation under the weak collision limit [75]. As the cells tested have never been exposed to high fields, ferromagnetic relaxation cannot be the dominant relaxation mechanism, and paramagnetic relaxation is the last candidate to account for the observed T_1 relaxation. These T_1 measurements have been carried out on cells with surfaces of Cs/Rb-coated pyrex and bare pyrex, and at temperatures 4.2 K and 295K, suggesting that the observed linear pressure dependence is likely a general property of the paramagnetic wall relaxation regardless of the surface and temperature. We also present a model to explain the observed linear pressure dependence by taking into account the diffusion of the spins. This new model also resolves the discrepancies between theories and experiments found in [31, 91] and explains a recent finding that polarization and T_1 are enhanced by adding ^{4}He into the cell [32].

The T_1 measurements at 295 K and 4.2 K were carried out using the Free Induction Decay (FID) technique. ^{3}He was filled and refilled in 48 mm OD spherical detachable cells to 1 or 2 atm, using a ^{3}He/N$_2$ gas handling system. The detachable cell was made of Rb-coated pyrex and had an O-ring valve connected to it through a capillary pyrex tubing with an i.d. of 1.5 mm and a length of 18 cm to restrict gas exchange between the valve and the cell, so that the depolarization from the valve was minimized. The detachable cells were always polarized at either 1 or 2 atm, and then diluted to different pressures (0.025 to 0.43 atm) using different dilution volumes. The pressure in the detachable cell was monitored by a pressure gauge connected between the volume and the cell.

In the 4.2 K experiment, we measured T_1 of ^{3}He in cylindrical pyrex cells immersed in liquid ^{4}He stored in a dewar. The cylindrical cell had an i.d. of 8 mm and a length of 25 mm. The top of the cell was attached to a thin pyrex tube with an i.d. of 3 mm and a length of 68 cm. The other side of the tube was connected to an O-ring valve outside the dewar, where the detachable cell is mounted. A gas flow restriction (0.8 mm i.d. and 3 mm long) was added to the connection point between the tube and the cell to minimize the gas exchange between them. A dilution volume was also connected for diluted T_1 measurements, similar to the 295 K measurement. After dilution, the remaining polarized ^{3}He gas in the detachable cell was allowed to diffuse into the cylindrical cell. The pressure in the cylindrical cell can be varied from 6.4×10^{-4} atm to 0.19 atm. Four cylindrical cells with identical dimensions but different surfaces (two bare pyrex and two Cs-coated pyrex) were used.

The 295 K T_1 measurements were carried out at 39.5 kHz using a homemade FID

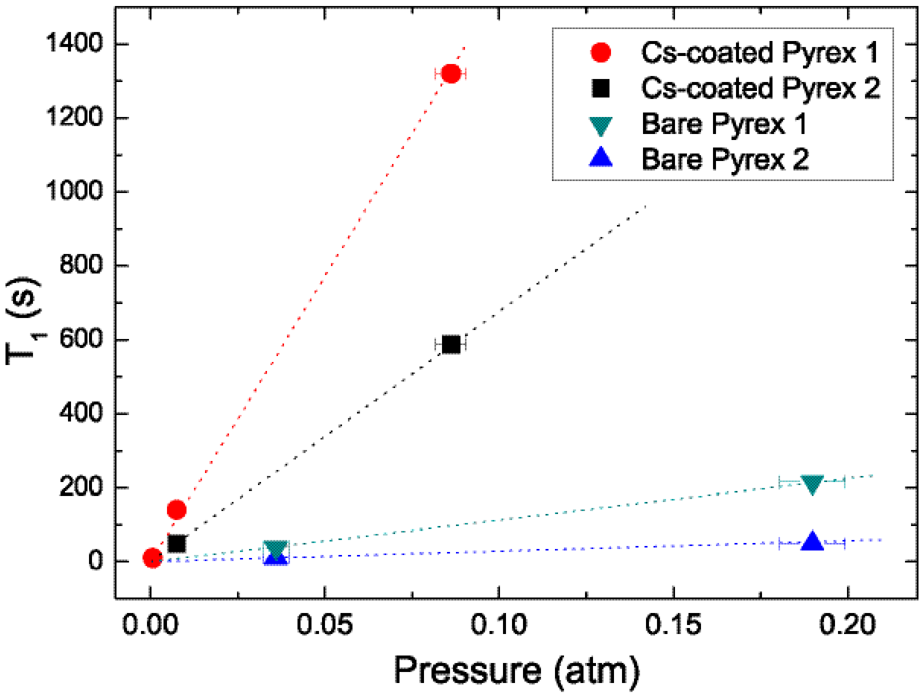

FIGURE 4.1: (Color online) T_1 of ^{3}He in four cylindrical cells at 4.2 K. Two cells are made of bare pyrex (up-triangle and down-triangle) and the other two are made of Cs-coated pyrex (square and circle).

polarimetry and also at 24 kHz using a commercial polarimetry made by Amersham Health; whereas the 4.2 K measurements were performed at 12 kHz, using Superconducting QUantum Interference Device (SQUID) manufactured by StarCryo. While the 39.5 kHz FID polarimetry has a higher signal-to-noise ratio than the 24 kHz polarimetry, the RF noises from its pre-amplifier are bigger. In all FID measurements, a small tipping angle, resulting in about 1% polarization loss, was applied. This loss was subtracted when extracting T_1 from the data. Two different Helmholtz coil pairs were used and the field gradients were measured to be < 2.3 mG/cm for the 295 K measurement and < 2.2 mG/cm for the 4.2 K measurement. The gradient induced T_1 was more than one thousand hours [29], and was negligible compared to the measured T_1. The dipole-dipole induced T_1 was calculated [98, 102], and subtracted from the measured T_1 values. Hence, all T_1s shown below are due to wall relaxation only.

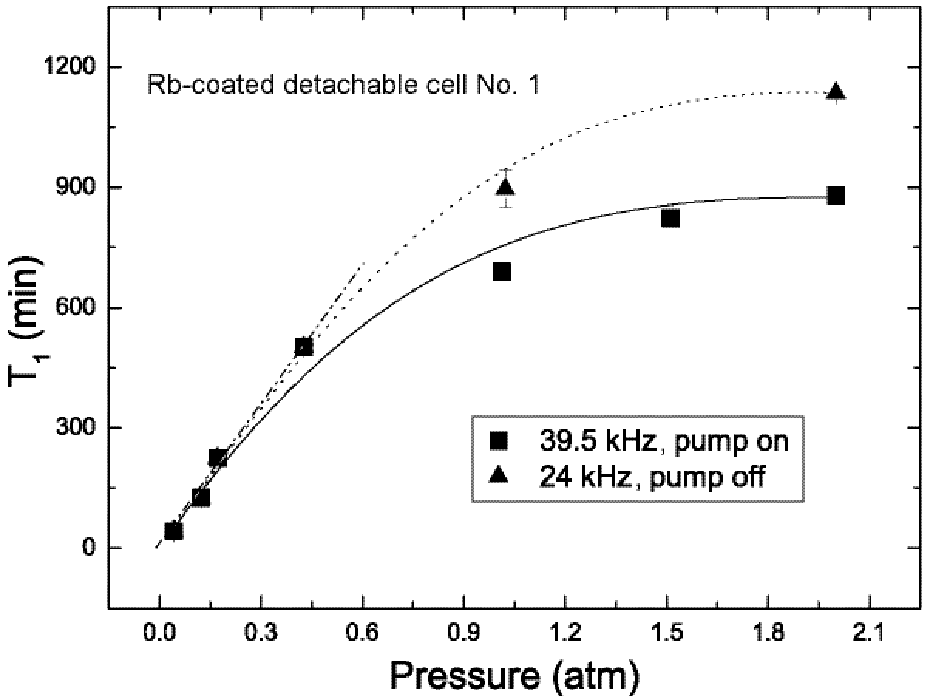

FIGURE 4.2: T_1 of ^{3}He in the Rb-coated detachable cell at 295 K. The dashed line is the linear fit to the first four data points below 0.43 atm. The dotted line is the fit using Eq. (4.3) to the four square points below 0.43 atm and the two triangles points. The solid line is the fit using Eq. (4.3) to all the squares.

At 4.2 K, when the pressure of the gas is reduced, T_1 decreases proportionally (Figure 4.1). From a linear fit of the data (dashed lines), it clearly shows that all the fitted lines pass through the origin, which suggests $T_1 \propto p$. For bare pyrex cells, the minimum T_1 we measured is 10.1±0.3 s at 3.6×10^{-2} atm. If the pressure is further reduced, T_1 becomes so short that a complete T_1 measurement becomes difficult. Cs coating helps increase T_1 by more than two orders of magnitude. This allows the pressure to be further reduced to 6.4×10^{-4} atm. However, even with Cs coating, T_1 at this pressure is only 10.4±0.6 s (the first solid circle in Figure 4.1). Therefore, at low pressure, the pressure dependent T_1 relaxation at 4.2 K is the dominant relaxation mechanism.

At 295 K, the Rb-coated detachable cells have T_1 on the order of tens of hours. This makes the low pressure T_1 measurement easier and also enables us to access the T_1-pressure relationship for a different surface and temperature in addition to the 4.2 K data. The detachable cells have never been exposed to fields higher than 30 G. Measurements of T_1 have been done to cells before and after degaussing using a commercial demagnetizer, and no changes have been seen within experimental uncertainties. The first detachable cell has $T_1 = 690 \pm 21$ min at 1 atm using the 39.5 kHz polarimetry. When the ^{3}He pressure is reduced to below 0.43 atm, the measured T_1 exhibits a linear pressure dependence (Figure 4.2). By fitting the first four points linearly (dashed line), ranging from 0.042 to 0.43 atm, it yields $T_1 = 1188 \times p$ min. This linear dependence does not hold when the pressure is above 0.43 atm, and T_1 at 2 atm does not change too much from T_1 at 1 atm. This clearly indicates that some other relaxation mechanisms, which are negligible at low pressure, become important at high pressure since the paramagnetic relaxation becomes less pronounced with increasing pressures. In a different experiment, we observed that the continuous RF noise broadcasted by the RF amplifier rendered polarization loss during the T_1 measurement [143]. In this experiment, a mechanical pump and a turbo pump were used to maintain the vacuum of the dilution volume throughout the experiment. We indeed observed that the background noise level in the pickup coil increased with the pumps running. Therefore, we repeated the non-diluted 1 atm and 2 atm T_1 measurements with all pumps off. The less noisy 24 kHz polarimetry was used in these measurements. The repeated measurements showed an increase of T_1 by roughly 200 min and 300 min at 1 atm and 2 atm, respectively. However, in the repeated measurements, T_1 still flattens out at 2 atm. As shown in [74], all their non-magnetized/demagnetized Rb-coated cells exhibit weak ferromagnetic relaxation behavior. This leads us to believe that our cells are also subject to ferromagnetic relaxation to some extent. As ferromagnetic relaxation has an inverse pressure dependence $T_1 \propto 1/p$ [75], it is negligible at low pressures; whereas, at high pressures, it becomes more prominent and therefore comparable to the paramagnetic relaxation. This could explain the flattening behavior of T_1. Hence, the measured T_1 relaxation can be attributed to three mechanisms, expressed as

$$\frac{1}{T_1} = \frac{1}{c_1 p} + \frac{1}{c_2} + \frac{p}{c_3}. \tag{4.3}$$

The first term is the paramagnetic wall relaxation, which depends on pressure linearly ($T_1 = c_1 p$); the second term is RF noise-induced relaxation, which has no pressure dependence ($T_1 = c_2$); the last term is the ferromagnetic relaxation, which inversely depends on pressure ($T_1 = c_3/p$) [75, 126]. Using Eq. (4.3) to fit the 39.5 kHz data in Figure 4.2 (solid line), one obtains $c_1 = 1288 \pm 110$ min/atm, $c_2 = 2754 \pm 251$ min and $c_3 = 5082 \pm 1641$ min·atm. If the two repeated measurements together with the four data points below 0.43 atm were used for the fit (dotted line), c_2 changes to $c_2 \geqslant 10086$ min, indicating $1/c_2$ is zero within fitting errors. This suggests that the RF noise in the repeated measurements is negligible.

We also tested another Rb-coated detachable cell, which has a longer T_1 at 1 atm ($T_1 = 1001 \pm 11$ min), measured by the 39.5 kHz polarimetry. This cell also shows the linear pressure dependence with pressure below 0.25 atm (Figure 4.3); and beyond this pressure, T_1 starts to flatten out as well. Fitting the data to Eq. (4.3) yields $c_1 = 1757 \pm 71$ min/atm, $c_2 = 2959 \pm 362$ min and $c_3 \geqslant 10113$ min·atm. c_2 of this cell is comparable to c_2 of the first one as expected, since the RF noise-induced T_1 should be independent of which cell is used. Both c_1 and c_3 are larger than those of the first cell, which suggests that both paramagnetic and ferromagnetic wall relaxations of the second cell are weaker than those of the first one. The 1 atm T_1 was also measured using 24 kHz polarimetry with all pumps off. T_1 in this case increases by roughly 236 min.

Once ferromagnetic wall relaxation and RF noise-induced relaxation are excluded, the T_1 relaxation measurements at both 295 K and 4.2 K clearly show the linear

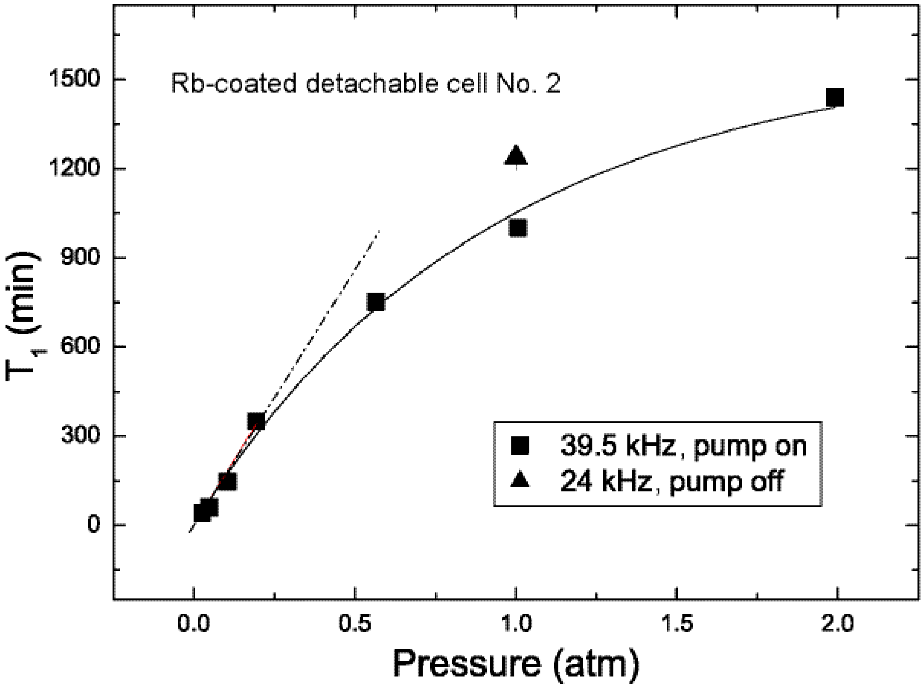

FIGURE 4.3: T_1 of ^{3}He in the second detachable cell which has longer T_1 at 1 atm. The dashed line is the linear fit to the four data points with pressure below 0.25 atm. The solid line is a fit using Eq. (4.3) to all 39.5 kHz data labeled as squares.

pressure dependence, which is contradictory to Eq. (4.2). The derivation of Eq. (4.2) implicitly assumes ballistic collisions between spins and the wall, which is only true when spins are in the vicinity of the wall. When far away from it, spins move in a diffusive manner. Hence, the effective speed, at which it moves to the wall, is much slower than its thermal velocity. As majority of the spins are not close to the wall, a more appropriate model to describe the wall relaxation should take into account the diffusion process. In [39], Chupp *et al.* used the diffusion equation to calculate the spatial distribution of ^{3}He polarization inside a high pressure double cell system. We will also use the diffusion equation, together with depolarizing boundaries, to describe the surface relaxation of ^{3}He. It should be noted that ferromagnetic relaxation does not fit into this surface relaxation model because it happens not only on the surface but also in the vicinity of the surface. Since ferromagnetic impurities produce much stronger dipole field than paramagnetic impurities, spin can be depolarized even it does not have a contact with the surface. In other words, ferromagnetic relaxation actually occurs in a region adjacent to the surface impurities. In the strong collision limit of the ferromagnetic relaxation, the dipole field is so strong that the adjacent relaxation region extends to the entire cell. In this case, the relaxation rate converges to the gradient-induced relaxation [75, 126].

Let $\rho(r,t)$ represent the polarization of ^{3}He gas inside a spherical cell as a function of position r measured from the center of the cell and time t. The diffusion equation of the polarization ρ is written as

$$D\nabla^2\rho = \frac{\partial\rho}{\partial t}, \tag{4.4}$$

where D is the diffusion constant of ^{3}He gas. Since spins lose their polarization only at the surface with probability α, the boundary condition is written as

$$\frac{\partial\rho(r,t)}{\partial r}|_{r=0} \neq \infty \tag{4.5}$$

$$\frac{\partial\rho(r,t)}{\partial r}|_{r=R} = -\alpha\rho(R,t), \tag{4.6}$$

where R is the radius of the cell. The solution is

$$\rho(r,t) = \sum_{k=1}^{\infty} A_k j_0(\frac{x_k r}{R}) \exp(\frac{-x_k^2 Dt}{R^2}), \tag{4.7}$$

where j_0 is the zeroth order spherical Bessel function, x_k is the kth root of Eq. (4.6), which can be re-written as

$$x_k j_0'(x_k) + \alpha R j_0(x_k) = 0, \tag{4.8}$$

and A_k is determined by

$$A_k = \frac{\int_0^R \rho(r,0) j_0(\frac{x_k r}{R}) r^2 dr}{\int_0^R j_0^2(\frac{x_k r}{R}) r^2 dr}. \tag{4.9}$$

Since terms other than $k = 1$ vanish quickly, only $k = 1$ term contribute to the polarization and T_1 is written as

$$1/T_1 = \frac{x_1^2 D}{R^2} \propto \frac{x_1^2}{nR^2} \propto \frac{x_1^2}{pR^2}. \tag{4.10}$$

The second and third proportionalities use the fact that $D \propto 1/n \propto 1/p$. Therefore, the paramagnetic wall relaxation rate $1/T_1$ does not only depend upon the depolarization probability α (implicitly through x_1) but also on the diffusion constant D. Chen *et al.*[32] found that T_1 of their ^{3}He cells are increased by filling ^{4}He into the cell. This can be explained by the decrease of ^{3}He diffusion constant due to the presence of ^{4}He in the cell. It should be noted that Eq. (4.4) can also be used in situations other than pure ^{3}He gas, for instance ^{3}He in superfluid ^{4}He. In this case, D is the diffusion constant of ^{3}He in superfluid ^{4}He [99, 86], so Eq. (4.4) and the following arguments are still valid. Another observation on Eq. (4.10) is that $1/T_1$ has a quadratic dependence on the surface-to-volume ratio, $1/T_1 \propto 1/R^2 \propto (S/V)^2$ (spherical cell). This quadratic dependence, instead of the linear dependence in Eq. (4.2), suggests that surface to volume ratio has bigger influence on paramagnetic relaxation T_1 than it is previously believed.

Low pressure cells (a few torr) used in Metastability Exchange Optical Pumping (MEOP) have been reported to have long T_1 from several hours to tens of hours [41, 67, 35, 1]. These include both valved cells and permanently sealed cells; and they are usually made of aluminosilicate glass or Cs-coated pyrex with much better glass cleaning process than what we did to our detachable cells. No apparent pressure dependence was observed in the valved MEOP cells, except that, at low enough pressures, the gradient-induced relaxation dominates. This seems to be inconsistent with the pressure dependence we observed. However, these cells usually have hundreds or even thousands of hours of T_1 at 1 atm, considerably longer than our cells (less than 20 hours). Rather than the paramagnetic relaxation, T_1 of those MEOP cells are likely dominated by other relaxation mechanisms, such as the ferromagnetic relaxation and the dipole-dipole relaxation.

T_1 of ferromagnetic wall relaxation has an inverse linear pressure dependence in the weak collision limit, defined as $\omega_0\tau << 1$, where ω_0 is the spin precession frequency and τ is the interaction time of spin with a magnetic site on the surface [75, 126]. In the strong collision limit ($\omega_0\tau >> 1$), T_1 becomes linearly dependent on pressure, which in fact can be understood by the gradient-induced relaxation [75]. As the experimental conditions of both 4.2 K and 295 K measurements are clearly not in the strong collision limit which requires large ferromagnetic site on the surface, and our cells have never been exposed to high fields, the observed pressure dependence cannot be explained by the ferromagnetic relaxation in the strong collision limit.

Chapman and Richards [31] also observed the linear pressure dependence of T_1 in ^{3}He at 4.2 K. They use Eq. (4.2) to describe their findings and the pressure dependence was ascribed to the pressure dependence of α using a two-phase model with ^{3}He in the absorbed phase with a shorter T_1 when a complete monolayer was formed on the surface, and ^{3}He in the bulk phase which has much longer T_1. However, this two-phase picture cannot explain the pressure dependence seen in the experiment by Lusher *et. al.* [91], in which only a partial monolayer was formed. The binding energies W between ^{3}He spin and a specific surface determines when a complete monolayer will be formed. For bare pyrex glass, the binding energy is around 100 K [91]. For Cs and Rb-coated cells, the binding energy are 2.3 K and 2.8 K [44, 33], respectively. In our 4.2 K measurement, for sure a complete monolayer of ^{3}He is formed on the bare pyrex; whereas, in the Cs-coated cell, it is certain that only a partial monolayer is formed. As the pressure dependence is observed in both cases, it further demonstrates that Eq. (4.2) and the two-phase picture are inadequate to describe the experimental data, and the diffusion process is essential to the wall relaxation.

In summary, we conclude that the linear pressure dependence observed in our T_1 measurements is associated with the paramagnetic wall relaxation. This pressure dependence originates from the diffusion process of ^{3}He spins and can be well described by the diffusion equation. It also suggests that it is vital to control the paramagnetic wall relaxation when the diffusions are fast.

This work is mainly based on the paper of Zheng *et al* [149]. The boundary condition Eq. (4.6) used in this work is questioned by Saam *et al* [122]. They proposed a different formula for the relaxing boundary condition in their comment. With certain assumption, they gave an alternative explanation to the observed pressure dependence. We did a finite element analysis to simulate the experiment using their boundary condition and assumptions. However, the simulation result does not agree with the experimental data. We wrote a reply to their comment, demonstrating our FEA result. The reply to their comment is shown in Appendix C. To summarize, the interpretation of the pressure dependence is still under debate and it is an open question that needs to be addressed in the future.

4.2 General Solution to Gradient Induced Transverse and Longitudinal Relaxation of Spins Undergoing Restricted Diffusion

4.2.1 Introduction

Longitudinal relaxation (T_1 relaxation) and transverse relaxation (T_2 relaxation) are the most important parameters in Nuclear Magnetic Resonance (NMR), Magnetic Resonance Spectroscopy and Magnetic Resonance Imaging (MRI). Many factors can contribute to T_1 and T_2 relaxations. It is well known that, for liquid or gaseous samples, such as spin polarized ^{3}He, diffusion in a non-uniform magnetic field can cause both T_1 and T_2 relaxations. In this manuscript, $1/T_1^G$ and $1/T_2^G$ represent the relaxation rates solely due to diffusion in a magnetic field gradient. The transverse relaxation due to diffusion in free space was first solved by Torrey [135]. He generalized the Bloch equation by adding a diffusion term and unveiled that the envelope of the transverse component of the magnetization decays as

$$A(t) = \exp(-\frac{1}{3}D\gamma^2G^2t^3), \tag{4.11}$$

where D is the diffusion constant, γ is the gyromagnetic ratio of the spin and G is a constant gradient. In practice, most diffusion happens in confined spaces, and the stochastic diffusion process is restricted, which makes the problem more complicated. Robertson [119] solved the Bloch-Torrey equation [135] in restricted geometries, by imposing boundary conditions to the equation. His approximate analytical solution showed that the envelop decays exponentially with a constant relaxation rate. This result is valid when $4Dt >> L^2$, where L is the distance between the boundaries. This limit is also known as fast diffusion limit or motional averaging regime, where spins have moved across the geometry many times in a time period t and therefore any fluctuation in the magnetic field averages out and a faster diffusion actually reduces the relaxation. Neuman [101] solved the same problem by calculating the accumulated phases of spins with the assumption that the relative phase distribution of spins is Gaussian in both the slow diffusion and fast diffusion limits. His slow diffusion result reproduces the free diffusion result, Eq. (4.11), and the fast diffusion result is the same as that of Robertson. In the intermediate regime, the Gaussian Phase Approximation (GPA) fails. However, it is crucial to quantitatively understand the intermediate regime because many experiments have shown edge enhancement phenomena in the slow diffusion and intermediate regime, which was recognized later as a localization regime [66]. People have observed that, when water diffuses in microscopic structures, the MRI signal is enhanced at the edge of the structure [112, 70, 17, 27, 69]. Saam *et al.* have also showed a similar edge enhancement effect, using hyperpolarized ^{3}He gas in cells with dimensions of about 1 cm [121]. This effect is ascribed to the more restricted diffusion at the boundary, which lessens the relaxation, and was first described quantitatively by De Swiet [133], using Airy functions. Airy functions have been shown to be the eigenfunction of the Bloch-Torrey equation in the intermediate regime [132]. Axelrod also showed that although GPA fails in the intermediate regime, it can be used to interpolate the result in this regime, which turns out to be close to the exact solution [8]. More detailed discussion on the restricted diffusion in various limits can be found in a review article [61] and references therein.

Despite of the widely used GPA method, Cates *et al.* used the second order time-dependent perturbation theory and carried out an expansion of spin density matrix to obtain both longitudinal and transverse relaxation rates for a spherical cell [29]. Their results works only in the fast diffusion regime, and they further divided the fast diffusion regime into two limits: the high pressure limit $\omega_0 R^2/8\pi D >> 1$ and the low pressure limit $\omega_0 R^2/8\pi D << 1$, where ω_0 is the Larmor precession frequency and R is the radius of the spherical cell. These two limits can be thought of as the characteristic spin precession time $\tau_l = 2\pi/\omega_0$ being much shorter or longer than the characteristic diffusion time in the cell $\tau_d = R^2/4D$, respectively. McGregor [92] used Redfield theory discussed in [130] to solve the same problem also in the fast diffusion regime. Redfield theory is a generalized treatment of the second-order time-dependent perturbation theory. It establishes a set of differential equations obeyed by the spin density matrix. Therefore, it is closely related to the treatment of Cates *et al.* [60]. By calculating autocorrelation function of spin under different geometries, McGregor was able to obtain transverse relaxation rates in the fast diffusion limit for different geometries, including slabs, cylinders and spheres.

In this manuscript, we make an extension to the McGregor's approach, which yields an analytical solution to the transverse magnetization suitable for all diffusion regimes. When $4Dt << L^2$, this solution reproduces Torrey's free diffusion result; when time $4Dt \approx L^2$, it is in the intermediate regime. In these two regimes, edge enhancement effect is also observed. Eventually, when $4Dt >> L^2$, it is in the motional averaging regime and a peak located at the center of the frequency spectrum is observed. We also performed Free Induction Decay (FID) measurements on polarized ^{3}He gas to verify the theoretical results. By changing the number density of the gas, the observed transverse relaxation happens in different diffusion regimes. When the decay envelopes are compared to the theoretical predictions, they are found to be in good agreements, especially in the intermediate regime. In addition to the transverse relaxation, our approach can also be used to calculate longitudinal relaxation in different regimes. We found that the longitudinal relaxation rate $1/T_1^G$ in the slow diffusion limit is twice as fast as that in the fast diffusion limit. As diffusion in the fast diffusion regime is more restricted, it could explain this factor of two difference. In this manuscript, we solve the problem in 1D for clarification purpose. However, it can be easily extended to 3D with complex geometries since one only needs to calculate the corresponding probability density function. Once the density function is known, the relaxation rate can be calculated readily, which makes this approach suitable for numerical simulations of complex geometries.

4.2.2 Redfield theory for magnetic field gradient-induced relaxations

For simplicity, let spins diffuse in a cubic cell with length L. A non-uniform magnetic field is applied along the $\hat{z}$ direction. At time $t = 0$, we track a spin starting at $\vec{x}'_c$. As time evolves, the expected position of the spin will change due to the diffusion process. Therefore, we use $\langle \vec{x}'(t) \rangle$ to represent the expected position of spin at some later time t and has the property that $\langle \vec{x}'(0) \rangle = \vec{x}'_c$. Since the field is non-uniform over the box, the spins also see fluctuating magnetic fields during diffusion. The fluctuating field $\vec{B}'$ can be treated as a perturbation to the zeroth order mean field $\vec{B}(\langle \vec{x}' \rangle)$ by taking Taylor expansion around $\vec{x} = \langle \vec{x}' \rangle$,

$$\vec{B}' \equiv \vec{B}(\vec{x}(t)) - \vec{B}(\langle \vec{x}'(t) \rangle) = \vec{\nabla}\vec{B} \cdot (\vec{x}(t) - \langle \vec{x}'(t) \rangle). \tag{4.12}$$

As described in [130], Redfield theory gives solutions to the problem with fluctuating magnetic fields. In our case, the applied field is constant in time; however the time dependence appears because of the diffusion process. The equation of motion for the transverse and longitudinal components of the spin can be written as [130]

$$\begin{aligned}\frac{d}{dt}\langle S_T \rangle \equiv \frac{d}{dt}(\langle S_x \rangle + i\langle S_y \rangle) = \gamma(\langle \mathbf{S}_T \rangle \times \mathbf{B}) - \\ \gamma^2 \left\{ \frac{1}{2}\left[J_{B'_x}(\omega) + J_{B'_y}(\omega) \right] + J_{B'_z}(0) \right\} \langle S_T \rangle\end{aligned} \tag{4.13}$$

$$\frac{d}{dt}\langle S_z \rangle = -\gamma^2 \left[J_{B'_x}(\omega) + J_{B'_y}(\omega) \right] \langle S_z \rangle, \tag{4.14}$$

where S_T is the transverse component of spins, $\mathbf{B} = B_z(\langle \vec{x}' \rangle)\hat{z}$, $\omega = \gamma B_z(\langle \vec{x}' \rangle)$, the Larmor precession frequency of spins at field strength $B_z(\langle \vec{x}' \rangle)$, and $J_{B'_x}$ is defined as [130]

$$J_{B'_x}(\omega) = \int_0^t \overline{B'_x(t-\tau)B'_x(t)} e^{-i\omega\tau} d\tau. \tag{4.15}$$

The bar denotes an ensemble average of the autocorrelation of the perturbed magnetic field. $J_{B'_z}(0)$ has the similar definition with B'_x replaced by B'_z and $\omega = 0$. The first term in Eq. (4.13) describes the precession of the spin under the field $B_z(\langle \vec{x}' \rangle)$, and the second term gives the transverse relaxation rate $1/T_2^G$; whereas Eq. (4.14) describes the longitudinal relaxation.

It should be noted that Eq. (4.15) was originally written in [130] as an integral from 0 to infinity. It was argued that the autocorrelation of the magnetic field would vanish quickly after a critical time τ_c, and consequently, integration from 0 to infinity introduces negligible errors as long as $t >> \tau_c$. For the case considered here, τ_c can be defined as $\tau_c \equiv (L/2)^2/4D$. When the diffusion is slow, the above approximation is invalid, and Eq. (4.15) must be used. By utilizing Eq. (4.12) and realizing the fact that diffusions in $\hat{x}$, $\hat{y}$ and $\hat{z}$ directions are independent of each other, $J_{B'_x}(\omega)$ can be re-written as

$$J_{B'_x}(\omega) = (\frac{\partial B'_x}{\partial x})^2 J_x(\omega) + (\frac{\partial B'_x}{\partial y})^2 J_y(\omega) + (\frac{\partial B'_x}{\partial z})^2 J_z(\omega), \tag{4.16}$$

where $J_x(\omega)$ is expressed as

$$J_x(\omega) = \int_0^t \overline{(x(t-\tau) - \langle x'(t) \rangle)(x(t) - \langle x'(t) \rangle)} e^{-i\omega\tau} d\tau, \tag{4.17}$$

and similar for $J_y(\omega)$ and $J_z(\omega)$. In general, $J_x(\omega)$ is time-dependent and the relaxation rates are also time-dependent. However, it will be shown that, in the fast diffusion limit, $J_x(\omega)$ approaches some constant values and $J_x(\omega) = J_y(\omega) = J_z(\omega)$. Hence, one can define the longitudinal relaxation rate $1/T_1^G$ as

$$\frac{1}{T_1^G} = \gamma^2 (|\nabla B_x|^2 + |\nabla B_y|^2) \Re \left[J_x(\omega) \right], \tag{4.18}$$

where $\Re\left[\cdot\right]$ indicates taking the real part. Hence, in the fast diffusion limit, the transverse relaxation rate $1/T_2^G$ can also be defined as

$$\frac{1}{T_2^G} = \frac{1}{2T_1^G} + \gamma^2 \left|\nabla B_z\right|^2 J_x(0). \tag{4.19}$$

Magnetic Field Gradient-induced Transverse Relaxation Rate $1/T_2^G$

The expected position of spin $\langle x'(t) \rangle$ at time t can be computed as

$$\langle x'(t) \rangle = \int_{-L/2}^{L/2} x\rho(x,t|x'_c,0)dx, \tag{4.20}$$

where $\rho(x,t|x_0,t_0)$ is the conditional probability density function of spin at position x at time t, if the spin is at x_0 at time t_0 ($t_0 = t - \tau$). It is apparently that Eq. (4.20) satisfies the condition $\langle x'(0) \rangle = x'_c$.

In order to compute $J_x(0)$, one needs to calculate position autocorrelation function, which, by definition, can be expressed as

$$\overline{(x(t-\tau) - \langle x' \rangle)(x(t) - \langle x' \rangle)} =$$

$$\int_{-L/2}^{L/2} \int_{-L/2}^{L/2} (x_0 - \langle x' \rangle)(x - \langle x' \rangle)\rho(x,t|x_0,t_0)\rho(x_0,t_0|\left\langle x' \right\rangle,0)dxdx_0. \tag{4.21}$$

Due to the symmetry of the cubic cell, $\rho(x,t|x_0,t_0)$ can be found by decomposing the 3D diffusion equation into 1D problem, subject to the boundary condition

$$\frac{\partial}{\partial x}\rho(x,t|x_0,t_0)|_{x=\pm L/2} = 0,$$

and the initial condition

$$\rho(x,t_0|x_0,t_0) = \delta(x - x_0).$$

The solution is found to be

$$\rho(x,t|x_0,t_0) = \frac{1}{L} + \frac{2}{L}\sum_{n=1,3}^{\infty} e^{-\frac{n^2\pi^2 D\tau}{L^2}} \sin(\frac{n\pi x}{L})\sin(\frac{n\pi x_0}{L})$$

$$+ \frac{2}{L}\sum_{n=2,4}^{\infty} e^{-\frac{n^2\pi^2 D\tau}{L^2}} \cos(\frac{n\pi x}{L})\cos(\frac{n\pi x_0}{L}). \tag{4.22}$$

By substituting Eq. (4.22) into Eq. (4.21), one obtains

$$\overline{(x(t-\tau)-\langle x'\rangle)(x(t)-\langle x'\rangle)} = \frac{8L^2}{\pi^4}\sum_{n=1,3}^{\infty}\frac{1}{n^4}\exp(-\frac{n^2\pi^2 D\tau}{L^2}) + \langle x'\rangle^2$$

$$-\frac{4\langle x'\rangle L}{\pi^2}\sum_{n=1,3}^{\infty}\frac{1}{n^2}\exp(-\frac{n^2\pi^2 Dt}{L^2})\sin(\frac{n\pi\langle x'\rangle}{L})\sin(\frac{n\pi}{2})$$

$$-\frac{4\langle x'\rangle L}{\pi^2}\sum_{k=2,4}^{\infty}\frac{1}{k^2}\exp(-\frac{k^2\pi^2 Dt_0}{L^2})\sin(\frac{k\pi\langle x'\rangle}{L})\sin(\frac{k\pi}{2})$$

$$+\frac{16L^2}{\pi^4}\sum_{n=1,3}^{\infty}\sum_{k=2,4}^{\infty}\frac{k^2+n^2}{n^2(k^2-n^2)^2}\exp(-\frac{n^2\pi^2 D\tau}{L^2})\exp(-\frac{k^2\pi^2 Dt_0}{L^2})$$

$$\times\cos(\frac{k\pi\langle x'\rangle}{L})\cos(\frac{k\pi}{2}). \tag{4.23}$$

Instead of substituting Eq. (4.23) into J_x directly, one can first take the slow diffusion or fast diffusion limits on it. It can be shown (see Appendix B) that, in the slow diffusion limit $4Dt << (L/2)^2$, Eq. (4.23) is simplified to

$$\overline{(x(t-\tau)-\langle x'\rangle)(x(t)-\langle x'\rangle)} \approx 2D(t-\tau). \tag{4.24}$$

$J_x(0)$ is then calculated as

$$J_x(0) = \int_0^t 2D(t-\tau)d\tau = Dt^2. \tag{4.25}$$

This is also true for $J_y(0)$ and $J_z(0)$. As $J_{x,y,z}(0)$ is time-dependent, the relaxation rate is also time-dependent. One has to substitute $J_{x,y,z}(0)$ into Eq. (4.13) directly to compute S_T,

$$\frac{d}{dt}\langle S_T\rangle = \gamma(\langle \mathbf{S}_T\rangle \times \mathbf{B}(\langle \vec{x}'\rangle)) - (\frac{1}{2T_1} + \gamma^2|\nabla B_z|^2 Dt^2)\langle S_T\rangle. \tag{4.26}$$

If one assumes that the gradient in one direction $\partial B_z/\partial x \equiv G$ dominates, then $|\nabla B_z| \approx G$ and $B_z = B_z(0) + G\langle x'\rangle \approx B_z(0) + Gx'_c$. $\langle x'\rangle \approx x'_c$ because spins are localized in the slow diffusion limit and the expected position at time t will not change significantly from their initial positions. Integrating upon time, Eq. (4.26) becomes

$$\langle S_T\rangle = S_0 \exp[i\gamma(B_z(0) + Gx'_c)t]\exp(-\frac{\gamma^2 G^2 D t^3}{3} + \frac{t}{2T_1^G}). \tag{4.27}$$

This coincides with 1D diffusion result derived by Torrey [135]. Torrey's derivation assumes free diffusion without boundaries, which is equivalent to the slow diffusion in a confined volume, as boundaries are not present to spins when diffusion is slow.

In the fast diffusion limit, $4Dt >> (L/2)^2$, all the exponential terms containing t in Eq. (4.23) vanish, so does $\langle x'\rangle^2$ term, which can be proved easily by taking the limit $4Dt/L^2 \to \infty$ in Eq. (4.20). Therefore, the only surviving term is the first one,

$$\overline{(x(t-\tau) - \langle x'\rangle)(x(t) - \langle x'\rangle)} = \sum_{n=1,3}^{\infty} \frac{8L^2}{n^4\pi^4} e^{-\frac{n^2\pi^2 D\tau}{L^2}}. \tag{4.28}$$

$J_x(0)$ in this case becomes

$$J_x(0) = \int_0^t \sum_{n=1,3} \frac{8L^2}{n^4\pi^4} e^{-\frac{n^2\pi^2 D\tau}{L^2}} d\tau = \frac{L^4}{120D}, \tag{4.29}$$

where the fact that $4Dt >> (L/2)^2$ is used again after the integration. $J_y(0)$ and $J_z(0)$ are the same as $J_x(0)$ in this limit. Substituting them back into Eq. (4.13), one obtains

$$\langle S_T\rangle = S_0 \exp[i\omega_0 t - (\frac{1}{2T_1} + \frac{\gamma^2 L^4 |\nabla B_z|^2}{120D})t]. \tag{4.30}$$

As $\langle x'(t)\rangle$ approaches zero in the fast diffusion limit, all the spins precess at the same central frequency $\omega_0 = \gamma B_z(0)$, no matter where the spin is initially. This is also known as motional averaging regime. If gradient in one direction dominates the other two ($|\nabla B_z| \approx G$), the transverse component decays with a constant relaxation rate $1/T_2^G$ given by

$$\frac{1}{T_2^G} = \frac{1}{2T_1^G} + \frac{\gamma^2 L^4 G^2}{120D}. \tag{4.31}$$

This result is also derived by McGregor [92] and Robertson [119] using GPA method. However, it will be shown in the discussion section that, by numerically calculating $J_x(0)$ using Eq. (4.23) without any approximation, one can obtain the frequency spectrum of the precession signal in various limits, which cannot be obtained from McGregor and Robertson's methods. As a constant gradient is applied, the frequency spectrum is actually a frequency encoded 1D image. In the slow diffusion limit, peaks are observed at the edge of the geometry, known as edge enhancement; whereas in the fast diffusion limit, a resonance peak is observed at the center of the spectrum.

In the intermediate region $4Dt \approx (L/2)^2$, one has to substitute Eq. (4.23) directly into $J_x(0)$ and then calculate Eq. (4.13). Unfortunately, no concise analytical form of $S_T(\langle x'\rangle)$ can be obtained in this regime. Hence, a numerical calculation of $S_T(\langle x'\rangle)$ is performed and compared with Free Induction Decay (FID) measurements on gaseous ^{3}He cells, and a good agreement in the intermediate regime is shown, see Sec. III.

Magnetic Field Gradient-induced Longitudinal Relaxation Rate $1/T_1^G$

In order to compute Eq. (4.14), one needs to obtain $J_x(\omega)$ first. In the slow diffusion limit ($4Dt << (L/2)^2$), Eq. (4.24) should be used,

$$\begin{aligned} J_x(\omega) &= \int_0^t 2D(t-\tau)e^{-i\omega\tau}d\tau \\ &= \frac{2D(1-e^{-i\omega t}-i\omega t)}{\omega^2}. \end{aligned} \tag{4.32}$$

Since, in most cases, $\omega >> 1$, $\Re(1 - e^{-i\omega t}) = 1 - \cos\omega t$ is a fast oscillating function, which averages to 1. Consequently, substituting $\Re[J_x(\omega)]$ into Eq. (4.18), the longitudinal relaxation has an averaged decay rate as

$$\frac{1}{T_1^G} = \gamma^2(|\nabla B_x|^2 + |\nabla B_y|^2)\frac{2D}{\omega^2} = 2D\frac{|\nabla B_x|^2 + |\nabla B_y|^2}{B_0^2}, \tag{4.33}$$

where $\omega = \gamma B_z(\langle\vec{x}'\rangle) \approx \gamma B_z(0) \equiv \gamma B_0$.

In the fast diffusion limit ($4Dt >> (L/2)^2$), Eq. (4.28) should be used to calculate $J_x(\omega)$,

$$\begin{aligned} J_x(\omega) &= \frac{8L^2}{\pi^4}\int_0^\infty \sum_{n=1,3}^{\infty} \frac{1}{n^4} e^{-\frac{n^2\pi^2 D\tau}{L^2}} e^{-i\omega\tau} d\tau \\ &= \frac{8L^2}{\pi^4}\sum_{n=1,3}^{\infty}\frac{1}{n^4}\frac{1}{\frac{n^2\pi^2 D}{L^2} + i\omega}. \end{aligned} \tag{4.34}$$

Hence, the real part of $J_x(\omega)$ is written as

$$\Re[J_x(\omega)] = \frac{8L^4 D}{\pi^2}\sum_{n=1,3}^{\infty}\frac{1}{n^2}\frac{1}{n^4\pi^4 D^2 + \omega^2 L^4}. \tag{4.35}$$

In the fast diffusion limit with high pressure ($\tau_d/\tau_l = \omega L^2/32\pi D >> 1$), the sum in Eq. (4.35) is simplified to

$$\sum_{n=1,3}^{\infty}\frac{1}{n^2}\frac{1}{\omega^2 L^4} = \frac{\pi^2}{8\omega^2 L^4}, \tag{4.36}$$

and $1/T_1^G$ in this limit becomes

$$\frac{1}{T_1^G} = D\frac{|\nabla B_x|^2 + |\nabla B_y|^2}{B_0^2}, \tag{4.37}$$

It is interesting to see that there is a factor of 2 difference between the slow diffusion $1/T_1^G$ and the high pressure fast diffusion $1/T_1^G$. More discussion on this topic is presented in Sec. IV.

In the fast diffusion with low pressure ($\tau_d/\tau_l = \omega L^2/32\pi D << 1$), the sum in Eq. (4.35) becomes

$$\sum_{n=1,3}^{\infty} \frac{1}{n^6}\frac{1}{\pi^4 D^2} = \frac{\pi^2}{960D^2}, \tag{4.38}$$

and the resultant $1/T_1^G$ in the low pressure limit is

$$\frac{1}{T_1^G} = \frac{\gamma^2 L^4}{120D}(|\nabla B_x|^2 + |\nabla B_y|^2). \tag{4.39}$$

This result is an analogy to the low pressure $1/T_1^G$ derived by Cates *et al.* for a spherical cell geometry [29]. For geometries other than sphere and box, one only needs to recalculate Eq. (4.23) and the corresponding $1/T_1^G$ can be obtained readily through steps illustrated above. This also applies to the transverse relaxation rate $1/T_2^G$ when other geometries are considered.

Magnetic Field Gradient-induced Resonance Frequency Shift

In Eq. (4.13), the imaginary part of the complex function $J_{B'_x}$ and $J_{B'_y}$ gives rise to the shift of precession frequency $\delta\omega$,

$$\delta\omega = \frac{-\gamma^2}{2}\left[|\nabla B_x|^2 + |\nabla B_y|^2\right]\Im\left[J_x(\omega)\right], \tag{4.40}$$

where $\Im\left[\cdot\right]$ means taking the imaginary part. In the slow diffusion limit, substituting Eq. (4.32) into Eq. (4.40) yields

$$\delta\omega = \frac{\gamma D t}{B_0}(|\nabla B_x|^2 + |\nabla B_y|^2). \tag{4.41}$$

It is interesting to note that, in the slow diffusion limit, the frequency shift increases linearly as a function of time, different from the t^3 dependence in the transverse relaxation rate. In addition, Eq. (4.41) does not depend on L as expected because

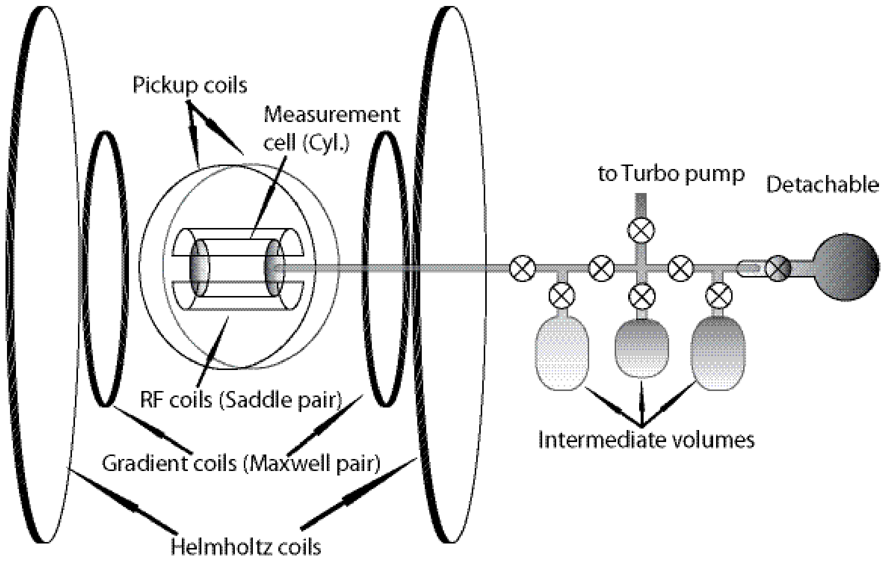

FIGURE 4.4: The apparatus for measuring the transverse relaxation of ^{3}He in the cylindrical measurement cell. ^{3}He in the detachable cell has been polarized by SEOP before it is transferred to the measurement cell.

the slow diffusion limit is equivalent to the free diffusion, in which spins do not see boundaries.

In the fast diffusion limit with high pressures, substituting Eq. (4.34) into Eq. (4.40) and taking the corresponding limit yields

$$\delta\omega = \frac{\gamma^2 L^2}{12\omega_0}(|\nabla B_x|^2 + |\nabla B_y|^2) \tag{4.42}$$

In the fast diffusion limit with low pressures, it yields

$$\delta\omega = \frac{17\omega_0\gamma^2 L^8}{20160 D^2}(|\nabla B_x|^2 + |\nabla B_y|^2) \tag{4.43}$$

These two results are analogies to the frequency shifts derived in [29] for a spherical cell.

4.2.3 Experiments and Results

FID measurements have been performed to measure transverse relaxation of polarized ^{3}He gas at 34.5 kHz. The ^{3}He gas is polarized in a 2 inch diameter spherical detachable cell via Spin-Exchange Optical Pumping (SEOP) technique. The cell is routinely filled with 760 torr ^{3}He and 100 torr N_2. After ^{3}He is polarized, the detachable cell is connected to a measurement cell sitting at the center of the Helmholtz coils through a 2 mm inner diameter glass tube. The measurement cell is made of bare pyrex glass in a cylindrical shape with 2 inch for both the diameter and the length. Three intermediate volumes made of pyrex and a turbo pumping line are connected to the glass transfer tube between the detachable cell and the measurement cell. The schematics of the experimental apparatus is shown in Figure 4.4. Before the measurement, polarized ^{3}He atoms are allowed to diffuse into intermediate volumes first so that the number density of ^{3}He in the detachable cell is diluted. The intermediate volumes are then isolated and the valve between the detachable cell and the measurement cell is opened. Consequently, the rest of ^{3}He in the detachable cell can diffuse freely into the measurement cell. When the pressure in the two cells reaches equilibrium, the valve is closed and FID measurements are carried out.

A pair of 6 inch diameter pickup coils in Helmholtz coil configuration is used, so that the coil has a rather uniform sensitivity over the entire cylindrical cell. Each coil has 2000 turns of 30 AWG wires to maximize the signal. The precession signal at 34.5 kHz is lock-in detected and the envelop of the signal is extracted. The RF coil is a pair of saddle coils with a length of 3.5 inch, a diameter of 3 inch and the opening angle is 120 degrees. Each coil has 10 turns of AWG 22 wires. The axis of the pickup coil, the RF field direction and the magnetic holding field are perpendicular to each other. A RF pulse with a tipping angle $\sim$ 20 degrees is sent to the measurement cell. A pair of gradient coils in Maxwell coil settings [50] is also added to provide a uniform field gradient of 2.3 mG/cm in the holding field or $\vec{z}$ direction. The background gradients are measured to be much smaller than this value and therefore ignored in the calculation shown below.

In Figure (4.5), we show the transverse relaxation measurements of ^{3}He with

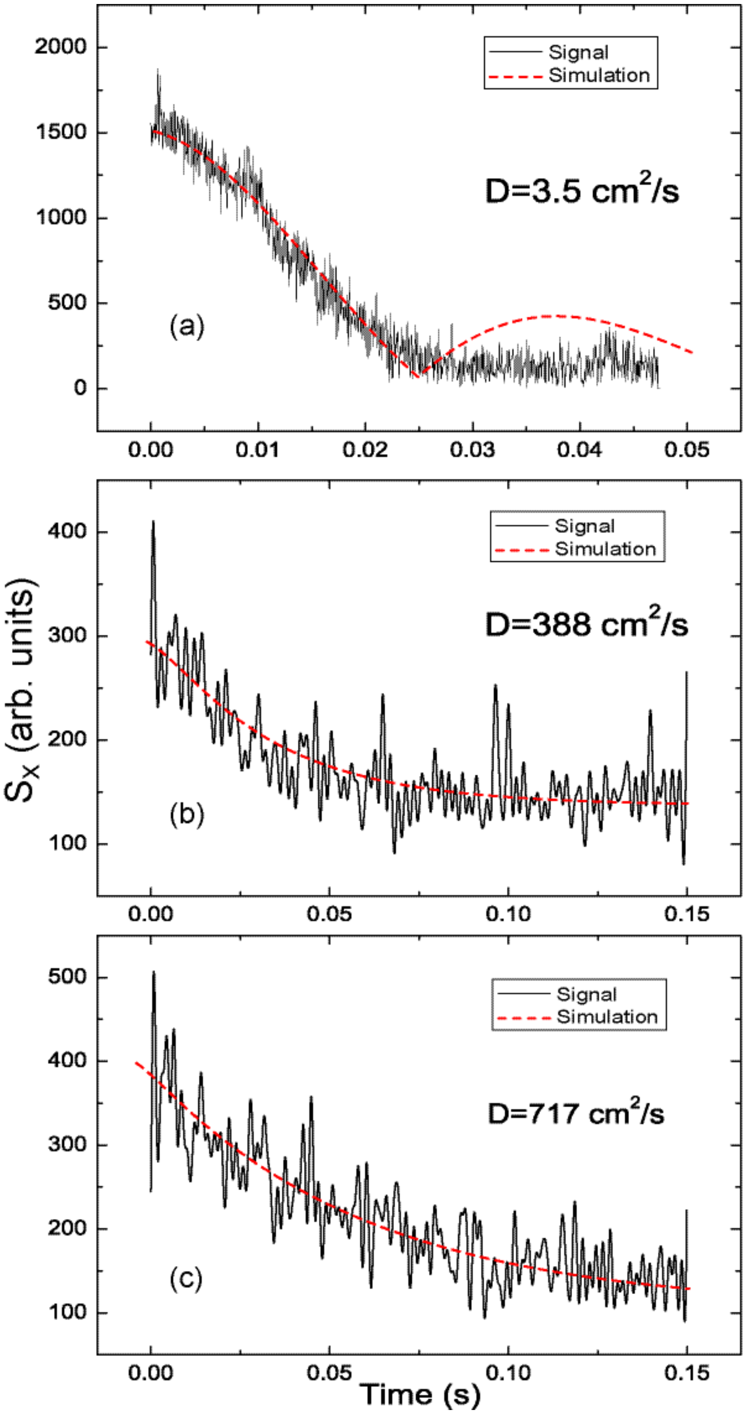

FIGURE 4.5: (Color online)Transverse relaxation measurements with different diffusion constants. (a) is in the slow diffusion regime and the sinc like shape of the decay profile is due to the spin defocus, (b) is in the intermediate regime and (c) is in the fast diffusion regime. Simulation results are shown as dashed lines and compared to the measured decay envelops.

pressures of 327 torr, 2.94 torr and 1.59 torr. The corresponding diffusion constants are 3.5, 388 and 717 cm^2/s, respectively (scaled from 1.5 cm^2/sec for 760 torr ^{3}He, which is measured using Carr-Purcell-Meiboom-Gill method [26]). When using the ratio $(L/2)^2/4Dt$ to characterize the diffusion regime, it is clear that 3.5 cm^2/s is in the slow diffusion regime; whereas 717 cm^2/s is in the fast diffusion regime and 388 cm^2/s is in the intermediate regime close to fast diffusion limit. When diffusion is slow, the decay of signal is mainly due to the dephasing of the spin precessing at different frequencies. This can be understood by taking D as zero, so that the exponential term in Eq. (4.27) is identical to one and a rough estimate of the overall signal S_{all} is simply integrating S_T over the entire cell,

$$S_{all} \approx \int_{L/2}^{-L/2} e^{i(\omega_0+\gamma G x')} dx' \propto e^{i\omega_0 t} \mathrm{sinc}(\frac{\gamma G L t}{2}) \tag{4.44}$$

where sinc(x) is defined as $\sin(x)/x$ and the first zero of sinc function is at $\gamma G L t = 2\pi$. Using the real values of G and L, one can determine $t = 26$ ms. This value is the same as the experimentally measured signal vanishing time $t \approx 26$ ms for the case D=3.5 cm^2/s, see Figure (4.5).

When diffusion is fast, spins will more or less precess at the same frequency (motional averaging) and the diffusion term dedicates the signal decay. As no simple form of S_T can be obtained in the intermediate regime, we numerically calculate $S_T(\langle x' \rangle)$ using the general form of autocorrelation function, Eq. (4.23). To evaluate Eq. (4.23), we compute one hundred terms in each of the first three sums and four hundred terms in the last double sum. We also evaluate $\langle x' \rangle$ up to 100 terms. Once $S_T(\langle x' \rangle)$ is known, it is weighted by $B(\langle x' \rangle)$, the sensitivity of the Helmholtz pickup coil at position $\langle x' \rangle$, and then integrated over the entire cylindrical cell to mimic the measured FID signal. The simulation results, shown as red dashed curves, are compared with measured decay envelops. The background noise of the FID measurement is around 150 arb. units. The simulation curves are shifted up by this amount to account for the background. Good agreements between measurements and simulations are found for the intermediate regime and the fast diffusion regime. One can also use Eq. (4.31) to predict T_2 in Figure (4.5c) as it is in the fast diffusion regime. The prediction yields $T_2 = 0.0589$ s and an exponential fit of the data yields $T_2 = 0.0557$ s, which is very close to the prediction. However, if Eq. (4.31) is used to predict T_2 in Figure (4.5b), it overestimates T_2 by 39% and the profile of the measured relaxation is somewhere between the sinc and exponential. This shows that Eq. (4.31) is inadequete to use in the intermediate regime, and one has to use the non-approximated form of $S_T(\langle x' \rangle)$ to do the calculation.

In the slow diffusion regime, the numerical calculation correctly captures the time when signal vanishes, and it also exhibits a small bump at 0.04 s, due to the partial refocus of spin. However, this bump is not observed in the experiment. It is probably due to the fact that in the simulation, we only take into account the gradient in the longitudinal direction. In reality, although gradients in other directions are smaller than the longitudinal one, they still affect the precession frequency of each individual spin. Consequently, spin refocus is disturbed and the small bump is smeared out.

4.2.4 Discussion

In Sec. III, we numerically calculate $S_T(\langle x' \rangle)$ without any approximation. The time evolution of integrated $S_T(\langle x' \rangle)$ is compared to the FID signal of polarized ^{3}He gas and a good agreement is found, especially in the intermediate regime. It is also interesting to see how S_T changes as a function of position $\langle x' \rangle$ when different diffusion regimes are considered. In Figure 4.6, we show S_T as a function of $\langle x' \rangle$, which is also equivalent to a frequency spectrum due to the linear relationship between ω and $\langle x' \rangle$, known as frequency encoding. The two curves shown in Figure 4.6 are calculated at the time instant $t = 0.02$ s, with $\gamma G = 1000$ rad/s·cm, $L = 1$ cm and

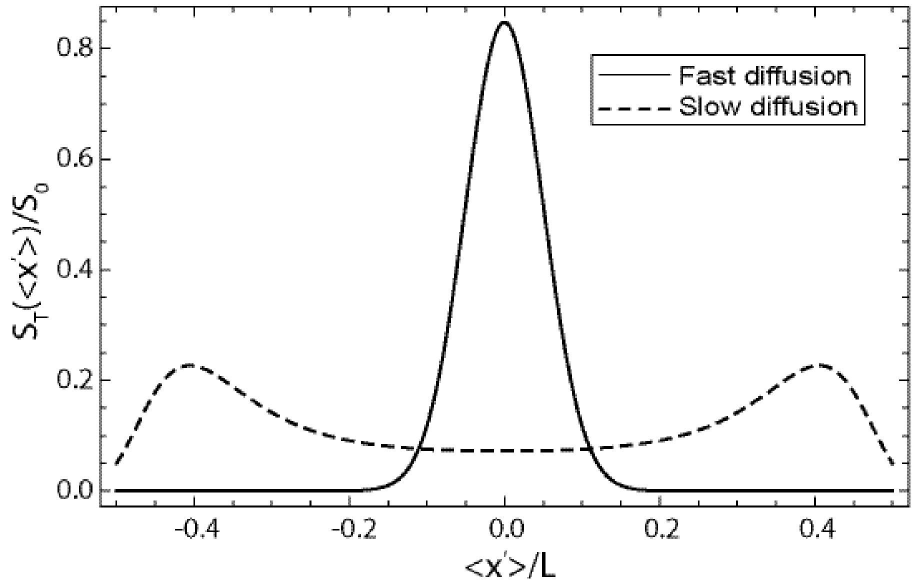

FIGURE 4.6: Frequency spectrum of S_T as a function of $\langle x' \rangle / L$ at $t = 0.02$ s. The length L of the cell is 1 cm. The solid line corresponds to $D = 1000$ cm^2/s, which is in the motional averaging regime, and the dashed line corresponds to $D = 1$ cm^2/s, which is in the slow diffusion limit.

$D = 1$ and 1000 cm^2/s, respectively. The $D = 1$ cm^2/s case is in the slow diffusion limit, and two peaks close to the edges are observed. As diffusion is more restricted at the boundary, the diffusion induced relaxation is suppressed, compared with the relaxation at the center. In contrast, the $D = 1000$ cm^2/s case is in the fast diffusion limit and only one peak centered at the mean frequency presents, which means most of spins precess at the same frequency and relax at the same rate, i.e. Eq. (4.31). These results show that the approach developed in this manuscript is able to capture all distinct behaviors of the transverse magnetization in different diffusion regimes.

In Sec. II B, it is shown that the longitudinal relaxation rate $1/T_1^G$ differs by a factor of 2 between the slow diffusion limit and the fast diffusion high pressure limit. A possible explanation is that when t is small, i.e. in the slow diffusion limit ($4Dt << (L/2)^2$), most of the spins do not see walls so spins diffuse freely; when t gets larger, it gets into the fast diffusion limit ($4Dt >> (L/2)^2$), where spins see the wall frequently. As diffusion is more restricted in the fast diffusion limit, the effective diffusion speed is smaller than that in the free diffusion. As a result, the relaxation rate in the fast diffusion limit is smaller, similar to the explanation of the edge enhancement effect.

We numerically evaluate $\Re[J_x(\omega_0)]$ as a function of time to reveal how $1/T_1^G$ changes from the slow diffusion limit to the fast diffusion limit (Figure 4.7). Values of the parameters used in the evaluation are assigned as $\langle x' \rangle = 0$, $D = 1$ cm^2/s, $L = 1$ cm and $\omega_0 = 1$ to 1000 rad/s. In the figure, the quantity $\omega_0^2\Re[J_x(\omega_0)]$ is actually plotted for the purpose of comparison. Therefore, in the slow diffusion limit, $\omega_0^2\Re[J_x(\omega_0)] = 2D$; whereas, in the fast diffusion high pressure limit, $\omega_0^2\Re[J_x(\omega_0)] = D$. As shown in the figure, when t is small, i.e. in the slow diffusion limit, the relaxation rate oscillates around $2D$. When t becomes larger, the oscillating amplitude of the relaxation rate decreases and the mean of the oscillation converges to the fast diffusion results. The final value of the fast diffusion result depends on the ratio of τ_d/τ_l, see Sec. II B. When $\omega_0 = 1000$, it is in the high pressure limit and $\omega_0^2 J_x(\omega_0)$ converges to D, which is 1 cm^2/s in our case; and when $\omega_0 = 1$ rad/s, it is in the low pressure limit and $\omega_0^2 J_x(\omega_0) = \omega_0^2 L^4/120D = 1/120$ cm^2/s, see Eq. (4.39). The characteristic time to distinguish the slow diffusion limit from the fast diffusion limit is also $\tau_c = (L/2)^2/4D = 0.0625$ s. As τ_c is usually small in practice, T_1^Gs measured by experiments are usually in the fast diffusion limit. Nevertheless, When D is small enough or alternatively the cell dimension is large enough, the characteristic time τ_c can be rather large and it is possible to measure the longitudinal relaxation rate in the slow diffusion regime.

4.2.5 Conclusions

A new approach based on Redfield theory is developed to calculate magnetic field gradient-induced longitudinal and transverse relaxations of ^{3}He gas. As an extension to the method developed by McGregor, the newly developed approach works in all

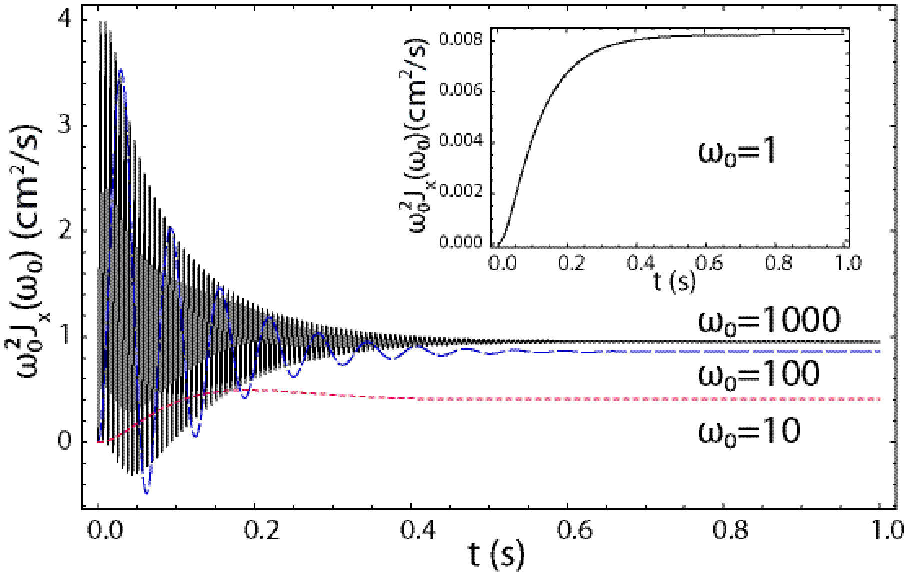

FIGURE 4.7: (Color online)The curve with $\omega_0 = 1000$ rad/s is definitely in the high pressure limit, the normalized relaxation rate evolves into D ($D = 1$ cm^2/sec) as expected. The inset figure shows the relaxation rate when $\omega_0 = 1$ rad/s, which is in the low pressure limit. It evolves into $\omega_0^2 L^4/120D$, which is 1/120 cm^2/s, when t becomes large. The other two curves are in the intermediate region.

diffusion regimes, including the intermediate regime. It can also explain the edge enhancement effect in the slow and intermediate diffusion regime, which shows the ability to capture all the relaxation related behaviors in one single unified model. It also has an advantage in terms of numerical simulations, because one only needs to re-compute the probability density function for new geometries. Since the density function is easy to obtain, the relaxation rates can be computed readily as described in this manuscript.

This work is based on the paper of Zheng *et al* [148].

5

Search for Spin-Dependent Short-Range Force Using Optically Polarized ^{3}He Gas

5.1 Introduction

The possible existence of new forces with weak couplings and macroscopic ranges have been proposed by several authors [90, 68, 9, 76]. A P- and T- violating macroscopic force with an interaction range from cm to μm first proposed in [97] has the form

$$V(z) = \frac{g_s g_p \hbar^2 \hat{\sigma} \cdot \hat{r}}{8\pi m_n} (\frac{1}{r\lambda} + \frac{1}{r^2}) \exp(-r/\lambda), \tag{5.1}$$

where g_s and g_p are the scalar and pseudoscalar coupling constants, $\hbar$ is the Plank's constant, $\hat{\sigma}$ is the spin of the polarized nucleon, $\hat{r} = \vec{r}/r$ is the unit vector from the unpolarized nucleon to the polarized nucleon, m_n is the nucleon mass, and λ is the range of the force. This short-range force is mediated by exchanging an axion-like particle between unpolarized nucleons and polarized nucleons. A similar interaction may also exist between nucleon and electron. Many experimental efforts have been devoted to search for this interaction between either nucleons or nucleon and electron, and various techniques have been used, such as sensitive torsion pendula

[118, 64], clock comparisons between two different polarized species [145, 136, 57], and measurements of neutron bound states on a flat surface in the gravitational field [10]. Very recently, measurements of the longitudinal relaxation rate Γ_1 and transverse relaxation rate Γ_2 of polarized ^{3}He gas were used to search for this short-range interaction between nucleons [109, 129, 49, 108]. As the relaxation time of polarized ^{3}He can be as long as tens of hours, any new interaction with the polarized ^{3}He nuclei can lead to a visible change in the relaxation time. These measurements provide to our knowledge the most stringent direct laboratory constraint on the coupling constant product $g_s g_p$ for a monopole-dipole interaction between nucleons of the form in Eq. (5.1) over distances from 10^{-6} to 10^{-2} m [108]. Note that this limit is still more than 9 orders of magnitude larger than the standard Axion coupling originally proposed to solve the strong CP problem [145, 103].

In this work, we present a new method to search for the spin-dependent macroscopic force between nucleons by measuring the frequency difference of optically polarized ^{3}He gas with and without a nearby unpolarized mass. The frequency difference due to the magnetic field gradient is a first order effect, as such it is more sensitive than the relaxation measurement because the gradient-induced relaxation is a second order effect [130, 29]. We also performed a pilot experiment to demonstrate how this method works. With a modest stability of the magnetic field, the sensitivity of this experiment already reaches the current best laboratory limit on $g_s g_p$. With improved stability of the magnetic field, the proposed method could be used to improve the current best limit by two to three orders of magnitude in the force range from 10^{-4} to 10^{-2} m.

5.2 Experimental Technique

The spin-dependent short-range interaction changes the precession frequency of the polarized nuclei through the interaction $\hat{\sigma} \cdot \hat{r}$ in Eq. (5.1), which is similar to the well-known $\hat{\mu} \cdot \vec{B}$ interaction of a magnetic dipole moment $\hat{\mu}$ in an external magnetic field $\vec{B}$. Consider a cylindrical cell containing polarized ^{3}He gas with its polarization pointing in the z direction along the axis of the cylinder and a block of unpolarized mass is placed next to the end of the cell. The short-range interaction on each ^{3}He atom inside the cell can be obtained by integrating Eq. (5.1) over the unpolarized source mass. In the limit case in which the transverse dimensions (x, y direction) of the mass are much larger than the force range, the mass can be approximated as an infinite plane source with its normal pointing in the z direction. In this limit the frequency shift from the planar mass block is [49]

$$\Delta\omega = \frac{g_s g_p N \hbar \lambda}{4 m_n} e^{-z/\lambda}(1 - e^{-d_0/\lambda}), \tag{5.2}$$

where z is the distance measured from the surface of the mass block to the polarized ^{3}He, N is the nucleon number density of the mass, and d_0 is the thickness of the mass block. If the external magnetic field is uniform with a value of B_0, then the spin precession frequency in the presence of the mass has a spatial dependence which can be written as

$$\omega = \omega_0 + A e^{-z/\lambda}, \tag{5.3}$$

where $A = \frac{g_s g_p N \hbar \lambda}{4 m_n}(1 - e^{-d_0/\lambda})$. As the precession signal received by the pickup coil is a weighted sum from all the ^{3}He inside the cell, the signal induced in the pickup coil is

$$S \propto \int_d^\infty \cos(\omega_0 t + A e^{-z/\lambda} t) B(z) dz, \tag{5.4}$$

where d is the window thickness of the cell, $B(z)$ is the field profile of the pickup coil along the cell axis, and the reciprocity theorem is applied here to compute the signal induced in the pickup coil [71]. When A is zero, Eq. (5.4) is a pure sinusoidal function with a well-defined frequency. When A is nonzero Eq. (5.4) shifts the mean frequency of the signal. The mean oscillation frequency determined from N_c

observed periods during a time T is $f = N_c/T$. In the presence of the interaction for the same number of periods the time duration changes to T' and the new frequency is $f' = N_c/T'$. The frequency difference is [1]

$$\Delta f = \frac{N_c}{T'} - \frac{N_c}{T} \cong -f\frac{\Delta T}{T}, \tag{5.5}$$

where $\Delta T = T' - T$. Eq. (5.5) establishes a relation between Δf and ΔT. ΔT can be calculated for different strengths $g_s g_p$ and ranges λ of the spin-dependent interaction by numerically integrating Eq. (5.4). For any given λ, the parameter A in Eq. (5.4) is tuned in such a way that the calculated ΔT matches the experimentally determined frequency shift Δf. Hence, constraints on $g_s g_p$ with different values of λ are established given the sensitivity of the experiment.

In this pilot experiment we used a 7 amg [2] high pressure ^{3}He cell originally constructed as a ^{3}He gas target for two- and three-body photo-disintegration experiments [144]. The cell had two chambers, a spherically-shaped spin-exchange optical pumping chamber and a 40 cm long cylindrical target chamber connected by a glass tube, Figure 5.1. The target chamber had two thin glass windows on its ends. The thickness of the window was about 250 μm. A Macor machinable ceramic mass block was used as the unpolarized mass. It was repeatedly brought into contact with and moved away from the cell window by a G-10 rod connected to a stepper motor. The stepper motor moved the mass to a final position with better than 10 micron repeatability, more than an order of magnitude smaller than the cell window thickness. Two identical pickup coils were mounted right below each window. Pickup coil A was used to measure the frequency of the polarized ^{3}He nuclei influenced by the mass; pickup coil B was used to monitor the magnetic holding field. The 40 cm

---

[1] When S/N becomes the limiting factor of the measurement (not the case in the present work), phase difference or frequency spectrum may provide a better measurement of the frequency shift than the peak counting method.

[2] 1 amg is the number density of 1 atm gas molecules at 0 °C.

long ^{3}He cell was positioned at the center of a Helmholtz coil pair. Due to fairly large gradients at the end of the cylindrical chamber, two identical two-axis gradient coil pairs (dashed line in Figure 5.1) were added at both ends to compensate the gradients from the Helmholtz coils and background fields. The measured transverse relaxation time T_2 of the ^{3}He signal is greater than 1 s with this arrangement.

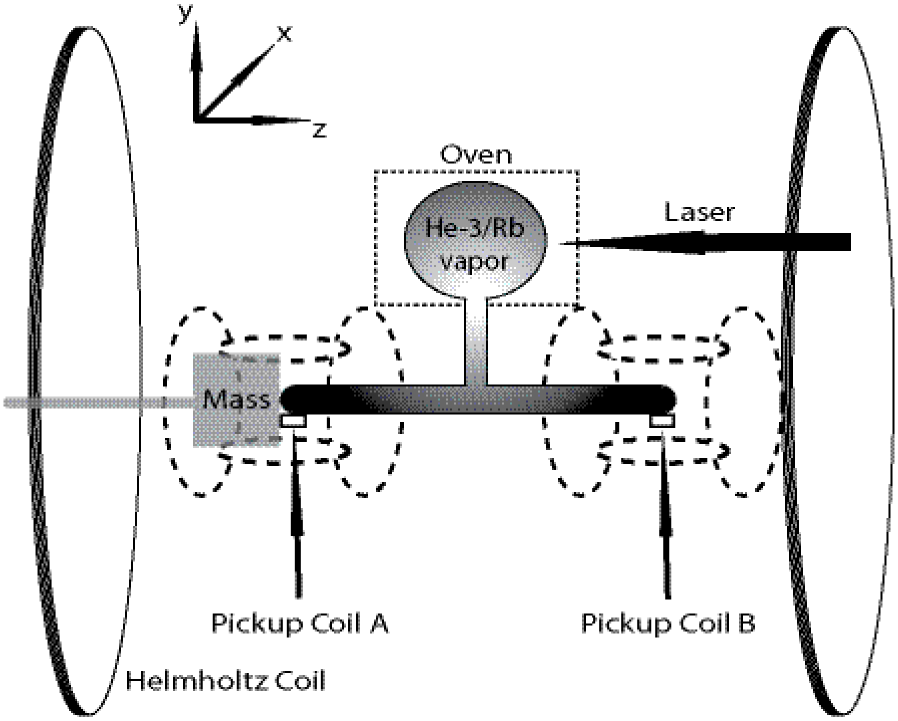

FIGURE 5.1: The diagram of the test experiment apparatus (not to scale). The cylindrical cell axis is the z direction. The cell contains 7 amg ^{3}He gas and is optically pumped in the pumping chamber to about 40% polarization. The coils in the dashed lines are gradient coils to actively compensate the gradients from the Helmholtz coil and other background fields.

Free induction decay (FID) at 24 kHz was performed to measure the ^{3}He precession signal. The RF pulse with small tipping angle was applied to make the polarization loss negligible. The precession signal is digitized and recorded by the computer. In order to determine the frequency unambiguously, the acquisition time stopped at the instant when the signal-to-noise ratio is either below 10 or at 0.2 s, whichever comes first. The frequency is computed by counting the periods during the acquisition time. In a 7 amg ^{3}He gas cell, the diffusion constant is about 0.27 cm^2/s [123], and it is known that the effective diffusion rate is lowered at the cell boundary [133]. Therefore effects from the diffusion of the ^{3}He can be ignored during the FID measurement and it is valid to use Eq. (5.4) to analyze the experimental data. Each measurement cycle contains two measurements: first with the mass in contact with the window (in position) and next with the mass moved far away from the window (out position). Simultaneous measurements at pickup coil B were performed to monitor the magnetic field fluctuations. The peak to peak variation of the field is about $5 \times 10^{-3}\%$. Removing the field fluctuations measured by coil B reduced the peak to peak variation of the field to $4 \times 10^{-4}\%$. After the field correction, the frequency difference between the "in" and "out" positions is calculated as $\Delta f = f_{in} - f_{out}$.

The magnetic susceptibility of the mass can change the field at the location of the ^{3}He through its effect on the holding field and therefore lead to a systematic effect. Although the magnetic susceptibility of Macor ceramic is known to be small enough not to cause a systematic error in this test experiment, the real material can in principle contain paramagnetic or even ferromagnetic impurities. Paramagnetic impurities would increase the local field strength (and therefore the ^{3}He precession frequency) independent of field direction. The spin-dependent interaction can increase or decrease the precession frequency depending on the magnetic holding field direction. We therefore can isolate a possible spin-dependent interaction from paramagnetic effects by flipping the magnetic field. However, a frozen-in field from possible ferromagnetic impurities has the same magnetic field dependence as the spin-dependent interaction, which makes it difficult to separate them apart. The most likely ferromagnetic contamination of the mass block comes from machining process, during which ferromagnetic tools are usually used to cut the material. To minimize this effect, cutting tools with diamond tips are used to ensure that there is no physical contact between the metallic part of the tools and the surface of the block. Additionally, we also flip spin direction in order to cancel any spin-dependent systematic effect in the system if there is any. Therefore, we took data in four different configurations for B field and spin directions, Δf_{++}, Δf_{-+}, Δf_{--}, and Δf_{+-}, representing B/S: ++, B/S: -+, B/S: –, and B/S: +-, respectively. If Δf_B represents the field-dependent frequency shift, Δf_S represents spin-dependent frequency shift, and Δf_0 represents frequency shift without B or S dependence, then

$$\Delta f_{++} = +\Delta f_B + \Delta f_S + \Delta f_0 \tag{5.6}$$

$$\Delta f_{-+} = -\Delta f_B + \Delta f_S + \Delta f_0 \tag{5.7}$$

$$\Delta f_{--} = -\Delta f_B - \Delta f_S + \Delta f_0 \tag{5.8}$$

$$\Delta f_{+-} = +\Delta f_B - \Delta f_S + \Delta f_0. \tag{5.9}$$

In this notation, the short-range force induced Δf_B can be expressed as

$$\Delta f_B = \frac{1}{4}(\Delta f_{++} + \Delta f_{+-} - \Delta f_{--} - \Delta f_{-+}). \tag{5.10}$$

The uncertainty of Δf_B is given by

$$\frac{1}{4}\sqrt{\sigma_{++}^2 + \sigma_{+-}^2 + \sigma_{--}^2 + \sigma_{-+}^2}, \tag{5.11}$$

where σ_{++}, σ_{-+}, σ_{--}, and σ_{+-} are the uncertainties of Δf_{++}, Δf_{-+}, Δf_{--}, and Δf_{+-}, respectively. The noise in the measurement is mainly due to the magnetic field fluctuation, which limits the uncertainties of the frequency measurements.

We performed 100 measurement cycles for each of the four configurations to determine the average frequency difference between the two mass positions. The frequency differences from the spin-dependent force for these runs are shown in Figure 5.2. The average frequency difference of 100 measurements was $\Delta f_B = -0.003 \pm 0.005$ Hz, consistent with zero.

Eq. (5.10) is then used to calculate the frequency difference from the spin-dependent short-range force to place an upper limit on $g_s g_p$ as a function of λ.

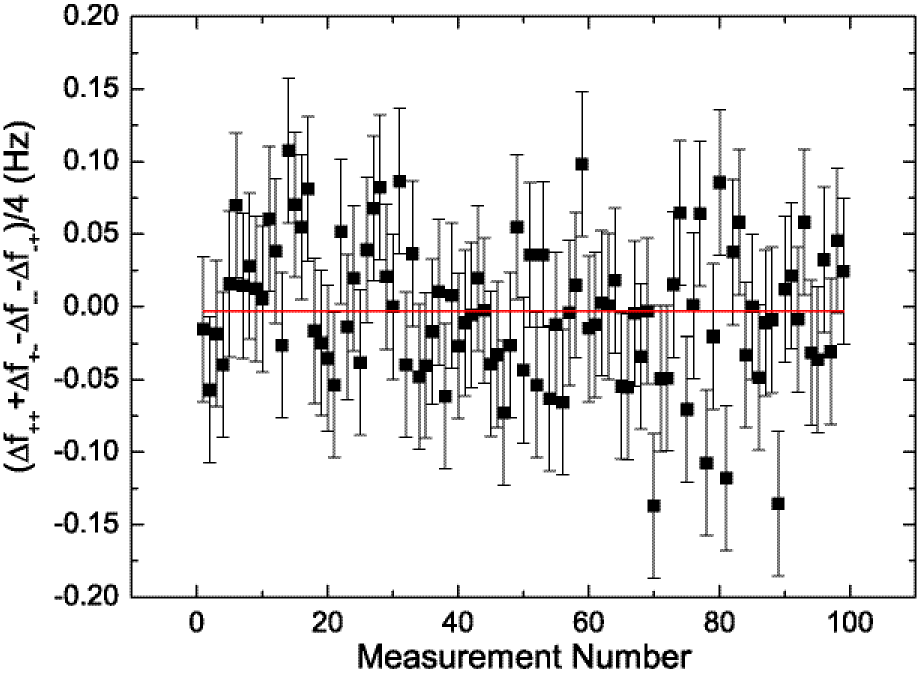

FIGURE 5.2: The frequency difference correlated with the position of the ceramic mass block. The error bars show the standard deviation of the magnetic holding field after correction by coil B.

For $f = 24$ kHz and $\Delta f = 0.005$ Hz, Eq. (5.5) yields $\Delta T = -2.1 \times 10^{-7} T$ s. With a fixed frequency shift, ΔT should increase linearly with respect to the acquisition time T. Theoretically, ΔT is obtained by comparing Eq. (5.4) with a sinusoidal function in absence of the force. With a real pick-coil profile, Eq. (5.4) is obtained by numerical integration, using the actual geometry of the experiment. The resultant ΔT as a function of T is shown in Figure 5.3 (the upper black curve). Surprisingly, ΔT increases linearly only for a short period of time. As time elapses, ΔT oscillates around a constant value, indicating that the frequency shift due to this exponential type of force is not fixed and diminishes at large T. This striking behavior suggests that one will not gain more information from longer measurement time though the frequency resolution is improved by doing so.

An closed-form solution of Eq. (5.4) can be obtained if one approximates the real profile of $B(z)$ by a rectangular function with a cut-off position w mimicking the width of the profile. In this case, the upper limit of the integral is replaced by w, and the integration yields

$$S(t) = \lambda[\cos(\omega_0 t)(\mathrm{Ci}(Ae^{-\frac{d}{\lambda}}t) - \mathrm{Ci}(Ae^{-\frac{w}{\lambda}}t))$$
$$- \sin(\omega_0 t)(\mathrm{Si}(Ae^{-\frac{d}{\lambda}}t) - \mathrm{Si}(Ae^{-\frac{w}{\lambda}}t))], \tag{5.12}$$

where $\mathrm{Ci}(x)$ is Cosine Integral and defined as $\mathrm{Ci}(x) = -\int_x^\infty \frac{\cos t}{t} dt$; $\mathrm{Si}(x)$ is Sine Integral and defined as $\mathrm{Si}(x) = \int_0^x \frac{\sin t}{t} dt$ [3]. One can use Eq. (5.12) to calculate the ΔT in Eq. (5.5). To the first order, ΔT can be expressed as

$$\Delta T = -\frac{\mathrm{Si}(Ae^{-\frac{d}{\lambda}}T) - \mathrm{Si}(Ae^{-\frac{w}{\lambda}}T)}{\mathrm{Ci}(Ae^{-\frac{d}{\lambda}}T) - \mathrm{Ci}(Ae^{-\frac{w}{\lambda}}T)}. \tag{5.13}$$

Using the value of $d = 250$ μm and $w = 5.825$ cm, Eq. (5.13) is plotted in Figure 5.3 (the lower red curve). It is surprising to find that ΔT does not increase linearly with respect to T all the way up. At certain point, ΔT becomes more or less a constant, which means the phase difference due to the short-range force stop accumulating after certain time. A longer measurement time will not increase the phase difference due to the short-range force. This behavior is the result of the inhomogeneous broadening due to the varying distance between the ^{3}He spin and the mass.

This simple approximation yields a satisfactory result in terms of the time at which the linear relationship breaks down (The exact solution is plotted as a black curve in Figure 5.3). In our experiment, the maximum measurement time is less than 0.2 s to guarantee that the FID measurement is in the linear region, so that the frequency comparison is valid even the measurement time for each configuration is slightly different.

5.3 Experimental Results

By choosing different values of λ, the constraints on the coupling constants $g_s g_p$ are found and plotted as a solid line in Figure 5.4. The 250 μm window thickness of the

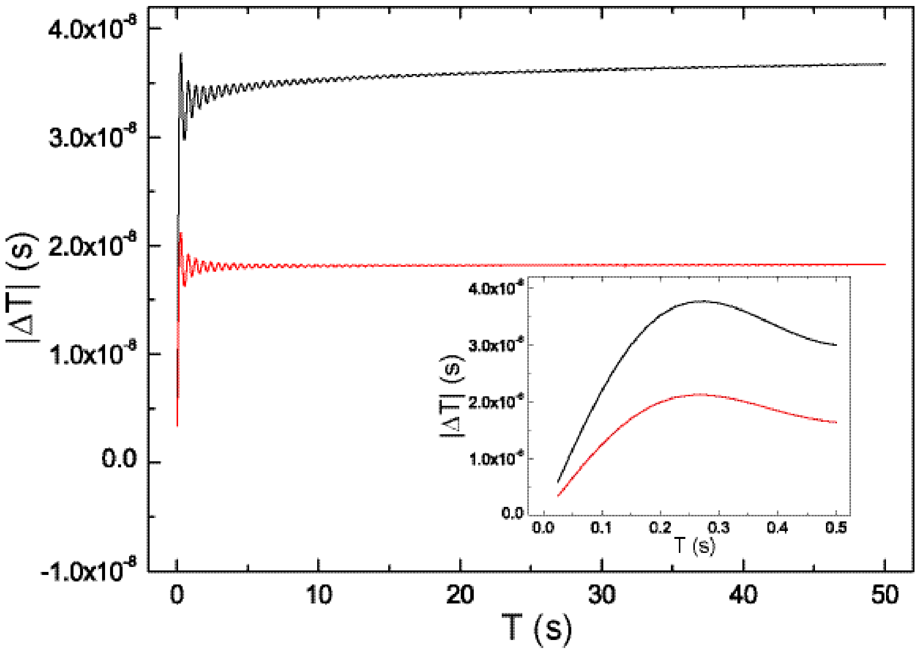

FIGURE 5.3: The upper curve shows the $|\Delta T|$ as a function of T, using the real field profile of the pickup coil. The lower curve shows the same curve but with the pickup coil profile approximated by a rectangular function. The inset of the figure shows the linear behavior of $|\Delta T|$ at small T.

double chamber glass cell allows us to constrain interactions ranges λ down to 10^{-4} m. The dominant source of the uncertainty in our experiment came from magnetic field fluctuations. The gradient compensation coils, needed to achieve an uniform field in our apparatus, added uncorrelated magnetic field noise to the holding field as the gradient coils were powered by independent power supplies.

5.4 Future Outlooks

There are many avenues for the improvement of the measurement sensitivity using this technique. One can use a dedicated ^{3}He cell with a shorter length and add magnetic shielding instead of gradient coils to improve the field uniformity and stability. In [38], the authors conducted a precision frequency measurement using polarized gases in an apparatus with three layers of cylindrical μ metal shielding for field uni-

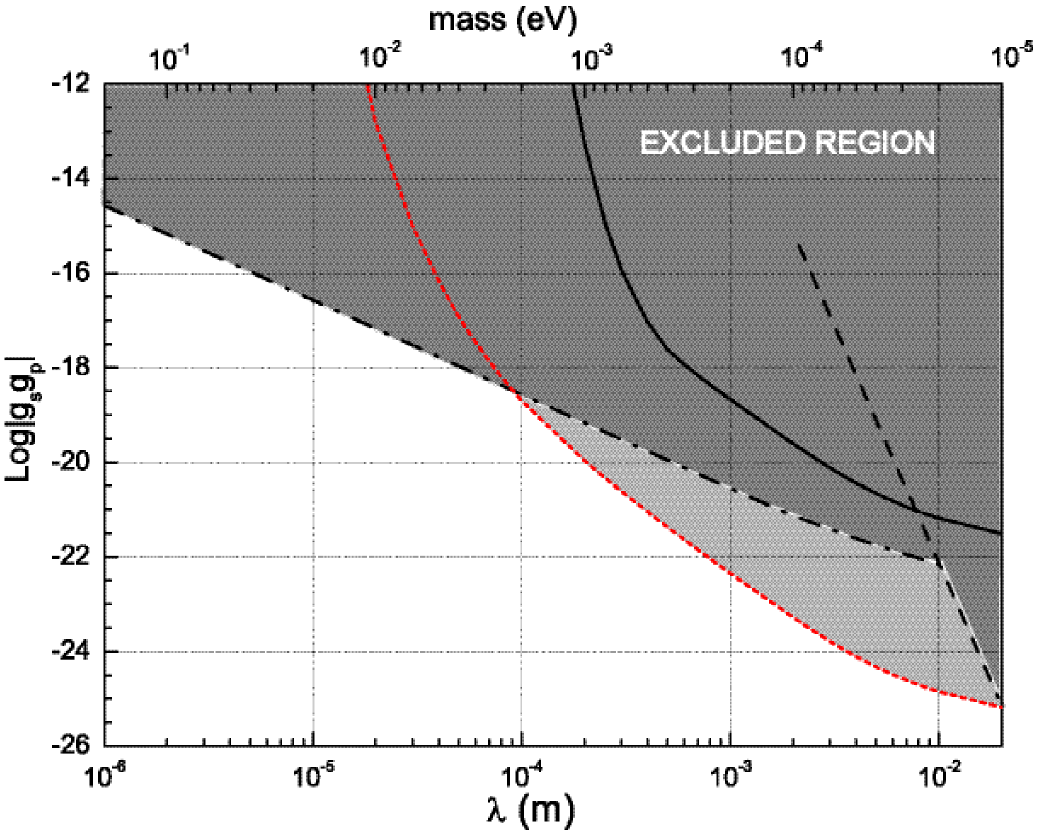

FIGURE 5.4: Constraints on the coupling constant product $g_s g_p$ of the spin-dependent force as a function of the range λ and the equivalent mass of the axion-like particle mediating the short-range interaction. The dashed line is the result from [145], the dash-dotted line is the re-analysis of the T_2 measurements of [55] by [108], the solid line is the analysis of our present experiment, and the dotted line is a projected sensitivity achievable using our method based on the stability of the magnetic field demonstrated in [38]. The dark gray is the excluded region and the light gray is the region that could be excluded with the improved field stability.

formity and a co-magnetometer technique to reduce the magnetic field noise by 3 to 4 orders of magnitude. They achieved a precision of 10^{-6} Hz out of 1000 Hz, two orders of magnitude better than our pilot experiment. In Figure 5.4 we show the limits on $g_s g_p$ (dotted line) which could be achieved with this technique using the sensitivity demonstrated in [38] assuming all other geometric parameters (window thickness, pickup coil size, etc.) are unchanged. As shown in Fig 5.4, this projected sensitivity would represent a significant improvement in the λ region of 10^{-2} to 10^{-4}

m, compared with the best existing laboratory limit derived by the authors of [108], shown as the dotted-dashed line, based on the results of a T_2 measurement from [55].

The sensitivity of the experiment below $\lambda = 10^{-4}$ m is clearly limited as the thickness of the window becomes much larger than the force range. The 7 amg ^{3}He cell has an internal pressure of more than 10 atm at 200 °C and the 250 μm window thickness is needed for strength. However, the high pressure is not necessary for this experiment. A 1 amg ^{3}He cell with reduced window thickness could be used to improve the sensitivity of the measurement, especially in the $\lambda < 10^{-4}$ m range. Another order of magnitude improvement on the sensitivity could be achieved if denser material was used as the unpolarized mass, such as pure copper or tungsten. We conclude that our proposed method shows a promising sensitivity, with at least one to two orders of magnitude improvement over the current best limit possible in a dedicated experiment with better magnetic field stability. A even higher sensitivity could be achieved if a thinner wall for the ^{3}He cell and denser material is used.

This chapter is mainly based on the the work of Zheng *et al* [147].

6

Conclusion and Future Outlook

The newly proposed nEDM experiment at Oak Ridge National Lab can improve the sensitivity of the neutron EDM by two orders of magnitude. It utilizes the polarized ^{3}He as a co-magnetometer to suppress the magnetic field fluctuation. The spin-dependent reaction between polarized ^{3}He and neutron is also used to obtain the precession frequency of the neutron. To reach the proposed sensitivity, it requires that the polarization of ^{3}He in the measurement cell should be at least 95%. This requires a very careful design of the apparatus and magnet so that the polarization of ^{3}He is maintained throughout the entire injection process. My Monte-Carlo simulation suggests that a 95% polarization of ^{3}He is possible to achieve as long as the transport field is well designed.

In addition to the polarization issue, the nEDM experiment also faces the challenge of measuring small ^{3}He signals due to low number density 5×10^{14} atoms/cc. The SQUID test setup was built to demonstrate the feasibility of measuring the small ^{3}He precession signal with SQUID in the nEDM experiment. Our test result shows that a signal to noise ratio of at least 10 could be achieved under the real nEDM experimental conditions.

During the SQUID test, I discovered a pressure dependence in the ^{3}He wall relaxation. This pressure dependence was observed at both low temperature and room temperature. After a dedicated study, I ascribe this pressure dependence to the diffusion process of the gaseous ^{3}He. A model was also proposed to quantitatively describe this behavior, which agrees with the experimental data very well.

I also developed an approach to calculate the magnetic field gradient-induced T_1 and T_2 relaxations of ^{3}He. This new approach yields a general solution which is capable of giving correct solutions in different diffusion regimes. All these studies are important to the nEDM experiment as well as to the polarized ^{3}He community because T_1 and T_2 are two of the most important parameters of polarized ^{3}He. The proposed measurement time of the nEDM experiment crucially depends on the values of T_1 and T_2, which plays an important role in determining the sensitivity of the nEDM experiment.

We use the high pressure ^{3}He cell to search for the short-range spin-dependent force. Thanks to the extremely thin window of the cell (250 μm) as well as the experimental procedures to cancel out the systematic effect, the sensitivity in our current setup is already in line with the current best limit. With further improvement on the apparatus, we are able to increase the sensitivity by two orders of magnitude over the current best limit.

The future work on the short-range force experiment involves manufacturing a new ^{3}He cell, a new liquid mass moving system, and installing a magnetic shielding. The smaller ^{3}He cell can improve the correlation between two measurement channels so that the field compensation scheme works better. The new cell can be filled with less ^{3}He gas so that the window thickness can be reduced further. The liquid mass instead of solid can maximize the interaction by minimizing the distance between the polarized ^{3}He and the mass. The magnetic field shielding can improve the field uniformity and stability. This increases the coherent measurement time, which helps determine the precession frequency more accurately.

Currently, there is a debate on how to interpret the pressure dependence observed in the ^{3}He paramagnetic wall relaxation. More experimental work and theoretical calculation are needed to clear up the confusion and end the debate.

Appendix A

Spin Exchange Optical Pumping

We polarize ^{3}He nuclei through spin-exchange optical pumping (SEOP). Firstly, the Rubidium vapor is polarized by optical pumping. Then, the polarized Rb transfer its polarization to ^{3}He nuclei by spin-exchange. Rubidium atom has one unpaired valence electron in its 5s shell. This electron can be excited to the $5P_{1/2}$ state from its ground state $5S_{1/2}$, also known as D_1 transition, by a photon. The wavelength of the photon is tuned to 794.8 nm, which is the energy gap between this $5S_{1/2} \rightarrow 5P_{1/2}$ transition [43, 21]. Following the selection rule $\Delta m = \pm 1$, only the electrons in $5S_{1/2}, m_S = -1/2$ state can jump into the $5P_{1/2}, m_S = 1/2$ state if the photon is circularly polarized in the positive direction. Once the electron is in the excited state $5P_{1/2}, m_s = 1/2$, some of the electrons can jump to the $5P_{1/2}, m_S = -1/2$ state due to collisions between Rb atoms. This process is also known as collisional mixing. Then, electrons in these two excited states will spontaneously decay back to the two ground states $5S_{1/2}, m_S = 1/2$ and $5S_{1/2}, m_S = -1/2$, see Figure A.1. Because of the collision, the excited electron decays back to the two ground states with equal probabilities. By optically pumping the Rb continuously, the net effect is that the electrons in the $5S_{1/2}, m_S = -1/2$ state are pumped to the $5S_{1/2}, m_S = 1/2$ state, and the polarization of Rb is close to 100%. The spontaneous decay also emits photons. These emitting photons are also polarized but in the opposite direction and can therefore depolarized the already polarized Rb atoms. To avoid this, Nitrogen gas is introduced to absorb the emitting photons, so that the angular momentum of the emitting photon is transfered to the neutron as rotational and vibrational energies. This technique is also known as non-radiative quenching [5].

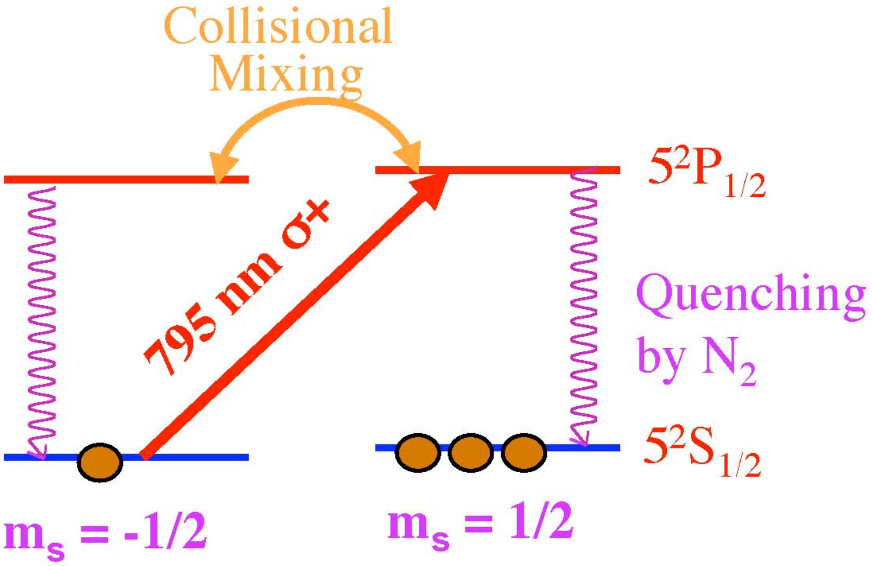

FIGURE A.1: Optical pumping of the valence electron in Rb atom.

The Rb can also transfer the spin of its electron to the nucleus of ^{3}He by binary collisions. During the collision, the spin is exchanged because of the hyperfine interaction between the ^{3}He nuclues and the electron in the Rb. Since Rb is polarized by the optical pumping, the polarization of the Rb will be transferred to the polarization of ^{3}He. When reaching an equilibrium, ^{3}He polarization is expressed as

$$P_{^3He} = P_{Rb} \frac{\gamma_{SE}}{\gamma_{SE} + \Gamma}, \tag{A.1}$$

where P_{Rb} is the polarization of Rb electron which is usually 1. γ_{SE} is the spin exchange rate between Rb and ^{3}He, and Γ is the total ^{3}He spin destruction rate.

The spin exchange rate is about 3% for every binary collision between Rb and ^{3}He and it usually takes about 12 hours for the spherical detachable cells used in Chapter 4 to reach maximum polarization. A variation to the Rb-^{3}He spin-exchange is the Rb-K-^{3}He spin-exchange. The Pottasium (K) atoms are introduced because the spin-exchange rate between K and ^{3}He is much bigger than the spin exchange rate between Rb and ^{3}He [144]. Therefore, by transfering the polarization from Rb to K and then from K to ^{3}He, a higher polarization of ^{3}He as well as a shorter pumping time can be achieved. For example, the pumping time in our high pressure ^{3}He cells (7 amagat ^{3}He) is reduced by roughly 50%. This cell has been used in the spin-dependent force experiment in Chapter 5.

In practice, the ^{3}He cell was filled with Rb/K metal. As the SEOP only takes place with Rb/K vapor, the cell is heated up to 190 °C or above using hot air flow to vaporize the Rb/K. The pressure of ^{3}He inside the cell usually ranges from 1 atm to 8 atm because spin exchange is efficient only at high pressures. The amount of N_2 added to the system is typically around 0.1 atm or one order of magnitude less than the ^{3}He density. The polarization of the ^{3}He in our lab can routinely reach more than 60%.

Appendix B

Simplification of the Position Autocorrelation Function in the Slow Diffusion Limit

In the slow diffusion limit, $4Dt << (L/2)^2$, Eq. (4.23) is simplified by expanding all exponential terms in terms of t, t_0 and τ to the first order. Trigonometric functions, such as $\sin(\frac{n\pi\langle x'\rangle}{L})$, can be expanded in terms of $\frac{\langle x'\rangle}{L}$ to the first order. The first term of Eq. (4.23) becomes

$$\frac{8L^2}{\pi^4}\sum_{n=1,3}^{\infty}\frac{1}{n^4}(1-\frac{n^2\pi^2 D\tau}{L^2}) = \frac{L^2}{12} - D\tau. \tag{B.1}$$

The second term $\langle x'\rangle^2$ is unchanged, and the third term becomes

$$\frac{4\langle x'\rangle L}{\pi^2}\sum_{n=1,3}^{\infty}\frac{1}{n^2}\sin(\frac{n\pi}{2})\frac{n\pi\langle x'\rangle}{L}(1-\frac{n^2\pi^2 Dt}{L^2})$$

$$= \frac{4\langle x'\rangle^2}{\pi}\sum_{n=1,3}^{\infty}\frac{\sin(\frac{n\pi}{2})}{n} + O(1/L) = \langle x'\rangle^2. \tag{B.2}$$

The fourth term is the same as the third term, which is also $\langle x'\rangle^2$; and the last term becomes

$$\frac{16L^2}{\pi^4}\sum_{n=1,3}^{\infty}\sum_{k=2,4}^{\infty}\frac{k^2+n^2}{n^2(k^2-n^2)^2}\cos(\frac{k\pi}{2})$$

$$\times(1-\frac{n^2\pi^2 D\tau}{L^2}-\frac{k^2\pi^2 Dt_0}{L^2}-\frac{k^2\pi^2\langle x'\rangle^2}{2L^2}). \tag{B.3}$$

The first term in the bracket of Eq. (B.3) is evaluated to converge to $-L^2/12$. The evaluation of the second term yields $D\tau$. The third term and fourth term are the same, except for different prefactors. They are evaluated to be $2Dt_0$ and $\langle x'\rangle^2$, respectively. Collecting all these terms together, the autocorrelation function of x becomes

$$\begin{aligned}
&\overline{(x(t-\tau)-\langle x'\rangle)(x(t)-\langle x'\rangle)}\\
&=\underbrace{\frac{L^2}{12}-D\tau}_{1st\ term}\underbrace{+\langle x'\rangle^2}_{2nd\ term}\underbrace{-\langle x'\rangle^2-\langle x'\rangle^2}_{3rd\ and\ 4th\ term}\\
&\underbrace{-\frac{L^2}{12}+D\tau+2Dt_0+\langle x'\rangle^2}_{5th\ term}+O(1/L)+O(t^2)\\
&=2D(t-\tau).
\end{aligned} \tag{B.4}$$

An alternative way to obtain Eq. (B.4) is to solve the diffusion equation in free space as slow diffusion is equivalent to free diffusion. In this case, the conditional probability function $\rho(x,t|x_0,t_0)$ is known to be

$$\rho(x,t|x_0,t_0)=\frac{1}{\sqrt{4\pi D\tau}}e^{-\frac{(x-x_0)^2}{4D\tau}}. \tag{B.5}$$

In the free diffusion, the diffusion equation as well as the autocorrelation is translational invariant. Therefore, $\overline{(x(t-\tau)-\langle x'\rangle)(x(t)-\langle x'\rangle)}=\overline{x(t-\tau)x(t)}$ and

$$\overline{x(t-\tau)x(t)}=\int_{-\infty}^{\infty}dx_0\frac{x_0 e^{-\frac{x_0^2}{4Dt_0}}}{\sqrt{4\pi Dt_0}}\int_{-\infty}^{\infty}\frac{xe^{-\frac{(x-x_0)^2}{4D\tau}}}{\sqrt{4\pi D\tau}}dx=2D(t-\tau), \tag{B.6}$$

which is exactly the same as Eq. (B.4).

Appendix C

Reply to the Comment By Saam et al on Pressure Dependence of Wall Relaxation in Polarized ^{3}He Gaseous Cells

The comment by Saam *et al* [122] proposed an alternative way to specify the boundary condition to describe the surface paramagnetic relaxation. In their formula, the macroscopic magnetic flux due to the diffusion at the wall is set equal to the number of collisions per second times the depolarization probability μ,

$$D\frac{\partial\rho(r,t)}{\partial r}|_{r=R} = -\frac{v}{4}\mu\rho(r,t). \tag{C.1}$$

Using this boundary condition, the paramagnetic wall relaxation becomes pressure dependent only when the surface is sufficiently dirty so that ^{3}He spins are completely depolarized once they hit the wall. Based on their derivation, they argue that the pressure dependence observed in the room temperature T_1 measurement in [149] can be solely ascribed to the o-ring valve used in the Rb-coated cells. As the valve has a very large depolarization probability, the depolarization of ^{3}He spins at other parts of the cell can be ignored. Based on this assumption, i.e. $\mu = 1$ on the valve, and using the geometry of the Rb-coated cell, they use a simplified formula in [73] to estimate $\mathrm{T}_1 = 1.2$ h at $D = 12$ cm^2/s, close to the measured value which is 2 h.

Their boundary condition is correct because it used the Fick's law to relate the macroscopic diffusion with the microscopic flux of the particles with average velocity $\bar{v}$. To further verify the interpretation using their boundary condition, we carry out a finite element analysis (FEA) to calculate T_1 at different pressures to check whether their boundary condition and assumption can describe the experimental result. In this study, we use the exact geometry of the Rb-coated cell in [149] and assume that the depolarization only happens on the valve. Using the boundary condition Eq. (C.1) proposed by Saam *et al*, we calculated T_1 with 4 different values of $v\mu/4$ from 1×10^{-3} m/s to 3×10^{-1} m/s. Since the mean velocity of ^{3}He at room temperature is about 1500 m/s, this corresponds to the depolarization probability μ from 2.7×10^{-6} to 8×10^{-4}. The FEA calculations and the experimental data are shown in Fig. C.1.

Contrary to the claim of the comment by Saam *et al*, the calculation using their boundary condition shows a linear pressure dependence at high pressure regardless of the magnitude of the depolarization probability. When pressure is low, T_1 with small depolarization probabilities tends to be a constant independent of the pressure. This is completely opposite to the observation in the experiment, where the linear pressure dependence is observed at low pressures. With a larger depolarization probability on the valve, the linear pressure dependence tends to extend more to the low pressure region. However, the predicted T_1 in this case will be too small, compared to the experimental values.

In reality, it can be more complicated than the assumption that the depolarization takes place only at the valve. For example, it is possible to have some magnetic impurities or a small area with very dirty surface in the capillary tube, which de-

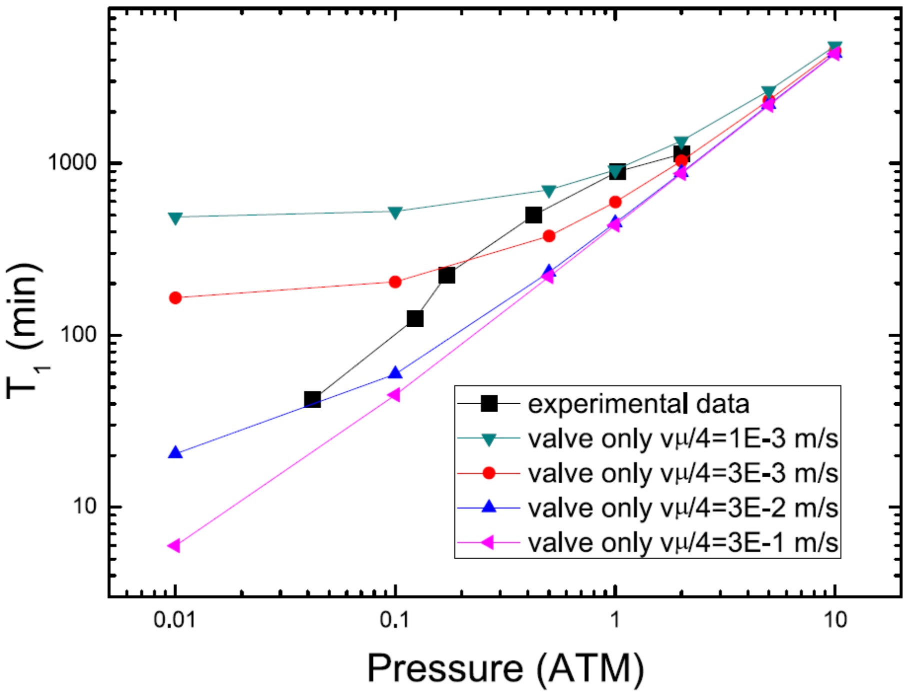

FIGURE C.1: The simulation uses the actual geometry of the Rb-coated cell and assume that the depolarization only takes place at the valve. Four simulations with different depolarization probabilities are plotted. None of them shows the behavior observed in the experiment.

polarizes the gas. However, no matter what actually causes the depolarization in the experiment, the relationship between T_1 and the pressure demonstrated in the FEA calculation should always hold, i.e. the T_1 is more or less a constant at low pressure and the linear pressure dependence is only evident at high pressures. This is inconsistent with the experimental observation and needs to be resolved.

Regarding to the low temperature data, the comment by Saam *et al* also carried out a FEA study with the assumption that the depolarization takes place in the tube which has surface impurities. However, it is unreasonable to assume that the tube has a much worse surface than the cell does since the tube and cell are actually one complete glass piece and cleaning procedures were equally applied to both of them. Therefore, the assumption that the depolarization is completely due to the impurities on the surface of the tube is highly unlikely. Even it is indeed the magnetic impurities in the tube that depolarize the ^{3}He gas, it still cannot explain why the pressure dependence is also observed after the cell and tube are coated with Cs, since their boundary condition would predict no pressure dependence when the surface is clean.

Another controversy between [149] and the comment by Saam *et al* is the explanation of the flattening behavior at high pressures for the Rb-coated cells. In [149], this behavior is explained by the ferromagnetic relaxation, whereas in the comment by Saam *et al*, it is taken for granted that the wall relaxation with clean surface will not exhibit any pressure dependence. To investigate this problem, we have measured a third Rb-coated cell at room temperature. This cell has the same geometry and was produced in the same batch with the other two Rb-coated cells, following the same procedures. The only difference concerning the third cell is that it was accidentally exposed to air for a very short period of time (< 1 s) and the T_1 of this cell was reduced because of this exposure. Other than this, this cell is similar to the other cells, including no previous exposures to high magnetic fields.

When T_1 measurement is performed on this cell at low pressures, it shows a pressure dependence similar to the pressure dependence observed in [149]. At high pressures, in contrast, an inverse pressure dependence is observed, see Fig. C.2. Since the inverse pressure dependence is unique to the ferromagnetic relaxation, this can be surely explained by the ferromagnetic wall relaxations. This supports the argument in the original paper that the flattening behavior at the high pressure is due to the ferromagnetic relaxation even though none of the cells has been magnetized before. Therefore, we may conclude that the absence of exposure to high fields does not guarantee the non-existence of the ferromagnetic relaxation. It only means that the ferromagnetic relaxation is weak and negligible at low pressures, and it can become increasingly evident at higher pressures.

Other possible candidates from the comment by Saam *et al*, such as inhomoge-

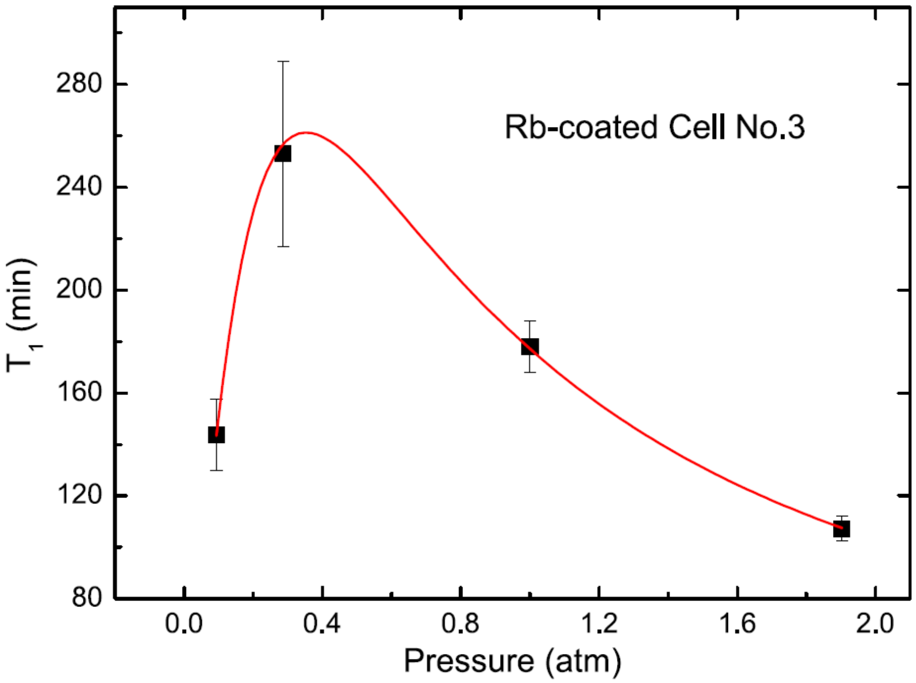

Figure C.2: A third Rb-coated cell. This cell has shorter T_1 in general. T_1 increases with increasing pressure at low pressure region, and peaks around 0.4 atm. Beyond 0.4 atm, an inverse linear pressure dependence is observed. The red curve in the figure is the fit using Eq. 2 in [149].

neous ac field, to explain the linear pressure dependence, can be safely ruled out. To reach the relaxation rate measured in the experiment, the magnitude of this ac field needs to be so strong that the SQUID sensor cannot survive in this environment [30]. It is true that the pressure dependence of the paramagnetic wall relaxation has neither been reported nor systematically studied before. The sealed cells can yield very long T_1 with either low pressures or high pressures. However, it is difficult to be quantitative to compare one sealed cell with another at different pressures, since different cells definitely have different surface conditions. The re-fillable cells used in our study, instead, provide an excellent way to evaluate the relationship between the wall relaxation and pressure, and the similar T_1 has always been observed no matter how many time the cell is re-filled. The linear pressure dependence has also been consistently observed in our measurements with different geometries and experimental conditions. We admit that the coefficient α used in Eq. (5) in [149] is not the depolarization probability, but rather a coefficient characterizing the surface condition which implicitly depends on the depolarization probability. The boundary condition proposed by Saam *et al* should be the correct one to use.

On the other hand, we observed a strong linear pressure dependence of the paramagnetic wall relaxation using the re-fillable cells at both room temperature and 4.2 K. Similar pressure dependence was also observed in references [31, 91, 32]. However, they either attribute the pressure dependence to the pressure dependence of the depolarization probability [31] or just presented the result without any explanation [91, 32]. Using the boundary condition proposed by Saam *et al*, we did a FEA simulation of our room temperature experiment. The simulation does not agree with the room temperature data in terms of the overall behavior of the T_1-pressure relationship. Their boundary condition cannot describe the low temperature data either, unless some unrealistic assumptions were made.

All these evidences point to the fact that a gap exists between the theory and the experimental observation. Though the boundary condition proposed by Saam *et al* is correct, it still cannot describe the experimental data. Therefore, the observed pressure dependent T_1 remains an open question, and some unknown issues need to be identified in order to solve the discrepancy. All in all, this linear pressure dependence is interesting and apparently nontrivial. It is worthy of further investigation.

Bibliography

[1] *Polarized ^{3}He cell development and application at NIST, JCNS Proceedings in press.*, 2011.

[2] K. Abe and et al. http://arxiv.org/abs/hep-ex/0202027, 2002.

[3] M. Abramowitz and I. Stegun. *Handbook of Mathematical Functions with Formulas, Graphs, and Mathematical Tables, 9th printing.* New York: Dover, 1972.

[4] C. Amsler and et al. Review of particle physics. *Physics Letters B*, 667:1 – 6, 2008.

[5] S. Appelt and et al. *Phys. Rev. A*, 58:1412, 1998.

[6] G. Arfken. *Mathematical Methods for Physicists, 3rd ed.* Academic Press, 1985.

[7] B. Aubert and et al. http://arxiv.org/abs/hep-ex/0203007, 2002.

[8] S. Axelrod and P. Sen. *J Chem. Phys.*, 114:6878, 2001.

[9] I. M. B. A. Dobrescu. Jhep0611, 5, (2006). arXiv:hep-ph/0605342v1.

[10] S. Baessler and et al. *Phys. Rev. D*, 75:075006, 2007.

[11] C. Baker and et al. *Phys. Rev. Lett.*, 97:131801, 2006.

[12] S. Balascuta. Monte carlo calculations of the spin transport of polarized 3he from the exit of the abs magnet to the helium injection cell in the upper cryostat. Technical report, May 2010.

[13] V. Baluni. *Phys. Rev. D*, 19:2227, 1979.

[14] R. Barbieri and et al. *Phys. Lett. B*, 369:283, 1996.

[15] M. S. Barr and A. Zee. *Phys. Rev. Lett.*, 65:21, 1990.

[16] S. Barr. *Int. Journal Mod. Phys. A*, 8:209, 1993.

[17] D. Barsky, B. Putz, K. Schulten, J. Schoeniger, E. Hsu, and S. Blackband. *Chem. Phys. Lett.*, 200:88, 1992.

[18] G. Beall and N. G. Deshpande. *Phys. Lett. B*, 132:427, 1983.

[19] A. A. Belavin and et al. *Physics Letters B*, 59:85, 1975.

[20] J. S. Bell. Time reversal in field theory. *Royal Society of London. Series A, Mathematical and Physical Sciences*, 231:479, 1955.

[21] R. Benumof. *Am. J. Phys.*, 33:151, 1965.

[22] I. I. Bigi and A. I. Sanda. *CP Violation.* Cambridge University Press, 2000.

[23] I. I. Bigi and N. G. Uraltsev. *Nucl. Phys. B*, 353:321, 1991.

[24] C. P. Burgess and G. D. Moore. *The Standard Model: A Primer.* Cambridge University Press, 2007.

[25] W. M. Burton and B. Powell. *Appl. Opt.*, 12:87, 1973.

[26] P. Callaghan. *Principles of Nuclear Magnetic Resonance Microscopy.* Oxford University Press Inc., New York, 1993.

[27] P. Callaghan, A. Coy, L. Forde, and C. Rofe. *J Magn. Res.*, A101:347, 1993.

[28] C. G. Callan and et al. *Physics Letters B*, 63:334, 1976.

[29] G. Cates, S. Schaefer, and W. Happer. *Phys. Rev. A*, 37:2877, 1988.

[30] W. D. C. T. S. S. Cates, G. and W. Happer. *Phys. Rev.*, A38:5092, 1988.

[31] R. Chapman and M. Richards. *Phys. Rev. Lett.*, 33:18, 1974.

[32] H. Chen and et al. *Phys. Rev. A*, 81:033422, 2010.

[33] E. Cheng, M. W. Cole, W. Saam, and J. Treiner. *Phys. Rev. Lett.*, 67:1007, 1991.

[34] H.-Y. Cheng. The strong cp problem revisited. *Physics Reports*, 158:1, 1988.

[35] B. Cheron, H. Gilles, J. Hamel, M. Leduc, O. Moreau, and E. Noël. *J. Phys. III France*, 5:1287, 1995.

[36] J. H. Christenson, J. W. Cronin, V. L. Fitch, and R. Turlay. Evidence for the 2π decay of the k_2^0 meson. *Phys. Rev. Lett.*, 13:138–140, Jul 1964.

[37] P. Chu. *NEUTRON ELECTRIC DIPOLE MOMENT AND DRESSED SPIN.* PhD thesis, UIUC, 2011.

[38] T. Chupp and et al. *Phys. Rev. A*, 38:3998, 1988.

[39] T. Chupp, R. Loveman, A. Thompson, A. Bernstein, and D. Tieger. *Phys. Rev. C*, 45:915, 1992.

[40] J. Clarke and A. Braginski. *The SQUID Handbook, Vol I.* WILEY-VCH, 2004.

[41] F. Colegrove, L. Schearer, and G. Walters. *Phys. Rev.*, 132:2561, 1963.

[42] R. J. Crewther and et al. *Phys. Lett.*, 88B:123, 1979.

[43] R. L. de Zafra. *Am. J. Phys.*, 28:648, 1960.

[44] A. Deninger, W. Heil, E. Otten, M. Wolf, R. Kremer, and A. Simon. *Eur. Phys. J. D*, 38:439, 2006.

[45] S. Dimopoulos and L. J. Hall. *Phys. Lett. B*, 344:185, 1996.

[46] W. B. Dress and et al. *Phys. Rev. D*, 15(1):9, 1977.

[47] G. R. Farrar. *Phys. Rev. D*, 50:774, 1994.

[48] J. I. Friedman and V. L. Telegdi. Nuclear emulsion evidence for parity non-conservation in the decay chain $\pi^+ - \mu^+ - e^+$. *Phys. Rev.*, 105:1681–1682, Mar 1957.

[49] C. Fu and et al. *Phys. Rev. D*, 83:031504(R), 2011.

[50] M. Garrett. *J Appl. Phys.*, 38:2563, 1967.

[51] R. L. Garwin and L. M. Lederman. *Nuovo Cim.*, 11:776, 1959.

[52] R. L. Garwin, L. M. Lederman, and M. Weinrich. Observations of the failure of conservation of parity and charge conjugation in meson decays: the magnetic moment of the free muon. *Phys. Rev.*, 105:1415–1417, Feb 1957.

[53] M. B. Gavela and et al. *Phys. Lett. B*, 109:215, 1982.

[54] M. B. Gavela and et al. *Nucl. Phys. B*, 430:382, 1994.

[55] C. Gemmel and et al. *Eur. Phys. J. D*, 57:303, 2010.

[56] J. Gerhold. *Cryogenics*, 12:370, 1972.

[57] A. Glenday and et al. *Phys. Rev. Lett.*, 101:261801, 2008.

[58] R. Golub and J. M. Pendlebury. *Phys. Lett. A*, 53:133, 1975.

[59] R. Golub, D. J. Richardson, and S. K. Lamoreaux. *Ultra-Cold Neutrons.* Adam Hilger, Bristol, 1991.

[60] R. Golub, R. M. Rohm, and C. Swank. *Phys. Rev. A*, 83:023402, 2011.

[61] D. Grebenkov. *Rev. Mod. Phys.*, 79:1077, 2007.

[62] J. Gunion and D. Wyler. *Phys. Lett. B*, 248:170, 1990.

[63] F. Halzen and A. D. Martin. *QUARKS AND LEPTONS: An Introductory Course in Modern Particle Physics*. John Wiley & Sons, Inc., 1984.

[64] G. Hammond and et al. *Phys. Rev. Lett.*, 98:081101, 2007.

[65] W. W. Havens and et al. *Phys. Rev.*, 72:634, 1947.

[66] M. Hayden, G. Archibald, K. Gilbert, and C. Lei. *J. Magn. Res.*, 169:313, 2004.

[67] W. Heil, H. Humblot, E. Otten, M. Schafer, R. Sarkau, and M. Leduc. Very long nuclear relaxation times of spin polarized helium 3 in metal coated cells. *Physics Letters A*, 201(4):337 – 343, 1995.

[68] C. Hill and G. G. Ross. *Nucl. Phys. B*, 311:253, 1988.

[69] M. Hurlimann, K. Helmer, T. D. Swiet, P. Sen, and C. Sotak. *J Magn. Res.*, A113:260, 1995.

[70] W. Hyslop and P. Lauterbu. *J Magn. Res.*, 94:501, 1991.

[71] E. Insko and et al. *J Magn. Res.*, 131:111, 1998.

[72] R. Jackiw and C. Rebbi. *Phys. Rev. Lett.*, 37(3):172–175, 1976.

[73] M. S. Jacob, R. and B. Saam. *J. Appl. Phys.*, 92:1588, 2002.

[74] R. Jacob and et al. *Phys. Rev. A*, 69:021401, 2004.

[75] R. Jacob, S. Morgan, B. Saam, and J. Leawoods. *Phys. Rev. Lett.*, 87:143004, 2001.

[76] J. Jaeckel and A. Ringwald. *Annu. Rev. Nucl. Part. Sci.*, 60:405, 2010.

[77] B. Josephson. Possible new effects in superconductive tunnelling. *Physics Letters*, 1(7):251 – 253, 1962.

[78] A. Kalafala. A design approach for actively shielded magnetic-resonance-imaging magnets. *IEEE Transactions on Magnetics*, 26:1181–1188, 1990.

[79] C. Keith, Z. Chowdhuri, D. Rich, W. Snow, J. Bowman, S. Penttila, D. Smith, M. Leuschner, V. Pomeroy, G. Jones, and E. Sharapov. Neutron cross sections for he-3 at epithermal energies. *PHYSICAL REVIEW C*, 69(3), MAR 2004.

[80] W.-Y. Keung, D. Chang, and T. C. Yuan. *Phys. Lett. B*, 251:608, 1990.

[81] I. B. Khriplovich and et al. *Phys. Lett. B*, 383:429, 1996.

[82] I. B. Khriplovich and S. K. Lamoreaux. *CP Violation Without Strangeness*. Springer, 2004.

[83] I. B. Khriplovich and A. R. Zhitnitsky. *Phys. Lett.*, 109B:490, 1982.

[84] M. Kobayashi and T. Maskawa. *Progress of Theoretical Physics*, 49:652, 1973.

[85] E. Kolb and M. Turner. *The Early Universe*. Westview Press, 1994.

[86] S. Lamoreaux and et al. *Eur. Phys. Lett.*, 58:718, 2002.

[87] L. Landau. *Nucl. Phys.*, 3:127, 1957.

[88] G. Larders. Proof of the tcp theorem. *Annals of Physics*, 2:1, 1957.

[89] T. D. Lee and C. N. Yang. Question of parity conservation in weak interactions. *Phys. Rev.*, 104:254–258, Oct 1956.

[90] J. Leitner and S. Okubo. *Phys. Rev.*, 136:B1542, 1964.

[91] C. Lusher, M. Secca, and M. Richards. *Low Temp. Phys.*, 72:25, 1988.

[92] D. McGregor. *Phys. Rev. A*, 41:2631, 1990.

[93] B. McKellar, S. Choudhury, X. He, and S. Pakvasa. *Phys. Lett. B*, 197:556, 1987.

[94] D. N. McKinsey. *Detecting magnetically trapped neutrons: Liquid helium as a scintillator*. PhD thesis, Harvard University, 2002.

[95] H. Middleton and et al. *Mag. Res. Med.*, 33:271, 1995.

[96] R. N. Mohapatra. *Unification and Supersymmetry*. Springer-Verlag, 1992.

[97] J. Moody and F. Wilczek. *Phys. Rev. D*, 30:130, 1984.

[98] W. Mullin, F. Laloe , and M. Richards. *Low Temp. Phys.*, 80:1, 1990.

[99] D. Murphy and H. Meyer. *Low Temp. Phys.*, 107:175, 1997.

[100] nEDM Colloboration. A new search for the neutron electric dipole moment funding pre-proposal, 2002.

[101] C. Neuman. *J. Chem. Phys.*, 60:4508, 1974.

[102] N. Newbury, A. Barton, G. Cates, W. Happer, and H. Middleton. *Phys. Rev. A*, 48:4411, 1993.

[103] R. Peccei and H. Quinn. *R.D. Peccei and H.R. Quinn*, 38:1440, 1977.

[104] R. D. Peccei and H. R. Quinn. Constraints imposed by cp conservation in the presence of pseudoparticles. *Phys. Rev. D*, 16(6):1791, 1977.

[105] R. D. Peccei and H. R. Quinn. Cp conservation in the presence of pseudoparticles. *Phys. Rev. Lett.*, 38(25):1440, 1977.

[106] J. M. Pendlebury and E. Hinds. *Nuclear Instruments and Methods in Physics Research A*, 440:471, 2000.

[107] D. H. Perkins. *Introduction to high energy physics, 4th edition.* Cambridge University Press, 2000.

[108] A. Petukhov and et al. *Phys. Rev. Lett.*, 105:170401, 2010.

[109] Y. Pokotilovski. *Phys. Lett. B*, 686:114, 2010.

[110] M. Pospelov and A. Ritz. *Phys. Rev. Lett.*, 83(13):2526, 1999.

[111] W. H. Press, B. P. Flannery, S. A. Teukolsky, and W. T. Vetterling. *Numerical Recipes in FORTRAN: The Art of Scientific Computing, 2nd ed.* Cambridge University Press, 1992.

[112] B. Pütz, D. Barsky, and K. Schulten. *Chem. Phys. Lett.*, 183:391, 1991.

[113] E. M. Purcell and N. F. Ramsey. *Phys. Rev.*, 78(6):807, 1950.

[114] N. F. Ramsey. *Phys. Rev.*, 84:506, 1951.

[115] N. F. Ramsey. *Phys. Rev.*, 109:225, 1958.

[116] N. F. Ramsey. *Acta Physica Hungarica*, 55:117, 1984.

[117] D. Rich and et al. A measurement of the absolute neutron beam polarization produced by an optically pumped 3he neutron spin filter. *Nuclear Instruments and Methods in Physics Research Section A: Accelerators, Spectrometers, Detectors and Associated Equipment*, 481(1-3):431 – 453, 2002.

[118] R. Ritter and et al. *Phys. Rev. Lett.*, 70:701, 1993.

[119] B. Robertson. *Phys. Rev.*, 151:273, 1966.

[120] A. Rose-Innes and E. Rhoderick. *Introduction to Superconductivity.* Pergamon Press, 1978.

[121] B. Saam, N. Drukker, and W. Happer. *Chem. Phys. Lett.*, 263:481, 1996.

[122] B. Saam and et al. *Phys. Rev. A, comment (unpublished).*

[123] B. Saam and et al. *Mag. Res. Med.*, 44:174, 2000.

[124] A. D. Sakharov. *JETP Lett.*, 5:24, 1967.

[125] L. I. Schiff. *Phys. Rev.*, 132(5):2194, 1963.

[126] J. Schmiedeskamp and et al. *Eur. Phys. J. D*, 38:445, 2006.

[127] J. Schwinger. *Phys. Rev.*, 82:914, 1951.

[128] J. Schwinger. *Phys. Rev.*, 91:713, 1953.

[129] A. Serebrov. *Phys. Lett. B*, 680:423, 2009.

[130] C. Slichter. *Principles of Magnetic Resonance.* Harper & Row, New York, 1963.

[131] F. Stecker. *Ap. J.*, 185:499, 1973.

[132] S. Stoller, W. Happer, and F. Dyson. *Phys. Rev. A*, 44:7459, 1991.

[133] T. D. Swiet. *J. Magn. Res. B*, 109:12, 1995.

[134] G. 't Hooft. *Phys. Rev. Lett.*, 37(1):8, 1976.

[135] H. Torrey. *Phys. Rev.*, 104:563, 1956.

[136] G. Vasolakis and et al. *Phys. Rev. Lett.*, 103:261801, 2009.

[137] S. Weinberg. *Gravitation and Cosmology.* J Wiley, New York, 1972.

[138] S. Weinberg. *The Quantum Theory of Fields.* Cambridge University Press, 2000.

[139] J. Wilks. *Properties of Liquid and Solid Helium.* Oxford University Press, 1967.

[140] C. S. Wu, E. Ambler, R. W. Hayward, D. D. Hoppes, and R. P. Hudson. Experimental test of parity conservation in beta decay. *Phys. Rev.*, 105:1413–1415, Feb 1957.

[141] W. Xu and et al. *Phys. Rev. Lett.*, 85:2900, 2000.

[142] W.-M. Yao and et al. Review of particle physics. *J. phys. G: Nucl. Part. Phys.*, 33:1, 2006.

[143] Q. Ye and et al. *Phys. Rev. A*, 80:023403, 2009.

[144] Q. Ye and et al. *Eur. Phys. J. A*, 44:55, 2010.

[145] A. Youdin and et al. *Phys. Rev. Lett.*, 77:2170, 1996.

[146] I. B. Zel'dovich. *J. Exp. Theor. Phys.*, 6:1488, 1957.

[147] W. Zheng, H. Gao, B. Lalremruata, Y. Zhang, G. Laskaris, C. Fu, and W. Snow. Search for spin-dependent short-range force using optically polarized ^{3}he gas. *Phys. Rev. D*, 85:061401R, 2012.

[148] W. Zheng, H. Gao, J.-G. Liu, Y. Zhang, Q. Ye, and C. Swank. General solution to gradient induced transverse and longitudinal relaxation of spins undergoing restricted diffusion. *Phys. Rev. A*, 84:053411, 2011.

[149] W. Zheng, H. Gao, Q. Ye, and Y. Zhang. Pressure dependence of wall relaxation in polarized ^{3}he gaseous cells. *Phys. Rev. A*, 83:031505R, 2011.

[150] O. Zimmer, G. Ehlers, B. Farago, H. Humblot, W. Ketter, and R. Scherm. A precise measurement of the spin-dependent neutron scattering length of ^{3}he. *EPJ direct*, 4:1–28, 2002. 10.1007/s1010502a0001.

Biography

Wangzhi Zheng was born in Urumchi, Xinjiang province, China on March 8, 1984. He went to the Urumchi No.1 middle school in 1999. In 2001, he won the first place in the Physics Olympic Games and later he was accepted into Peking University to study physics in 2002 and obtained his B.S. degree there. In 2006, he went to Duke University to pursue his PhD degree under the supervision of Prof. Haiyan Gao. During his PhD study, He was also enrolled in the concurrent M.S. Program in the Biomedical Engineering at Duke University in 2008. He obtained his M.S. degree in Biomedical Engineering in 2011. He has published four papers as the first author and several other papers as a collaborator during his PhD study.